Synthesis of Various Metal Oxides by Different Synthetic Methods

Dissertation

zur Erlangung des akademischen Grades
„Doktor der Naturwissenschaften"

im Promotionsfach Chemie

am Department Chemie

der Johannes Gutenberg-Universität Mainz

in Mainz

vorgelegt von

Massih Ahmad Sarif

geboren in Kabul

Mainz, September 2021

Dekan: ██████████████████

Erster Berichterstatter: ████████████████████

Zweiter Berichterstatter: █████████████

Tag der mündlichen Prüfung: 20 / 12 / 2021

Die vorliegende Arbeit wurde im Zeitraum vom August 2018 bis September 2021 unter der Leitung von Herrn ███████████████ am Department Chemie der Johannes Gutenberg-Universität Mainz durchgeführt.

I hereby declare that I wrote the dissertation submitted without any unauthorized external assistance and used only sources acknowledged in the work. All textual passages which are appropriated verbatim or paraphrased from published and unpublished texts as well as all information obtained from oral sources are duly indicated and listed in accordance with bibliographical rules. In carrying out this research, I complied with the rules of standard scientific practice as formulated in the statutes of Johannes Gutenberg-University Mainz to insure standard scientific practice.

Mainz, September 2021

Massih Ahmad Sarif

Für meine Schwester ████████████████

und in Erinnerung an meine Mama

„Jenseits der Reichweite von Richtig und Falsch liegt ein Feld- ein singendes

Feld. Dort werde ich dich treffen"

Rumi

Danksagung

Meinem besten Freund ████████████████ möchte ich für die lange Freundschaft danken und für seine Unterstützung, die manchmal nötig war, zu jeder Tages- oder Nachtzeit.

Mein Dank gilt ebenfalls allen, die mich in meinen verschiedenen Lebensabschnitten begleitet haben und mir zur Seite standen.

Zuletzt gilt mein besonderer Dank meiner Schwester ████████████████ und meiner Mutter ██████████ für den Rückhalt in allen Momenten meines Lebens.

Abstract

The potential applications of nanoparticles cover an enormous spectrum. The present work addresses the synthesis of nanoparticles using different synthetic methods and their potential fields of application. The first section of the thesis deals with the synthesis of perfectly shaped CoO nanooctahedra in a classical batch synthesis. The preparation of the nanoparticles first required optimization of the synthesis conditions, especially with respect to the ligand concentrations, ligand ratios, and reaction temperature. X-ray and electron diffraction were used to establish the crystal structure of the CoO nanooctahedra. Transmission electron microscopy was used to demonstrate the octahedral morphology of the particles. X-ray spectroscopic and magnetic studies confirmed the formation of phase-pure CoO and its surface chemistry. Molecular dynamics simulations were performed based on the experimental data. This showed that the binding energy of the surface ligands used for synthesis was lowest at a ratio of 1:1 (oleic acid/oleylamine). Based on the experimental and simulated data, a mechanism for the formation of the octahedral nanoparticles was elucidated. The morphology of the particles had a crucial impact on the catalytic activity in anodic oxygenation during electrochemical water splitting.

The second section of the dissertation deals with the synthesis of CeO_2 nanoparticles in segmented flow as well as batch processes. Electron microscopic, thermal, vibrational spectroscopic and sorption studies showed no significant differences in terms of particle surface area or morphology. For segmented flow reactions, the reaction time was significantly reduced, and the yield was significantly increased. Haloperoxidase activity was detected by phenol red assay. The CeO_2 nanoparticles were then used to prepare polycarbonate nanocomposites. The nanocomposites showed up to 85% reduction in biofilm formation. In addition, the formation of the virulence factor pyocyanin, which is directly linked to the quorum sensing system of bacteria, was reduced by 55%.

In the third part of the work, a rapid microfluidic synthesis of $NaCrO_2$ particles on a large scale was elaborated. The structure of $NaCrO_2$ particles and their surface structure were determined by X-ray diffraction and X-ray spectroscopy studies. Investigations by ^{1}H and ^{23}Na nuclear magnetic resonance spectroscopy, Raman spectroscopy, thermal analysis, and transmission electron microscopy provided information about the formation mechanism of the $NaCrO_2$ particles. Submicrometer-sized micelles were formed by water-in-oil emulsions, acting as microreactors in the synthesis and allowing mixing of the reaction components at the molecular level. When the micelle-stabilized mixtures were heated, the product $NaCrO_2$ was formed after

a short annealing time and at moderate temperatures. The microfluidic synthesis of $NaCrO_2$ was used for the synthesis of other layered oxides with the formular $NaMO_2$ such as $NaAlO_2$, $NaFeO_2$ and $NaCoO_2$. It offers the possibility to produce potential or already commercially used battery materials in very short reaction time in large quantities and with constant quality.

Zusammenfassung

Die Anwendungsmöglichkeiten von Nanopartikeln umfassen ein enormes Spektrum. Die vorliegende Arbeit beschäftigt sich mit der Synthese von Nanopartikeln über unterschiedliche Synthesemethoden und deren Anwendungsmöglichkeiten.

Der erste Abschnitt der Arbeit befasst sich mit der Synthese von perfekt geformten CoO-Nanooktaedern in einer klassischen Batch-Synthese. Die Herstellung der Nanopartikel erforderte zunächst eine Optimierung der Synthesebedingungen, insbesondere im Hinblick auf die Ligandenkonzentrationen, -verhältnisse und die Reaktionstemperatur. Durch Röntgen- und Elektronenbeugung wurde die Kristallstruktur der CoO-Nanooktaeder bestimmt. Mit Hilfe der Transmissionselektronenmikroskopie wurde die oktaedrische Morphologie der Partikel nachgewiesen. Röntgenspektroskopische und magnetische Untersuchungen bestätigten die Bildung von phasenreinem CoO und seine Oberflächenchemie. Auf der Grundlage der experimentellen Daten wurden moleküldynamische Simulationen durchgeführt. Dabei zeigte sich, dass die Bindungsenergie der Oberflächenliganden, die zur Synthese verwendet wurden, bei einem Verhältnis von 1:1 (Ölsäure/Oleyamin) am niedrigsten ist. Auf der Grundlage der experimentellen und simulierten Daten wurde ein Mechanismus für die Bildung der oktaedrischen Nanopartikel ausgearbeitet. Die Morphologie der Partikel hatte einen entscheidenden Einfluss auf die katalytische Aktivität in der anodischen Sauerstoffabscheidung bei der elektrochemischen Wasserspaltung.

Der zweite Teil der Dissertation befasst sich mit der Herstellung von CeO_2-Nanopartikeln im segmentierten Fluss sowie im Batchverfahren. Elektronenmikroskopische, thermische, schwingungsspektroskopische und Sorptionsuntersuchungen zeigten keine signifikanten Unterschiede in Bezug auf die Partikeloberfläche oder -morphologie. Bei Reaktionen im segmentierten Fluss wurde die Reaktionszeit erheblich verkürzt und die Ausbeute signifikant erhöht. Die Haloperoxidase-Aktivität wurde mit dem Phenolrot-Assay nachgewiesen. Die CeO_2-Nanopartikel wurden anschließend zur Herstellung von Polycarbonat-Nanokompositen verwendet. Die Nanokomposite zeigten eine Verringerung der Biofilmbildung um bis zu 85 %. Darüber hinaus wurde die Bildung des Virulenzfaktors Pyocyanin, der direkt mit dem Quorum-Sensing-System der Bakterien verknüpft ist, um 55 % reduziert.

Im dritten Teil der Arbeit wurde eine schnelle mikrofluidische Synthese von $NaCrO_2$-Partikeln in großem Maßstab ausgearbeitet. Die Struktur der $NaCrO_2$-Partikel und ihre Oberflächen-struktur wurden mittels Röntgenbeugungs- und röntgenspektroskopischer Untersuchungen ermittelt. Untersuchungen mittels ^{1}H- und ^{23}Na kernmagnetischer Resonanzspektroskopie,

Ramanspektroskopie, thermischer Analyse, und Transmissionselektronenmikroskopie gaben Aufschluss über den Bildungsmechanismus der $NaCrO_2$-Partikel. Über Wasser-in-Öl-Emulsionen werden Mizellen in Submikrometergröße gebildet, die als Mikroreaktoren bei der Synthese fungieren und die Durchmischung der Reaktionskomponenten auf molekularer Ebene ermöglichen. Beim Erhitzen der Mizell-stabilisierten Gemische bildet sich bereits nach kurzer Zeit und bei moderaten Temperaturen $NaCrO_2$. Die mikrofluidische Synthese von $NaCrO_2$ konnte auf die Synthese anderer Schichtoxide $NaMO_2$ (wie $NaAlO_2$, $NaFeO_2$ und $NaCoO_2$) übertragen werden und bietet die Möglichkeit, potenzielle oder bereits kommerziell genutzte Batteriematerialien in sehr kurzer Reaktionszeit in großen Mengen und mit gleichbleibender Qualität herzustellen.

Contents

1. Introduction

Although nanoparticles (NPs) have been used for a long time, research on NPs has only been conducted in recent decades.[1] The term nanotechnology was introduced by Norio Taniguchi in 1974. Since then, the use of NPs has steadily evolved.[2] Today, NPs are used in many fields. Their small size and the resulting large surface-to-volume ratio lead to numerous reactive surface centers. Therefore, NPs are well suited for applications in catalysis, hybrid materials, contrast agents[3], battery materials[4] and biocides[5].

There are two approaches to produce NPs: (i) The top-down and (ii) the bottom-up approach. The top-down method is a physical approach unlike the bottom-up method, which is a chemical approach. It breaks down bulk materials into nanoscale materials, while the bottom-up approach builds up nanomaterials through the assembly of single units like atoms or molecules. Both approaches have their strengths but also weaknesses, the choice of approach depends on several factors such as the later application, costs, and particle properties. The bottom-up approach offers an excellent way to synthesize NPs with narrow size distribution, with well-defined facets and thus morphologies by utilizing surfactants to control the facet growth. The surface structure of NPs is determined by the size and morphology. The ability to adapt these properties is determined by various parameters e.g., surfactants, reaction temperature or solvents. Synthetic control is therefore crucial to obtain NPs with the desired properties.[6]

The most common way to synthesize NPs through the bottom-up approach is the batch process, which has, however, some disadvantages. The physical and chemical properties of NPs are significantly determined by their size. It is well known that an upscaling of batch syntheses often leads to a broad size distribution or even changes concerning particle morphology, due to the changes of mass and heat transfer. Consequently, it is mandatory to find alternatives, due to the lack of control in batch processes. Flow syntheses offer an alternative to the conventional batch processes. Several factors indicate that flow synthesis can eliminate many of the problems of batch synthesis that can arise from upscaling. The use of micrometer-sized flow tubes leaves the surface-to-volume ratio unchanged during upscaling, furthermore, it allows a higher heat and mass transfer and therefore also a higher conversion rate.[7-8] Important parameters for the flow synthesis are temperature, pressure, reactants concentration and stream flow, and for the setup, the tube material, length of the tube and the pump type. Due to the formation of particles,

clogging issues can occur within the tubes, therefore optimizing the mentioned parameters and the setup are mandatory to avoid those issues.

Recent publications clearly show that upscaling of syntheses in flow setups are easily possible, within short reaction times and therefore high yields per hour. Brutchey et al. synthesized nickel NPs with a 60% yield and therefore 15% more than the usual batch synthesis, also they were able to synthesize the Ni NPs with a conversion rate of 1,1 g/h.[9] The possibility to use different flow modes offers additional possibilities to adjust and therefore optimize the synthesis. Santamaria et al. were able to synthesize iron oxide NPs in a short reaction time, with different morphologies and crystalline structures by using a segmented flow and different gases as carrier medium e.g. N_2, O_2 or CO.[10]

The present work deals with the synthesis of various NPs using different synthesis methods, in particular (i) batch- and (ii) microfluidic synthesis, as well as the characterization and application of the NPs. Major disadvantages associated with classical flask synthesis are theoretically avoidable by microfluidics. In the context of this work, among other things, this was investigated. Furthermore, the synthesis of NPs is in general influenced by various factors e.g., reaction time, ligand concentration and ligand ratios. The influence of the mentioned factors on the morphology, dispersity, size, and catalytic activity were investigated.

1.1 References

(1)   D. Schaming, H. Remita and H. C. Flemming, *Found. Chem.*, 2015, **17**, 187-205.

(2)   N. Taniguchi, Proc. Intl. Conf. Prod. Eng. Tokyo, Part II, Japan Society of Precision Engineering, 1974.

(3)   T. H. Shin, Y. Choi, S. Kim and J. Cheon, *Chem. Soc. Rev.*, 2015, **44**, 4501-4516.

(4)   M. N. Tahir, B. Oschmann, D. Buchholz, X. Dou, I. Lieberwirth, W. Tremel, R. Zentel and S. Passerini, *Adv. Energy. Mater.*, 2016, **6**, 1501489.

(5)   K. S. Siddiqi, A. Husen and R. A. K. Rao, *J. Nanobiotechnol.*, 2018, **16**, 14.

(6)   M. Sarif, J. Hilgert, I. Khan, R. A. Harris, S. Plana-Ruiz, M. Ashraf, E. Pütz, J. Schemberg, M. Panthöfer, U. Kolb, M. N. Tahir and W. Tremel, *Langmuir*, 2020, **36**, 13804-13816.

(7)   J. Ma, S. M. Y. Lee, C. Yi and C. W. Li, *Lab Chip*, 2017, **17**, 209-226.

(8)   Y. Song, J. Hormes and C. S. S. R. Kumar, *Small*, 2008, **4**, 698-711.

(9)   E. J. Roberts, S. E. Habas, L. Wang, D. A. Ruddy, E. A. White, F. G. Baddour, M. B. Griffin, J. A. Schaidle, N. Malmstadt and R. L. Brutchey, *ACS Sustain. Chem. Eng.*, 2017, **5**, 632-639.

(10)   A. Larrea, V. Sebastian, A. Ibarra, M. Arruebo and J. Santamaria, *Chem. Mater.*, 2015, **27**, 4254-4260.

2. Theoretical Background

2.1 Formation of Nanoparticles

Wet chemical synthesis, a variation of the bottom-up approach, has several advantages over the top-down approach. First, implementation is simple. Furthermore, NPs with a low dispersity and with specific morphologies can be obtained with surfactants, which control NP facet growth. The properties of NPs are significantly influenced by their size and morphology as they determine the surface structure. Therefore, it is essential to control particle nucleation and growth. The LaMer model[1] is fundamental for understanding the formation of NPs in wet-chemical synthesis. Originally, LaMer and Dinegar used the classical nucleation theory in order to describe the formation of sulfur sols. Nevertheless, it is used as a standard model to describe the homogenous nucleation and growth of NPs. The LaMer model is a kinetic model describing the solute concentration change as a function of time (Figure 2.1). Figure 2.1 is divided into three phases. The first phase comprises the formation of monomers, the second the nucleation process and the third the growth of the evolving NPs. C_s is the saturation concentration, which describes the solubility of the monomer. C_{min} is the minimum and C_{max} the maximum supersaturation. In the first phase, the monomer concentration increases rapidly until it reaches the minimum saturation concentration C_{min}. At this point the nucleation process and therefore the transition to the second phase starts. The monomer concentration in phase 2 still increases, due to the formation of monomers in phase 1. Provided that no further monomers are formed, the concentration decreases. As soon as the monomer concentration reaches again the minimum saturation concentration, the transition into the third phase starts.[1-2]
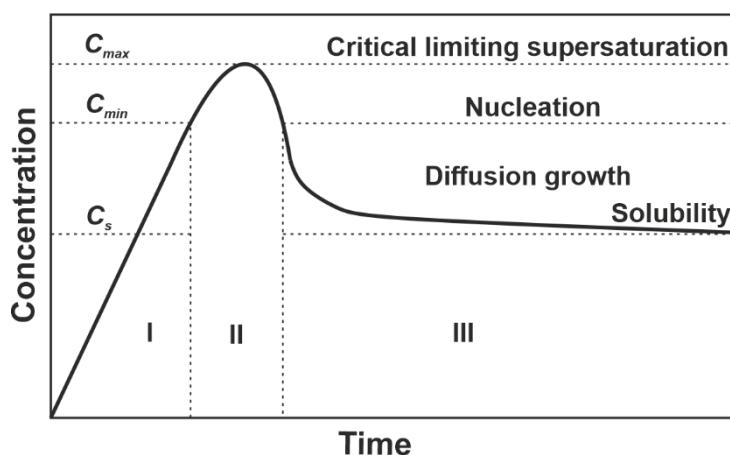
Figure 2.1. LaMer model of nucleation and growth. Adapted with permission from ref [1].

The growth by diffusion starts in the third phase. If the monomer concentration is lower than the minimum saturation concentration C_{min} but higher than the saturation concentration C_s, the particles keep growing. The synthesis of monodisperse NPs requires the temporal separation of nucleation and growth processes. During the diffusion-controlled growth of the NPs (phase III), no further nuclei may be generated. Therefore, the nucleation rate should be as high as possible (burst nucleation) ensuring a step change into the growth phase. The temporal separation can be done by setting various parameters, e.g., temperature or pH-value, but also through the procedure, e.g., hot injection of the precursor.[3] A careful control of the parameters is therefore necessary to obtain monodisperse NPs. Due to the sensitivity of NPs synthesis concerning their parameters, smallest changes during the synthesis can change the particle size, quality and even the phase. Optimization is therefore crucial for the wet-chemical approach. However, it is well known that a simple scale-up of an optimized synthesis does not always work and often heavily influence the morphology, phase, or dispersity. Changes in heat- and mass transfer are responsible for this. Upscaling is always accompanied by a change in volume, leading also to a change of the surface-to-volume ratio. The change of the ratio impacts the heat transfer significantly.[4-7] In a typical batch synthesis, the heating process will be carried out externally. Through the external heating the energy is transferred through the walls of the flask and dissipated into the reaction solution. Three main reasons are responsible for the heating up of the reaction solution (i) radiation, (ii) conduction and (iii) convection.[8] Thermal radiation is the transfer of energy through electromagnetic waves and conduction through the contact between the heating source and the flask wall. Convection describes the heat transfer within the reaction solution. Convection processes are directly related to mass transfer, which describes the movement of mass within the batch.[9] A change in surface-to-volume ratio changes the thermal energy and the mass transfer. To enable upscaling, it is therefore essential to keep the change in the surface-to-volume ratio as low as possible or even unchanged. In a flow system

4

the ratio does not change, it remains constant. It is therefore important to give an insight into the dynamics of flow systems in order to understand and apply the system as an alternative to batch synthesis.

2.2 Microfluidics

2.2.1 Fluids

The term microfluidics consists of the two terms micro and fluid. While the former describes the size of the container that transports the medium, the latter refers to the nature of the medium in the container. In general, a fluid is a substance which deforms, i.e., flows by applying shear forces.[10] Therefore, liquids, gases and plasmas can be assigned to fluids. Fluids can be divided into ideal and real fluids. Ideal fluids are incompressible, they show no internal resistance to flow and therefore no viscosity, while real fluids show to some extent dependent on the material the mentioned behavior. For real fluids, a further subdivision can be made into Newtonian and non-Newtonian fluids. Newtonian fluids obey the Newtonian law of viscosity (Eq 2.1).[10-12]

$$\tau = \eta \frac{du}{dy} \qquad (2.1)^{[11]}$$

Here, τ stands for the shear stress, η for the dynamic viscosity, which is the product of the kinematic viscosity v and the density ρ, furthermore $\frac{du}{dy}$ describes the shear rate. Eq. 2.1 shows that the shear stress is proportional to the shear rate. Therefore, no change of the viscosity occurs in dependency of the shear rate (Figure 2.2A-B). A prototypical Newtonian fluid is water, which obeys Eq. 2.1. Different from Newtonian fluids non-Newtonian fluids behave differently when shear forces are applied.[10-12]
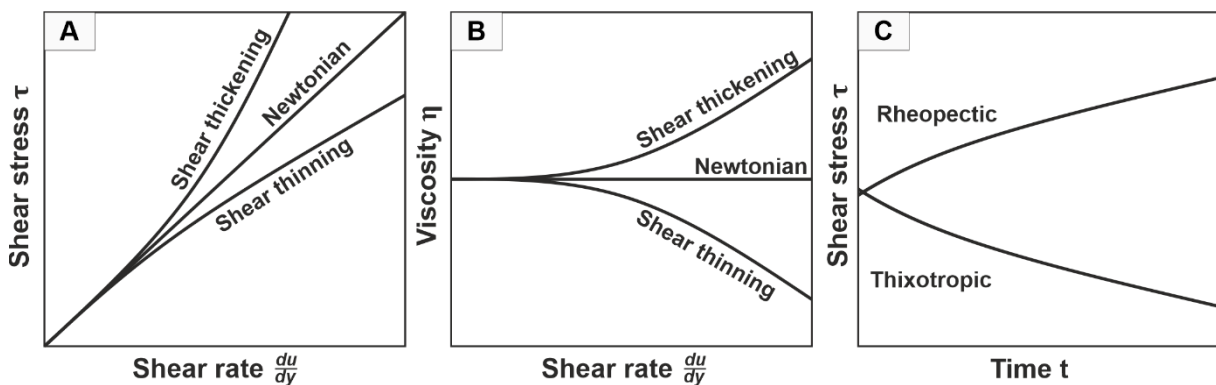
Figure 2.2. Rheogram of Newtonian and non-Newtonian fluids. (A) Shear stress as a function of shear rate, (B) viscosity as a function of shear rate and (C) time. (A-C) Adapted with permission of ref [13-15].

Non-Newtonian fluids are divided into two regimes. The nonlinear behavior of the fluids is divided by focusing on the (i) change of viscosity with increasing shear rate and (ii) with

constant shear rate during a time interval. Fluids whose viscosity increases with increasing shear rate exhibited shear thickening behavior and *vice versa* shear thinning behavior (Figure 2.2A-B). Fluids that change their viscosity at a constant shear rate as a function of time are divided into thixotropic and rheopectic materials (Figure 2.2C). Thixotropic fluids show a time-dependent decrease in their viscosity, while the viscosity for rheopectic materials increases, when the fluids undergo shear stress.[10] Internal friction and the associated viscosity are important factors influencing the flow behavior of fluids. Figure 2.3 shows a flow diagram of the different rheological behavior of fluids.
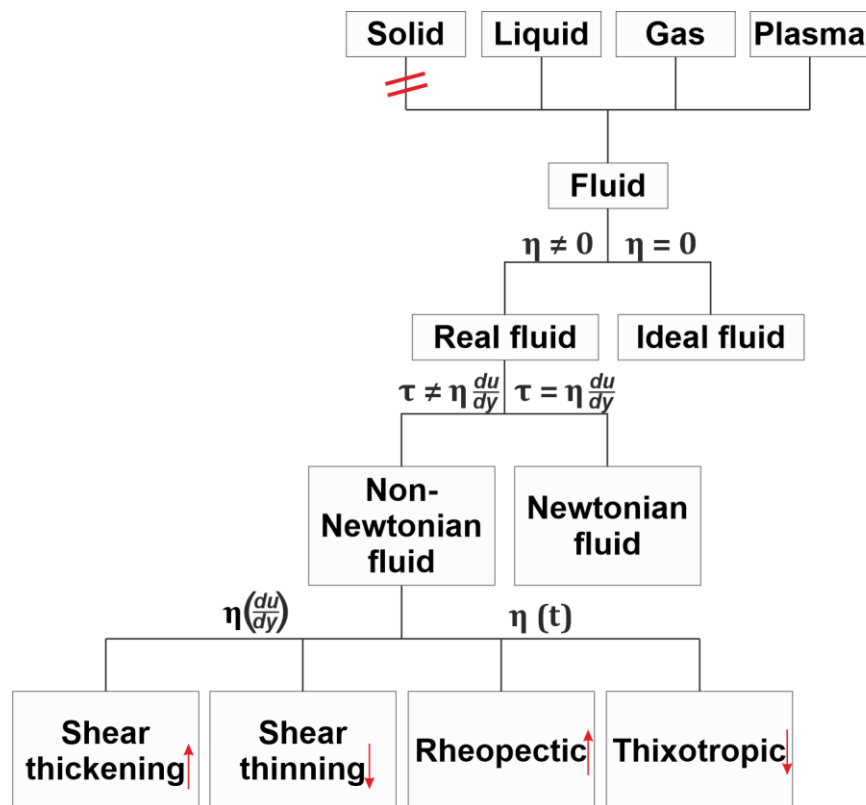
Figure 2.3. Flow diagram of the rheological behavior of fluids.

2.2.2 Laminar and Turbulent Flow

The flow profile of Newtonian fluids can vary, depending on various factors. The flow profile is divided into laminar and turbulent flow.[10] In laminar flow, the fluid flows in layers that do not mix with each other. Mass transfer therefore takes place only through the momentum of the reactants, but not through the mixing of the layers. The layers move parallel to the tube wall in the flow direction. Due to the properties of a real fluid, friction occurs between the fluid layers, and with the tube wall. The internal friction between the layers and the interaction with the tube walls leads to different velocities of the single layers, which finally leads to a parabolic flow profile (Figure 2.4). The flow velocity reaches its maximum in the center of the tube, while it

6

decreases towards the pipe walls. The velocity profile can be described with the Hagen-Poiseulle equation (Eq. 2.2).[16]

$$Q = \frac{\pi \Delta p R^4}{8 \eta L} \qquad (2.2)^{[17]}$$

Q stands for the volumetric flow rate, Δp is the pressure drop between the ends of the tube, R is the tube radius, η is the dynamic viscosity and L the tube length. The law represents the dependence of the volumetric flow rate on the tube radius. Furthermore, the law assumes that the viscosity does not change as a function of shear rate or time, i.e.it applies to Newtonian fluids.[18] Equation (Eq. 2.2) shows that doubling the tube radius leads to a 16-fold volumetric flow rate. It also shows that the flow rate is directly dependent on the viscosity. Taking that into account, the volumetric flow rate is determined by the tube radius and viscosity.

In a turbulent flow, fluid layers are no longer present, instead, the streamlines are chaotic, leading to fluctuations concerning the pressure and flow velocity, but also to an efficient mixing of the layers. Therefore, the Hagen-Poiseulle equation cannot be used in turbulent flow. The transition from laminar to turbulent flow depends significantly on the flow velocity. The Reynolds number R_e can be used to determine whether a flow is laminar or turbulent. It describes the ratio of inertial forces to viscous forces within a fluid (Eq. 2.3).[11,16]

$$R_e = \frac{\rho u L}{\eta} \qquad 2.3^{[11]}$$

ρ describes the density of the fluid, u the flow velocity, L is the characteristic length, for the flow in a tube, L is usually equal to the inner diameter of the tube and. η describes the dynamic viscosity. Eq. 2.3 states that the Reynolds number increases with increasing flow velocity. Laminar flow occurs at $R_e < 2300$ and turbulent flow at $R_e > 4000$. In the range $2300 < R_e < 4000$ an intermittent flow can be observed consisting of irregular intervals of laminar and turbulent flows.[16]

Synthesizing NPs requires mixing of the precursors. In laminar flow mixing occurs through the momentum of the reactants rather than through the mixing of layers. The lack of mixing can lead to the formation of NPs with a broad dispersity, as well as to the formation of other phases as by-products. Furthermore, the parabolic flow profile leads to different residence times of the reactants, which also influences particle growth. In flow setup microfluidic mixers can be used which induce turbulence in a spatially limited area and thus enable the layers to be mixed. The turbulent flow allows excellent mixing, but due to the fluctuations in pressure and flow velocity, the reproducibility of a synthesis is not always given. During the synthesis of NPs, gas formation often occurs due to thermal decomposition of the precursors or reflux of the solvents.

The formation of gases induces turbulence between layers, therefore mixers can be dispensed for synthesis, where thermal decomposition occurs.

Long residence times and therefore low flow velocities can lead to clogging, due to the accumulation of NPs within the tubes. Short residence times can result in no conversion. The setting of flow velocity is therefore crucial in order to optimize a synthesis in a flow setup. In addition to the flow velocity, other parameters are essential as well. A closer look to those parameters is therefore necessary.
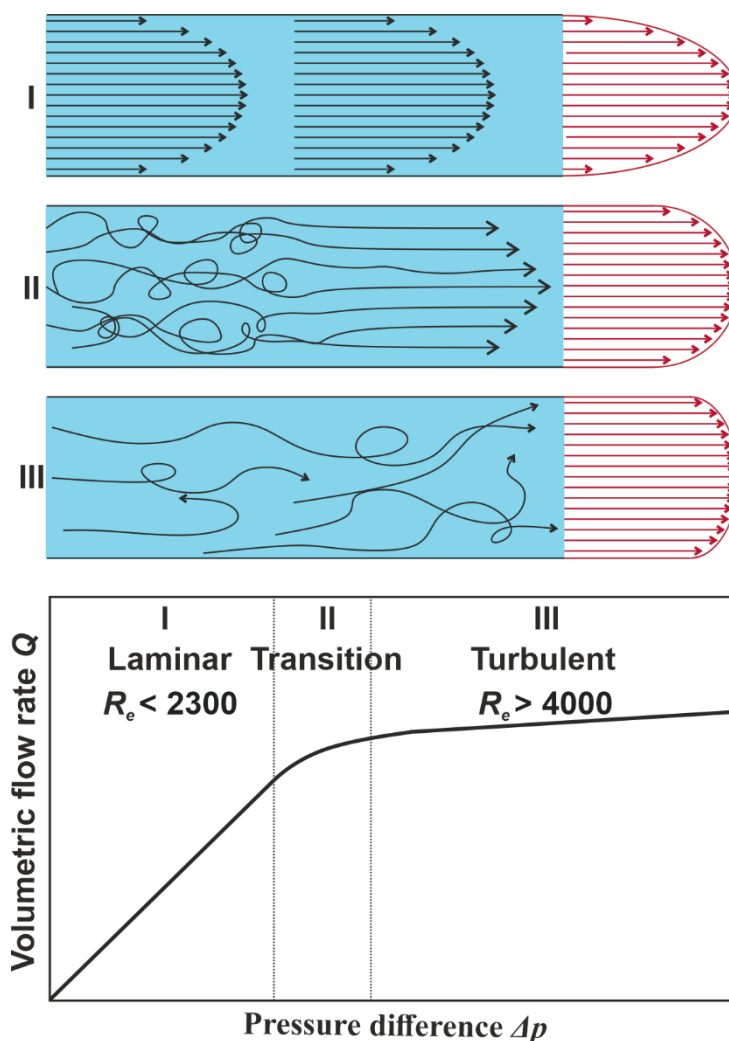
Figure 2.4. Laminar, transient and turbulent flow with the corresponding Reynolds number R_e. Adapted with permission of ref [19].

2.2.3 Setup and Parameters

2.2.3.1 Microfluidic Pumps

In microfluidics, two different types of pumps are generally used: (i) Syringe or (ii) peristaltic pumps. In a (i) syringe pump, the syringes serve as fluid reservoir and for dispensing the fluid into the flow system. The pump motor exerts pressure *via* an actuator which results into the

8

dispensing of the fluid into the tubes (Figure 2.5A). (ii) Peristaltic pumps belong to the group of mechanical displacement pumps. From an external fluid reservoir, the fluid is delivered into the tube by the principle of peristalsis, using a rotating head mechanism. The head mechanism consists of a certain number of actuators. The tube is placed along the actuators, contraction and relaxation (peristalsis) cause the fluid to spread in the tube (Figure 2.5B).[20]
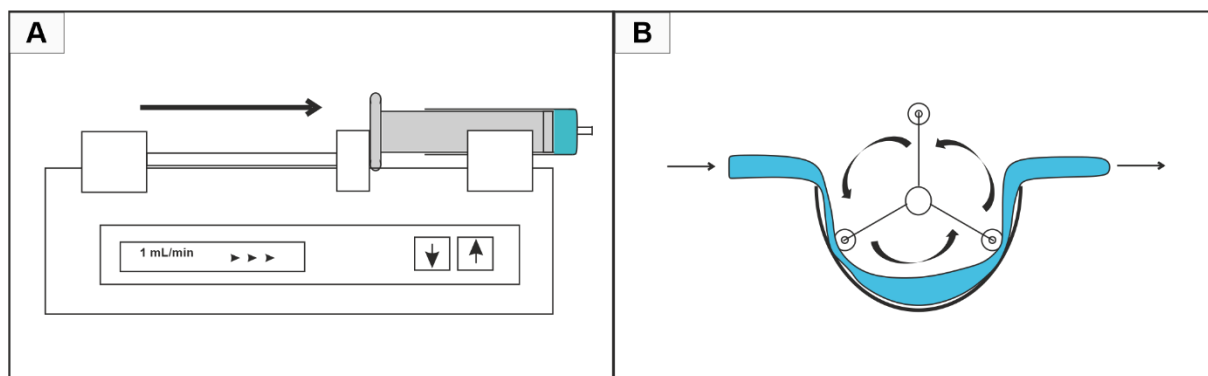
Figure 2.5. Pump types. (A) Syringe pump and (B) peristaltic pump.

Syringe pumps can be adjusted very precisely in their injection speed, making them particularly suitable for reactions in which the slightest deviations can manipulate the synthesis. Syringe pumps can also be used at very high pressures, allowing a range of parameter variations concerning the synthesis. A major disadvantage is that the fluid volume is limited by the syringe volume, therefore upscaling is limited. Furthermore, some reactants do not dissolve in the solvent at room temperature, as the syringe cannot be heated. The range of possible applications is further limited. Peristaltic pumps are slightly less precise than syringe pumps. Furthermore, they cannot be used at very high pressures, limiting therefore the range of parameter variations. However, by using an external fluid reservoir, the volume and therefore upscaling is not limited. More importantly, the external fluid reservoir can be heated which allows further synthetic options. Therefore, peristaltic pumps are particularly suitable for the synthesis of NPs, since upscaling is possible, and no solubility issues occur. Due to the advantages of the peristaltic pump, the work described in this dissertation was carried out exclusively with peristaltic pumps.

2.2.3.2 Tubes, Flow Velocity and Heating Elements

Concerning the tubes two factors should be considered, the overall length of the tube and the tube material. The overall tube length depends on the setup such as the number of different heating regimes and the flow mode. More importantly, the tube length in correlation with the flow velocity determines the reaction time. The formation of NPs within the tubes can lead to clogging, the correct length is therefore essential to optimize a synthesis. Although the reaction time can be determined by the flow velocity, issues occur due to the formation of gases during

the decomposition of the reactants, which statistically influence the flow rate caused by the additional pressure. Therefore, a careful choice of the tube length and flow velocity is essential to optimize a synthesis.

Mainly tubes made of glass, stainless steel or polymer-based materials are used in microfluidics. Glass is difficult to handle due to its fragility. Therefore, stainless steel or polymer-based tubes are usually used. The heating temperature is a major factor in the choice of the tube materials. Polymer-based tubes like fluorinated ethylene propylene (FEP), poly-tetrafluorethylene (PTFE) or polyether ether ketone (PEEK) have a maximum usage range temperature between 200 – 350 °C, under the condition that no tube-damaging substances are used. For temperatures up to 200 °C, these tubes can be used. At higher temperatures, stainless steel tubes are preferable. Unsaturated fatty acids are often used in the synthesis of NPs. Transition metals can accelerate the autooxidation of unsaturated fatty acids due to their catalytic effect. Stainless steel tubing can thus act as a catalyst for autooxidation, and high temperatures favor the process.[21-22] Depending on the synthesized NPs, autooxidation can affect the synthesis. Glass tubes should be considered if this issue occurs. Nevertheless, autooxidation is not a common issue in microfluidics, therefore stainless steel is the material of choice for high temperature syntheses. For temperatures lower than 180 °C oil baths are sufficient as heating elements. Possible alternatives at higher temperatures are sand baths, molten salt baths or continuous flow heaters. In this work, cartridge heaters were used, placed in the center of a cylindrical steel inlet. The inlet had a spiral-shaped notch, in which the stainless-steel tube was attached. The inlet was in a ceramic sleeve for insulation and better temperature control. (Figure 2.6).
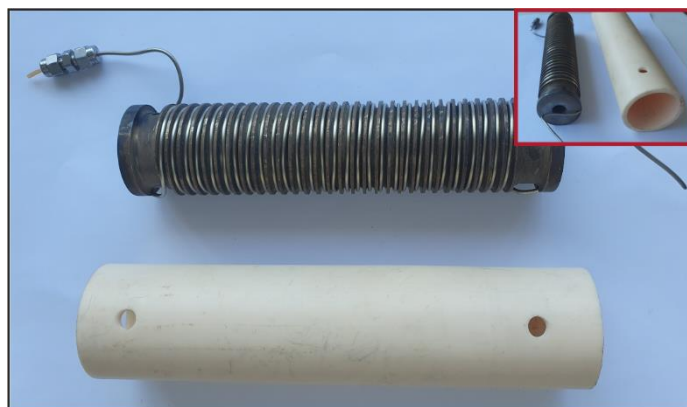

Figure 2.6. Heating element, with the cylindrical steel inlet and ceramic sleeve.

2.2.3.3 Flow Modes

Different flow systems can be run in microfluidics. The choice of the particular flow system depends crucially on the synthesis conditions. The flow systems are subdivided into continuous and segmented flow systems. Continuous flow setups are the most established system in microfluidics, due to their simplicity. While the single-phase mixture flows through the main channel, further reactants can enter the reaction phase *via* side channels. This allows the realization of multistep syntheses, e.g., the synthesis of heterodimers. Due to the high throughput of fluid volumina and the direct contact of the fluid with the tube walls a high risk of channel clogging exists, due to the deposition of NPs on the tube walls (Figure 2.7A).[4] In segmented flow, two immiscible fluids are used. The reaction solution and the carrier medium alternate in the tube. Segmented flow systems are divided into liquid-liquid flows, e.g., water in oil, and gas-liquid flows.[4] The generation of droplets can be done by microfluidic chips or T-junctions. While the former is used for small fluid volumes and the throughput of NPs is low, T-junctions are suitable for the synthesis of NPs on a large scale.[23] The droplet size depends mainly on the flow rate, while the morphology depends on the composition of the reaction solution, the carrier medium, and the resulting interaction with the tube walls.[23] The different droplet morphologies are shown in Figure 2.7B. Figure 2.7B.1 shows the classical droplet morphology. The droplets are completely enclosed by the carrier medium and thus have no contact with the tube walls. Highly hydrophobic solutions, such as polytetrafluorethylene (PTFE), are suitable as the carrier medium, with water as reaction solution. Due to the polarity of water, interactions with the tube wall are low, ensuring therefore the formation of droplets.
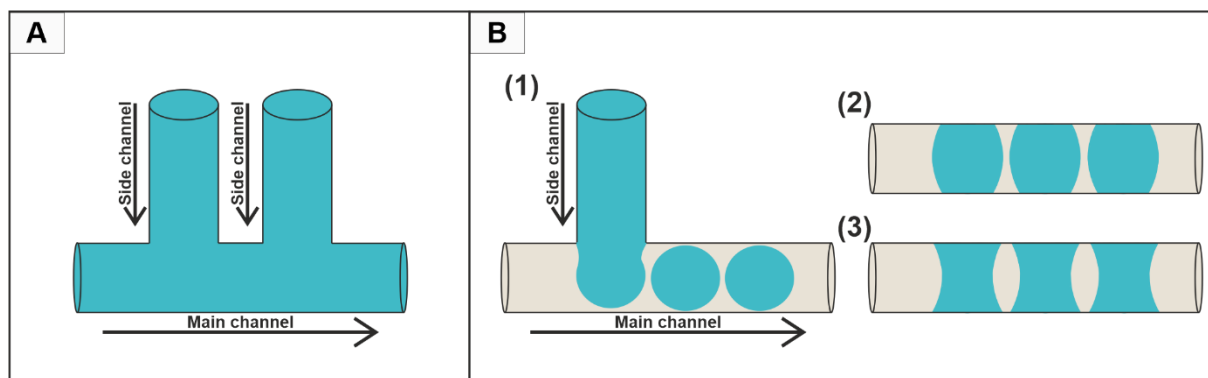
Figure 2.7. Illustration of the (A) continuous- and (B) segmented flow. The segmented flow is shown as (B.1) the droplet mode, (B.2) plug mode and (B.3) slug mode. Adapted with permission of ref [4,24].

By changing the polarities of the carrier medium and reaction solution, the formation of convex droplets (plug mode) occurs (Figure 2.7B.2). In the plug mode, carrier medium and reaction solution are in contact with the tube walls. The carrier medium should not wet the tube walls to avoid the formation of droplets rather than plugs. Therefore, gases or non-polar compounds are

suitable as carrier media. Polar solvents are suitable for the reaction solution due to the low affinity to the tube walls. If the reaction solution shows a strong affinity to the tube walls, concave shaped droplets are formed (slug mode, Figure 2.7B.3). Nonpolar solvents as a reaction solution (e.g., hexane) tend to form slugs rather than droplets. The classical droplet flow is the most suitable choice for the synthesis of NPs.[23] Due to the lack of contact with the tube walls, the material of the tubes does not affect synthesis, e.g., through autooxidation processes. Furthermore, the probability of clogging is lowest, as the resulting NPs cannot interact with the walls and therefore do not adhere.[4,23] Nevertheless, droplet flow cannot always be driven. High reaction temperatures limit the choice of the carrier medium. Therefore, high polarity differences between reaction solution and carrier medium cannot always be achieved. Furthermore, the composition of the reaction solution determines the interaction with the tube walls. Therefore, it is not always possible to prevent the reaction solution from interacting with the tube walls. Segmented flow is particularly suitable when the risk of clogging in the continuous flow is too high. In addition, the use of gases in segmented flow can promote the oxidation of NPs unstable in air. Furthermore, different morphologies and phases can be produced in the gas-liquid flow, by varying the gas with unchanged composition of the reaction solution.[24]

2.3 Nanoparticles and Their Applications

2.3.1 Selective Synthesis of Nanoparticles

The selective synthesis and thus the formation of certain facets can be essential, depending on the latter application. Therefore, the synthesis of NPs with certain facets is usually accompanied by the optimization of synthetic variables, as even small deviations in the synthesis can lead to a change in dispersity or even phase. It is therefore essential for a reproducible optimized synthesis to consider at least the most important variables. Important variables in a synthesis are the (i) metal precursor, (ii) surfactants, (iii) solvent (iv) heating temperature and heating rate, and (v) reaction time. The variables cannot be considered as independent factors affecting the system, but they merge into each other and therefore influence each other. For example, the selection of a different metal precursor can influence not only the phase of the product, but also the decomposition temperature. However, there are characteristic changes when changing a single parameter, so individual consideration of these is essential to understand the system.

It is generally known that the (i) variation of the metal precursor has an influence on the resulting phase, faceting, dispersity, and reaction temperature.[25-27] Banerjee et al.[25] investigated the influence of different iron precursors on the properties of magnetite NPs while maintaining the same synthesis conditions. Their results showed changes concerning the morphology of the NPs by changing the metal precursor ($Fe(NO_3)_3 \cdot 9\,H_2O$; $FeCl_3 \cdot 6\,H_2O$). Furthermore, the use of an Fe^{2+} precursor (e.g. $FeSO_4 \cdot 7\,H_2O$) led to the formation of additional side phases (α-FeO(OH), γ-FeO(OH)). The preparation of pure cobalt NPs in the presence of oleylamine (OAM), which acts as a reduction agent, showed that changing the cobalt precursor from cobalt acetate ($Co(ac)_2$) to cobalt acetylacetonate ($Co(acac)_2$), led to a higher decomposition temperature and smaller NPs.[28] These two examples illustrate the influence of the metal precursor on the final product. Numerous causes can be the reason for this interference, but in general a change in the stability of the precursor or even in the reaction mechanism is usually associated with it. During the thermal decomposition of the metal precursor, intermediates are often formed by ligand exchange, which in turn decompose to form the actual precursor. Ligand exchange in turn depends on the stability of the metal precursor. A more stable precursor can cause the decomposition temperature to change, but also the nucleation and growth phases, which in turn can change the size and dispersity of the particles, but also the facet growth. The cobalt synthesis can be taken as an example. $Co(acac)_2$ is thermodynamically more stable than $Co(ac)_2$ due to the multidentate nature of acetylacetonate and the associated chelate effect. The ligand exchange of acetylacetonate with OAM therefore requires a higher temperature, which in turn increases burst nucleation and thus the number of nuclei, which finally leads to smaller NPs. As a result, particles of approx. 3 nm in size are obtained instead of 6-10 nm particles when using cobalt acetate.[28] The same applies to magnetite particles mentioned above. A change in the oxidation state can affect the formation of the phase, since the reaction mechanism changes.[25] Therefore, the variation of the metal reactants is essential to gain insight into the mechanism of NP formation.

Beside the metal precursor, (ii) surfactants play an essential role in the wet chemical synthesis of NPs. Surfactants are characterized by long non-polar chains (tails), as well as a polar part (head). Due to the large surface/volume ratio, NPs tend to have relatively high surface energies, The task of a surfactant is to minimize the surface energy in order to stabilize them and thus protect them from agglomeration.[29] However, surfactants can also contribute to the formation of the particles during the nucleation stage e.g. by ligand exchange[25] or act as a reducing agent[30]. Furthermore, in addition to their stabilizing effect on the particles, surfactants can also be used as a substitute for solvents. For example, ferrite NPs (MFe_2O_4) can be produced in the

presence of OAM, which acts as stabilizing agent but also as solvent.[31] Due to their functional groups, surfactants can also act as an acid or base. A well-known combination of two surfactants used within a single synthesis is oleic acid (OAC) and OAM.[32-34] Due to the functional groups of OAC and OAM, an acid-base equilibrium is established between the two surfactants. OAM acts as a base and deprotonates OAC (OAC + OAM = OAC$^-$ + OAMH$^+$) and therefore improves the adsorption of oleate on certain facets.

Asadi et al.[32] investigated the influence of the ratios of the two surfactants with respect to the morphology, size and size distribution of the resulting iron oxide particles. Various ratios of the two surfactants were tested, and an optimum ratio of 3:1 OAC to OAM was determined to obtain NPs with a defined morphology and narrow size distribution. Changing the ratio significantly affected facet growth and thus morphology as well as dispersity. Through molecular dynamic simulations, it was shown that at a ratio of 3:1 OAC:OAM, the binding energy of the deprotonated OAC to the surface of the NPs showed the highest negative binding energy and thus the ratio is most suitable for stabilizing the particles. When optimizing a synthesis, the concentrations of the ligands are therefore essential, and optimization in terms of concentration is indispensable.

The influence of (iii) solvents on the synthesis of NPs is also an important factor to consider when optimizing a synthesis. During synthesis, the polarity of the solvents decisively influences the solvent-particle, solvent-ligand, particle-ligand, and particle-particle interactions. Therefore, solvents have a crucial influence on particle growth, as well as the stability of the particles with respect to agglomeration.[35-37] In general, colloidal NPs can be stabilized in solution by electrostatic or steric interactions. While in steric stabilization, surfactants on the surface of the particles prevent agglomeration, electrostatic stabilization relies on the formation of an electrochemical double layer. NPs have a charge on their surface, so in solution an electrochemical double layer forms on the particle surface. The strength of the electrochemical double layer depends, among other things, on the polarity of the solvent. When the polarity is changed, this also influences the electrochemical double layer, which ultimately leads to changed conditions in the growth of the particles.[35,38] Besides the influence of the polarity of the solvent on the electrochemical double layer and thus the electrostatic stabilization, the solvent also influences the steric stabilization. Taking oleate capped NPs as an example, the polarity of the solvent is crucial for the swelling of the oleate layer onto the surface of the NPs.[37] Wong et al.[37] demonstrated this influence with coarse-grained model structures and compared theoretical and experimental results of oleate capped CdSe quantum dots. Through their investigations they showed that the extension of the swelling layer and therefore the

thickness of the layer increases with decreasing polarity. Various solvents were used, ranging from water to chloroform and hexane. The results showed the agglomeration behavior due to the polarity change of the solvent and therefore the change of the thickness of the oleate layer.[37] Solvents can also be used as surfactants[31] or even as reagents[39]. The range of influencing factors is enormous. When optimizing a synthesis, the fine-tuning of the solvent is therefore crucial for the particle properties.

The main influence of (iv) the heating temperature and heating rate is in the nucleation process, due to the thermal decomposition of the precursor. To understand this process, kinetic and thermodynamic factors must be considered. Two essential terms play a role in the homogeneous nucleation of a spherical particle. Eq. 2.4 shows the total free energy ΔG.[40]

$$\Delta G = 4\pi r^2 \gamma + \frac{4}{3}\pi r^3 \Delta G_v \tag{2.4}^{[40]}$$

$$\Delta G_v = \frac{-k_B T ln(S)}{v} \tag{2.5}^{[40]}$$

The first term represents the surface free energy. Here r is the radius of the particle and γ the surface energy. The second term is the bulk free energy, where ΔG_v represents the crystal free energy. ΔG_v depends (Eq. 2.5) upon the Boltzmann constant k_B, the temperature T, the supersaturation S and the molar volume v. While the first term in Eq 2.4 is positive, due to the formation of a particle and thus the formation of a surface, the second term is negative. The second term has a stronger effect on the total free energy with increasing particle radius. Above a certain radius, the so-called critical radius, the second term predominates, and the formation of nuclei is thermodynamically preferred. It is therefore the minimum radius at which nuclei do not return to solution (Eq. 2.6). The critical radius corresponds with the critical free energy ΔG_{crit} (Eq. 2.7). The critical free energy is obtained by differentiating ΔG with respect to r.[40]

$$r_{crit} = \frac{-2\gamma}{\Delta G_v} = \frac{2\gamma v}{k_B T ln(S)} \tag{2.6}^{[40]}$$

$$\Delta G_{crit} = \frac{4}{3}\pi \gamma r_{crit}^2 \tag{2.7}^{[40]}$$

Eq. 2.6 states that with increasing temperature the critical radius decreases and thus the critical free energy. The nucleation rate, i.e. the formation of N nuclei after a certain time unit t can be obtained by an Arrhenius type equation (Eq. 2.8).[40]

$$\frac{dN}{dt} = A exp\left(-\frac{\Delta G_{crit}}{k_B T}\right) = A exp\left(\frac{16\pi \gamma^3 v^2}{3k_B^3 T^3 (ln(S))^2}\right) \tag{2.8}^{[40]}$$

The nucleation rate depends mainly on temperature, supersaturation and surface free energy. When the temperature increases, the nucleation rate increases as well. A higher number of nuclei also influences the growth process of the particles. Since the higher number of nuclei

means that fewer monomers are available for each nucleus, the size of the particles decreases for higher temperatures. Beside the heating temperature, the heating rate influences the nucleation process. At slow heating rates, burst nucleation is suppressed. Thus, less nuclei are produced, and the particles generally become larger. Furthermore, the nucleation period is extended, whereby growth and nucleation phases can overlap and the size distribution becomes broader.[41] The heating temperature and rate are therefore important parameters to vary particle size.

In particular the (v) reaction time influences the particle size. The duration of the growth phase and thus the size of the particles can be influenced by the reaction time. Short reaction times therefore often lead to smaller particles than long reaction times. However, the dispersity of the particles can also be influenced by changing the reaction time. Therefore, it is essential to adjust reaction time to the remaining conditions to optimize a synthesis.[42-45]

In summary, some important synthetic variables that significantly influence particle properties have been discussed. However, it should be note that there are even more factors which have not been explained in detail, but which affect the outcome of a synthesis, e.g., the concentration of the metal oxide/chalcogenide product and thus the supersaturation of the solution. Still, the optimization of a synthesis should focus on the most essential parameters, otherwise there is a risk of complicating the system, making it impossible to understand the reaction and the mechanisms behind it.

2.3.2 Haloperoxidase Mimicry of Nanoparticles

Biofilms are communities of microorganisms embedded within a self-generated matrix of extracellular polymeric substances, attached to each other and to a surface.[46-47] The formation of biofilms is a dynamic process and divided into different stages which are shown in Figure 2.8. In the first stage, the reversible attachment of microorganism to a surface start. In the second stage the irreversible immobilization of the microorganism on the surface starts through interactions with flagella, different types of polysaccharides and adhesive proteins. The second stage is therefore characterized by the formation of microcolonies. In the third stage the proliferation of the multilayered cell structure begins. Furthermore, extracellular polymeric substances forms and their segregation begins. The fourth stage is marked by the maturation of the biofilm, which consists of channels to distribute nutrients , but also signal molecules, which are responsible for the communication of the microorganism (*quorum sensing*) In the last stage the detachment and dispersal starts, in order to spread and colonize further surfaces.[47-49] An essential factor for the formation of biofilms is the *quorum sensing*. It is the ability of bacteria

16

to monitor their cell-population density and consequently regulate their gene expression in order to adapt to their environment concerning various physiological activities.[50-53] *Quorum sensing* occurs via secretion of signal molecules called autoinducers (AI). The chemical structure of autoinducers is mostly based on acyl homoserine lactones (AC-1) or furanosyl compounds (AC2), depending on the species of the bacteria. To prevent *quorum sensing* and thus communication between bacteria, the AIs act as a target molecule. By changing the chemical composition of the AIs, the corresponding receptors are not able to bind those, thus a reaction to the signal molecule remains absent.[50-53]
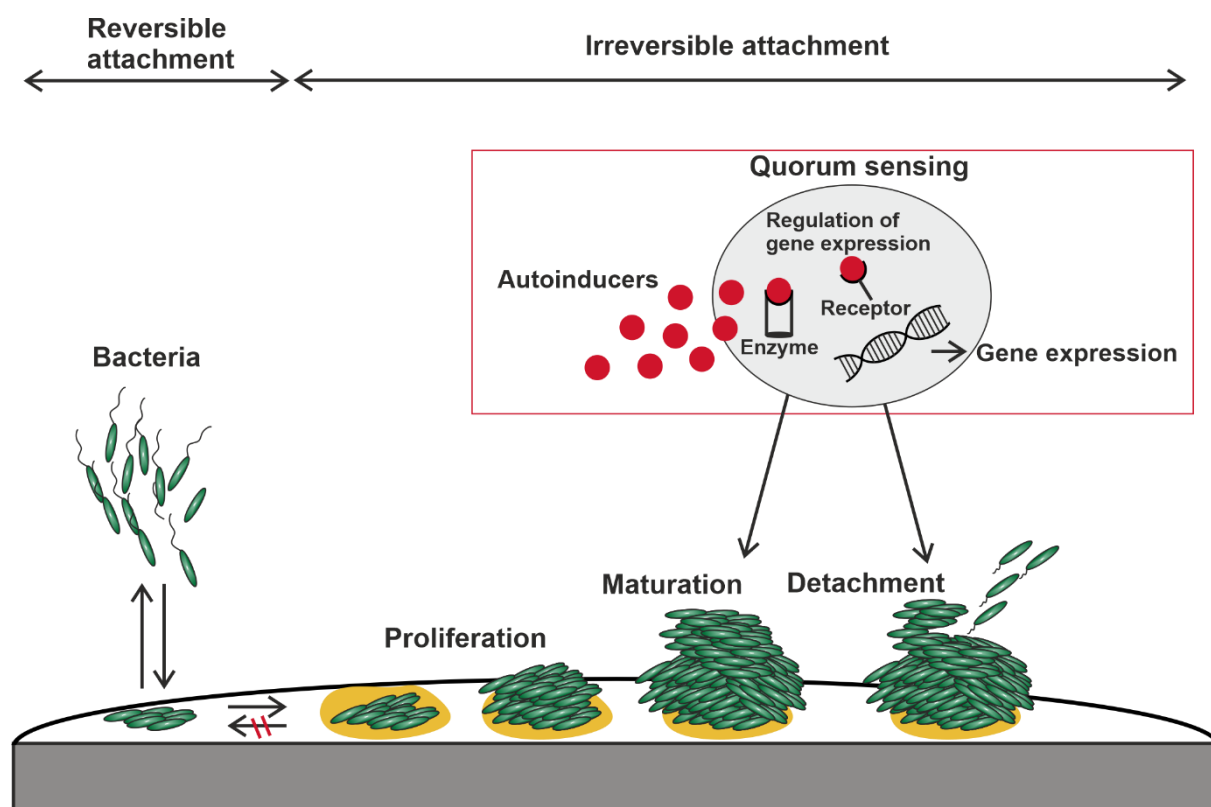
Figure 2.8. Biofilm formation with the different stages. Adapted with permission of ref [47,54].

In nature, there are numerous examples that show that *quorum sensing* can be prevented e.g. red marine algae[55] brown algae[56] or even in bacteria like *Streptomyces toyocaensis*[57]. A common mechanism in nature in order to prevent the formation of biofilms, is the oxidative halogenation of AI by haloperoxidase enzymes which consists often of iron or vanadium-based compounds.[54] Scheme 1 shows the haloperoxidase reaction.

$$\text{R-H} + H_2O_2 + H^+ + X^- \xrightarrow{\text{"HOX"}} \text{X-R} + 2\,H_2O$$

The oxidation of halides (Cl^-, Br^-, I^-) occurs through hydrogen peroxide (H_2O_2), leading to the formation of hypohalous acids, which further react with nucleophilic acceptor molecules.[54] Hypohalous acids inhibit the formation of biofilms due to halogenation of the AIs. Furthermore, they show biocidal effects caused by their oxidizing power and toxicity to various

17

microorganisms.[58] NPs can mimic native enzymes. Various materials show peroxidase – like activity, e.g., V_2O_5[59], Fe_3O_4[60], TiO_2[61] and CeO_2[62]. CeO_2 is a promising candidate, due to its non-toxic behavior and high abundance, which allows an environmentally compatible use, as well as a cost-efficient production on an industrial scale. The Belousov-Zhabotinsky reaction describes the bromination of malonic acid. During the reaction hyphohalous acids forms, due to the redox couple Ce^{3+}/Ce^{4+}.[63] Due to the non-stochiometric occurrence of Ce^{3+}/Ce^{4+} in CeO_2 NPs, the haloperoxidase activity is close related to the Belousov-Zhabotinsky reaction.[63-65] Herget et al.[62] showed a significant decrease of biofilm formation on stainless steel plates with CeO_2-nanorods, indicating a haloperoxidase-like activity of CeO_2. Furthermore, kinetic measurements showed typical Michaelis-Menten kinetics, indicating the enzyme-like behavior. Frerichs et al.[63] increased the catalytic activity by a factor of 3 through doping with Bi^{3+} in comparison to undoped CeO_2 particles. With a concentration of 270 ng/mL of $Ce_{0.8}Bi_{0.2}O_{2-\delta}$ the NPs reduced the biofilm formation by 50%. In comparison, phase pure CeO_2 NPs decreased biofilm formation by slightly more than 20%, assuming therefore a significant correlation between defect concentration and haloperoxidase activity.[63] Besides defect concentration, the catalytic activity is also determined by the surface/volume ratio, i.e., particle size, surface ligands and surface charge. Therefore, the scope of factors to further decrease the biofilm formation is significant and the potential of CeO_2 NPs has not yet been fully exploited.

2.3.3 Intercalation Batteries

The principle of a battery is to generate electrical energy from a chemical potential.[66] In recent years, the demand for rechargeable batteries, especially for use in portable devices and electric vehicles, has increased enormously. Batteries with higher capacities and a long cycle life are needed to fulfill increasingly demanding tasks. There are many different types of batteries, and in recent decades intercalation batteries have become particularly popular. Since 1990, when Sony announced the first commercial lithium-ion battery (LIB), intercalation batteries have become ubiquitous in our lives and are used in nearly every portable electronic device.[67] Figure 2.9 shows the set-up of a LIB. LIBs consist of a negative and a positive electrode and an electrolyte. Furthermore, current collectors are present. A copper foil is placed at the negative-, and aluminium foil at the positive electrode. Between the two electrodes is a separator consisting of a porous solid membrane.[68] Both electrodes are made of intercalation materials. The positive electrode is made mostly of a layered lithium metal oxid ($LiMO_2$), while the negative electrode commonly consists of graphite.[68-70] The electrolyte allows the diffusion of Li-ions from one electrode to the other, depending on the charge mode. It usually contains

18

lithium salts, additives, and organic solvents.[71] During discharge, the lithium cations in the electrolyte diffuse through the porous membrane to the positive electrode. Meanwhile, the electrons migrate to the positive current collector (aluminum foil) with the help of the negative current collector, usually a copper foil. At the positive electrode, intercalation of the lithium-ions into the metal layer oxide material begins. When the battery is charged, the migration of the lithium ions changes in the opposite direction.[68,72]

Important parameters to describe batteries in general are (i) specific capacity, (ii) specific energy and (iii) cycle life. The capacity describes the amount of energy provided during a discharge process. The unit of the capacity is Ah, while the (i) specific capacity has the unit Ah/kg, therefore it describes the capacity as a function of mass. The product of the specific capacity and the average discharge voltage gives the (ii) specific energy with the unit Wh/kg.

$$C_6 + LiMO_2 \underset{\text{Discharge}}{\overset{\text{Charge}}{\rightleftharpoons}} Li_xC_6 + Li_{(1-x)}MO_2$$
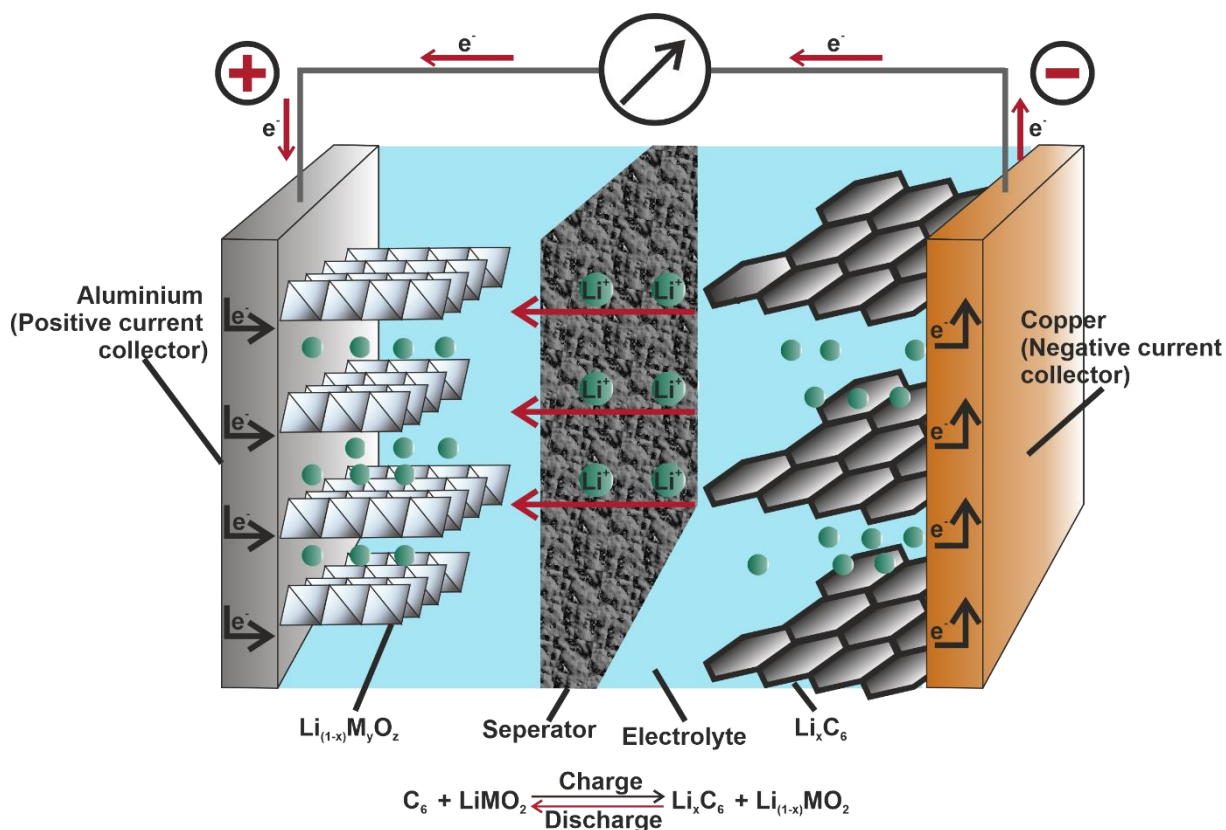
Figure 2.9. Basic principle and set up of LIBs during the discharging process. Adapted with permission of ref [68].

It describes the stored energy per gram. The energy density refers to the volume of the material and describes the stored energy per liter (Wh/L).[68] The (iii) cycle life describes the number of discharge and charge cycles before the capacity reaches the critical capacity of 80% of the original value.[73] The most commercially used material for LIBs as positive electrode material is $LiCoO_2$.[72] With a specific capacity of 190 Ah/kg at a voltage of 3.9 V, it is predestined for numerous applications e.g., for electronic devices.[74]

19

Nevertheless, some problems are associated with the material. $LiCoO_2$ is known to release oxygen at high temperatures. Therefore, safety issues can occur.[70,74] Furthermore, cobalt is relatively expensive.[72] To improve safety and reduce the price, different new materials have been developed. $LiMnO_2$ has a smaller specific capacity (110 Ah/kg) at a voltage of 4.0 V, but it is safer in terms of oxygen release and biohazard. However, the thermal stability of the material is lower, which limits its potential range of applications.[72-74] LIBs with the composition $LiNi_{1-x-y}Co_xMn_yO_2$ (NMC) and $LiNi_{1-x-y}Co_xAl_yO_2$ (NCA) offer a serious alternative to $LiCoO_2$. $LiNi_{0.8}Co_{0.1}Mn_{0.1}O_2$ shows a specific capacity of 200 Ah/kg at a voltage of 3.8 V, $LiNi_{0.8}Co_{0.15}Al_{0.05}O_2$ shows similar results(200 Ah/kg at 3.7 V). The energy density of NMC and NCA are at the level of $LiCoO_2$. Therefore, similar applications for the latter LIBs can be considered. Due to the composition, less cobalt is necessary, which reduces the price. Furthermore, NMC and NCA are known to be safer than $LiCoO_2$.[72,75-76] NMC batteries are already in commercial use, e.g., in e-bikes or electric powertrains.[77] The improvement of lithium-based batteries is a subject of current research. In terms of safety, specific capacity, energy density, cost, there is still room for improvement. In the next few decades, demand for lithium is expected to increase significantly, driven in particular by demand for electric vehicles and electronic devices.[78] Due to the limited resources of lithium, the price of the raw materials will also rise as demand increases. The development of non-lithium-based batteries is therefore essential to avoid such problems. A promising candidate are sodium-based ion batteries (SIB). The elemental abundance of sodium is around 400 times higher than lithium, increasing demand for rechargeable batteries would therefore not be a serious problem for SIBs.[79-80] Nevertheless, it should be mentioned that according to the current state of research, SIBs can be used complementary to LIBs, but not as a substitute in all respects, because the standard electrochemical potential for lithium is 3.04 V, while it is 2.71 V for sodium. Furthermore, the Shannon´s ionic radii for lithium and sodium are 0.76 Å and 1.02 Å. This leads to a smaller theoretical energy density compared to the lithium-based counterpart.[81-82] Due to the expected price increase for lithium-based raw materials in the next few years, prices for SIBs could be around 10-20% lower according to previous forecasts.[81-83] Therefore, the use of SIB batteries can be considered a more resource-efficient option in some areas. The classification of sodium layered oxides proposed by Delmas et al.[84] is subdivided into two types of structures, the O3 and P2 type. Figure 2.10 shows the different stacking order of sodium layered oxides. In general, metal layered oxides with the formula ABO_2 are made up of MO_2 layers with edge-sharing MO_6 octahedra. The cations A occupy the positions between the layers. The main difference between the O3 ($R\overline{3}m$) and P2 ($P6_3/mmc$) types is the oxide coordination of the A

20

cations and therefore the occupation of the A sites between the layers. The O3 structure type has an octahedral coordination of the Na^+ cations, while the sodium ions in the P2 structure type occupy the prismatic sites.[81]
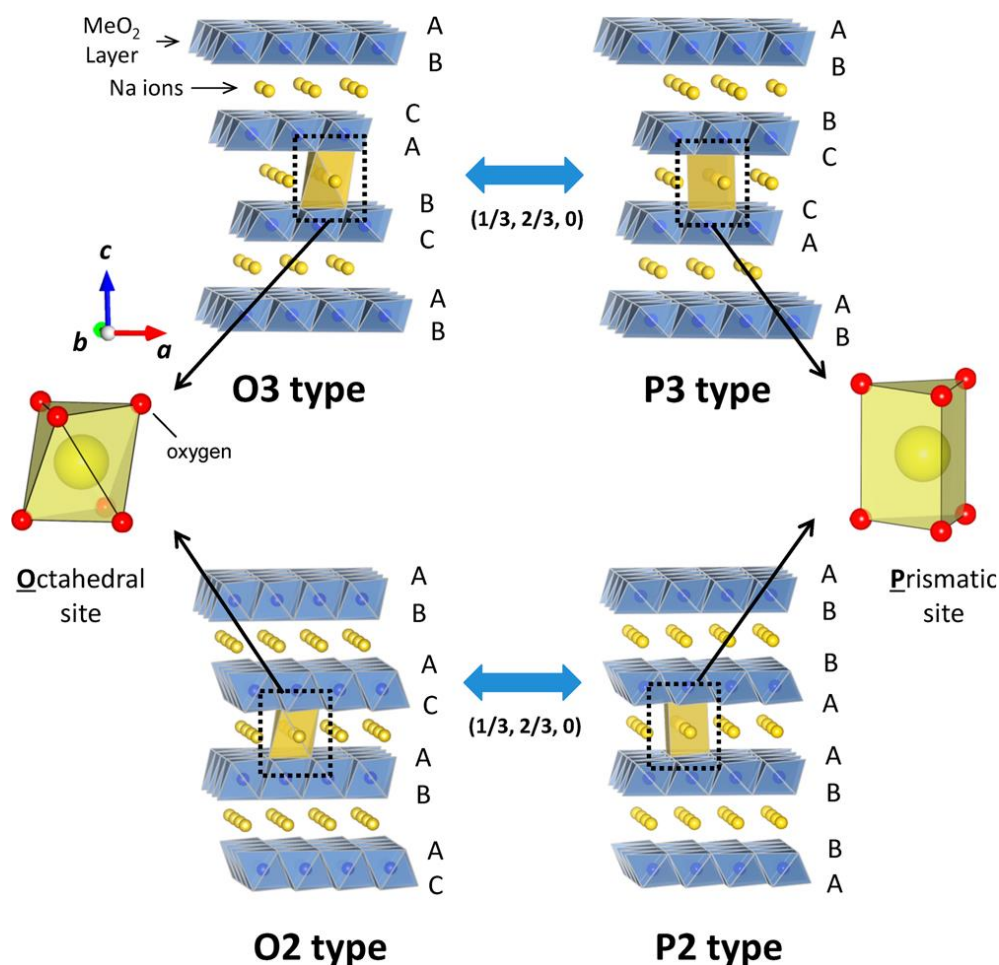
Figure 2.10. $NaMO_2$ layered oxide structures with phase transition induced due to sodium de/intercalation. Reprinted with permission from ref [81].

The O3 structure type (α-$NaFeO_2$) is build up by edge shared NaO_6 and MO_6 octahedra layers which are alternating perpendicular to the [111] direction. The MO_2 layers have the sequence: AB, CA, BC. During the deintercalation of the sodium ions a phase transition occurs from the O3 to the P3 structure type occurs, where an octahedral coordination of the Na^+ cations rather than a prismatic coordination become favored. During this phase transition the MO_2 layers change their stacking order, with an AB, BC, CA sequence after rearrangement. In the P2 structure type, the sodium cations are prismatically coordinated by oxide anions, the main difference compared to the P3 type is the stacking order (AB, BA). Through intercalation of sodium cations, a phase transition to the O2 structure type occurs *via* rearrangement of the MO_2 layers. The O2 type has the sequence AB, AC. In general, phase transitions from the O3/P3 to O2/P2 type do not occur.[81]

Various sodium-based materials have been reported as potential positive electrode materials. Table 1 shows and compares a few potential sodium-based positive electrode materials with their Li-based counterparts. The specific capacity of the sodium compounds is in general lower than that of the lithium-based materials. Therefore, intensive research efforts have been invested into sodium-based compounds in order to improve their specific capacity.

Table 2.1. Various lithium and sodium based positive electrode materials.

Material	Specific capacity (Ah/kg)	Voltage (V)	Reference
$LiCoO_2$	190	3.9	74
$LiMnO_2$	110	4.0	72
$LiNi_{0.8}Co_{0.1}Mn_{0.1}O_2$ (NMC)	210	3.8	85
$LiNi_{0.8}Co_{0.15}Al_{0.05}O_2$ (NCA)	200	3.8	85
α-$NaFeO_2$	85	3.3	86
β-$NaFeO_2$	100	0.2-4.0	87
$Na_3V_2(PO_4)_2F_3$	135	3.8	88
$NaCrO_2$	113	3.0	89

2.4 References

(1)   V. K. LaMer and R. H. Dinegar, *J. Am. Chem. Soc.*, 1950, **72**, 4847-4854.

(2).   L. Bahrig, S. G. Hickey and A. Eychmüller, *Cryst. Eng. Comm.*, 2014, **16**, 9408-9424.

(3)   S. G. Kwon and T. Hyeon, *Small*, 2011, **7**, 2685-2702.

(4)   J. Ma, S. M. Y. Lee ,C. Yi and C. W. Li, *Lab Chip*, 2017, **17**, 209-226.

(5)   Y. Song, J. Hormes and C. S. S. R. Kumar, *Small*, 2008, **4***,* 698-711.

(6)   P. R. Makgwane and S. S. Ray, *J. Nanosci. Nanotech.*, 2014, **14**, 1338-1363.

(7)   J. Wang and Y. Song, *Small*, 2017, **13**, 1604084.

(8)   V. L. M. Silva, L. M. B. F. Santos and A. M. S. Silva, *Chem. Eur. J.*, 2017, **23**, 7853-7865.

(9)   J. H. Lienhard IV and J. H. Lienhard V, *A Heat Transfer Textbook*, Phlogiston Press, Cambridge, 2020.

(10)   G. Hauke, *An Introduction to Fluid Mechanics and Transport Phenomena*, Springer, Dordrecht, 2008.

(11)   Y. Nakayama and R. F. Boucher, *Introduction to Fluid Mechanics*, Butterworth-Heinemann, Oxford, 1999.

(12)   H. F. George and F. Qureshi, in *Encyclopedia of Tribology*, ed. Q. J. Wang and Y. W. Chung, Springer, Boston, 2013, pp. 2416-2420.

(13)   G. L. Wilkes, *J. Chem. Educ.*, 1981, **59**, 880.

(14)   K. Sanaullah and A. Khan, in *Advances in Sustainable Polymer Composites*, ed. R. Rahman, Elsevier, Amsterdam, 2020, ch. 7, pp. 141-183.

(15)   T. Sochi, *Polymer*, 2010, **51**, 5007-5023.

(16)   J. X. J. Zhang and J. Hoshino, *Molecular Sensors and Nanodevices*, Elsevier, Amsterdam, 2014.

(17)   C. Loudon and K. McCulloh, *Ann. Entomol. Soc. Am.*, 1999, **92**, 153-158.

(18)   A. Ostadfar, *Biofluid Mechanics Principle and Applications*, Elsevier, Amsterdam, 2016.

(19)   N. Westerhof, N. Stergiopulos, M. I. M. Noble and B. E. Westerhof, *Snapshots of Hemodynamics*, Springer, Cham, 2019.

(20)   J. M. Berg and T. Dallas, in *Encyclopedia of Microfluidics and Nanofluidics*, ed. D. Li, Springer, New York, 2nd edn, 2015, pp. 2693-2701.

(21).   M. C. C. Llaurado, PhD thesis, Universitat Rovira I Virgili, 2007.

(22)   F. Shahidi and Y. Zhong, *Chem. Soc. Rev.*, 2010, **39**, 4067-4079.

(23)   G. Niu, A. Ruditskiy, M. Vara and Y. Xia, *Chem. Soc. Rev.*, 2016, **44**, 5806-5820.

(24)   A. Larrea, V. Sebastian, A. Ibarra, M. Arruebo and J. Santamaria, *Chem. Mater.*, 2016, **27**, 4254-4260.

(25)   D. Kumar, H. Sing, S. Jouen, B. Hannoyer and S. Banerjee, *RSC Adv.*, 2015, **5**, 7138-7150.

(26)   F. Sayed and V. Polshettiwar, *Sci. Rep.*, 2015, **5**, 9733.

(27)   F. Yazdani and M. Seddigh, *Mat. Chem. Phys.*, 2016, **184**, 318-323.

(28)   N. S. Gajbhiye, S. Sharma, A. K. Nigam and R. S. Ningthoujam, *Chem. Phys. Lett.*, 2008, **466**, 181-185.

(29)   A. Heuer-Jungemann, N. Feliu, I. Bakaimi, M. Hamaly, A. Alkilany, I. Chakraborty, A. Masood, M. F. Casula, A. Kostopoulou, E. Oh, J. Susumu, M. H. Stewart. I. L. Medintz, E. Stratakis, W. J. Parak and A. G. Kanaras, *Chem. Rev.*, 2019, **119**, 4819-4880.

(30)   Z. Xu, C. Shen, Y. Hou, H. Gao and S. Sun, *Chem. Mater.*, 2009, **21**, 1778-1780.

(31) L. Pérez-Mirabet, E. Solano, F. Martínez-Julián, R. Guzmán, J. Arbiol, T. Puig, X. Obradors, A. Pomar, R. Yáñez, J. Ros and S. Ricart, *Mater. Res. Bull.*, 2013, **48**, 966-972.

(32) H. S. Dehsari, R. A. Harris, A. H. Ribeiro, W. Tremel and K. Asadi, *Langmuir*, 2018, **34**, 6582-6590.

(33) S. Sun, H. Zeng, D. B. Robinson, S. Raoux, P. M. Rice, S. X. Wang and G. Li, *J. Am. Chem. Soc.*, 2004, **126**, 273-279.

(34) L. T. Lu, N. T. Dung, L. D. Tung, C. T. Thanh, O. K. Quy, N. V. Chuc, S. Maenosono and N. T. K. Thanh, *Nanoscale*, 2015, **7**, 19596-19610.

(35) M. H. Hussain, N. F. Abu Bakar and A. N. Mustapa, *Nanoscale Res. Lett.*, 2020, **15**, 140.

(36) N. Gacem and P. Diao, *Colloids Surf. A Physiochem. Eng. Asp.*, 2013, **417**, 32-38.

(37) S. Leekumjorn, S. Gullapalli and M. S. Wong, *J. Phys. Chem. B*, 2012, **116**, 13063-13070.

(38) J. Song, D. Kim and D. Lee, *Langmuir*, 2011, **27**, 13854-13860.

(39) M. Niederberger and N. Pinna, *Metal Oxide Nanoparticles in Organic Solvents*, Springer, London, 2009.

(40) N. T. K. Thanh, N. Maclean and S. Mahiddine, *Chem. Rev.*, 2014, **114**, 7610-7630.

(41) H. S. Dehsari, M. Heidari, A. H. Ribeiro, W. Tremel, G. Jakob, R. Potestio and K. Asadi, *Chem. Mater.*, 2017, **29**, 9648-9656.

(42) V. C. Karade, T. D. Dongale, S. C. Sahoo, P. Kollu, A. D. Chougale, P. S. Patil and P. B. Patil, *J. Phys. Chem. Solids*, 2018, **120**, 161-166.

(43) M. Nakaya, R. Nishida and A. Muramatsu, *Molecules*, 2014, **19**, 11395-11403.

(44) H. S. Wasly, M. S. Abd El-Sadek and M. Henini, *Appl. Phys. A.*, 2018, **124**.

(45) S. Mohan, M. Vellakkat, A. Aravind and R. U, *Nano Ex.*, 2020, **1**.

(46) M. Vert, Y. Doi, K. H. Hellwich, M. Hess, P. Hodge, P. Kubisa, M. Rinaudo and F. Schué, *Pure Appl. Chem.*, 2012, **84**, 377-410.

(47) R. Subramani, M. Jayaprakashvel, in *Implication of Quorum Sensing and Biofilm Formation in Medicine, Agriculture and Food Industry*, ed. P. Bramhachari, Springer, Singapore, 2019, pp. 11-20.

(48) W. Yin, Y. Wang, L. Liu and J. He, *Int. J. Mol. Sci.*, 2019, **20**, 3423.

(49) L. Yi, M. Jin, J. Li, D. Grenier and Y. Wang, *Appl. Microbiol. Biotechnol.*, 2020, **104**, 8649-8660.

(50) M. B. Miller and B. L. Bassler, *Annu. Rev. Microbiol.*, 2001, **55**, 165.

(51)   A. Camilli and B. L. Bassler, *Science*, 2006, **311**, 1113.

(52)   W. R. J. D. Galloway, J. T. Hodgkinson, S. D. Bowden, M. Welch and D. R. Spring, *Chem. Rev.*, 2011, **111**, 28-67.

(53)   B. L. Bassler and R. Losick, *Cell*, 2006, **125**, 237-246.

(54)   K. Herget, H. Frerichs, F. Pfitzner, M. N. Tahir and W. Tremel, *Adv. Mater.*, 2018, **30**, 1707073.

(55)   M. Manefield, R. Nys, K. Naresh, R. Roger, M. Givskov, S. Peter and S. Kjelleberg, *Microbiol.*, 1999, **145**, 283-291.

(56)   M. Almeida, S. Filipe, M. Humanes, M. F. Maia, R. Melo, N. Severino, J. A. L. da Silva, J. J. R. Fraústo da Silva and R. Wever, *Phytochem.*, 2001, **57**, 633-642.

(57)   G. C. Marshall and G. D. Wright, *Biochem. Biophys. Res. Commun.*, 1996, **219**, 580-583.

(58)   S. A. Borchardt, E. J. Allain, J. J. Michels, G. W. Stearns, R. F. Kelly and W. F. McCoy, *Appl. Environ. Microbiol.*, 2001, **67**, 3174-3179.

(59)   F. Natalio, R. André, A. F. Hartog, B. Stoll, K. P. Jochum, R. Wever and W. Tremel, *Nature Nanotech.*, 2012, **7**, 530-535.

(60)   H. Wei and E. Wang, *Anal. Chem.*, 2008, **80**, 2250-2254.

(61)   B. Khorshidi, I. Biswas, T. Ghosh, T. Thundat and M. Sadrzadeh, *Sci. Rep.*, 2018, **8**.

(62)   K. Herget, P. Hubach, S. Pusch, P. Deglmann, H. Götz, T. E. Gorelik, I. A. Gural´skiy, F. Pfitzner, T. Link, S. Schenk, M. Panthöfer, V. Ksenofontov, U. Kolb, T. Opatz, R. André and W. Tremel, *Adv. Mater.* 2017, **29**, 1603823.

(63)   H. Frerichs, E. Pütz, F. Pfitzner, T. Reich, A. Gazanis, M. Panthöfer, J. Hartmann, O. Jegel, R. Heermann and W. Tremel, *Nanoscale*, 2020, **12**, 21344-21358.

(64)   N. J. Lawrence, J. R. Brewer, L. Wang, T. S. Wu, J. Wells-Kingsbury, M. M. Ihrig, G. Wang, Y. L. Soo, W. N. Mei and C. L. Cheung, *Nano Lett.*, 2011, **11**, 2666-2671.

(65)   V. Baldim, F. Bedioui, N. Mignet, I. Margaill and J. F. Berret, *Nanoscale*, 2018, **10**, 6971-6980.

(66)   R. C. Massé, C. Liu, Y. Li, L. Mai and G. Cao, *Nat. Sci. Rev.*, 2017, **4**, 26-53.

(67)   J. Xie and Y.C. Lu, *Nat. Commun.*, 2020, **11**, 2499.

(68)   R. Korthauer, *Lithium-Ion Batteries: Basics and Applications*, Springer, Berlin Heidelberg, 2018.

(69)   S. W. Kim, D. H. Seo, X. Ma, G. Ceder and K. Kang, *Adv. Energy Mater.*, 2012, **2**, 710-721.

(70)   K. Ozawa, *Solid State Ion.*, 1994, **69**, 212-221.

(71)   Q. Li, J. Chen, L. Fan, X. Kong and Y. Lu, *Green Energy Environ.*, 2016, **1**, 18-42.

(72)   S. Xin, H. Gao and Y. G. Guo, in *Nanostructures and Nanomaterials for Batteries*, ed. Y. G. Guo, Springer, Singapore, 2019, pp. 29-87.

(73)   H. Wenzl, in *Encyclopedia of Electrochemical Power Sources*, ed. J. Garche, C. Dyer, P. Moseley, Z. Ogumi, D. Rand and B. Scrosati, Elsevier, Amsterdam, 2009, pp. 552-558.

(74)   Y. Lyu, X. Wu, K. Wang, Z. Feng, T. Cheng, Y. Liu, M. Wang, R. Chen, L. Xu, J. Zhou, Y. Lu and B. Guo, *Adv. Energy Mater.*, 2020, **11**, 2000982.

(75)   K. G. Gallagher, P. A. Nelson, in *Lithium-Ion Batteries*, ed. G. Pistoia, Elsevier, Amsterdam, 2014, pp. 97-126.

(76)   G. Patry, A. Romagny, S. Martinet and D. Froelich, *Energy Sci. Eng.*, 2014, **3**, 71-82.

(77)   A. Accardo, G. Dotelli, M. L. Musa and E. Spessa, *Appl. Sci.*, 2021, **11**, 1160.

(78)   S. Ziemann, D. B. Müller, L. Schebek and M. Weil, *Resour. Conserv. Recy.*, 2018, **133**, 76.

(79)   A. V. Naumov and M. A. Naumova, *Russ. J. Non-Ferr. Met.*, 2010, **51**, 324-330.

(80)   K. H. Wedepohl, *Geochim. Cosmochim. Acta*, 1995, **59**, 1217-1232.

(81)   N. Yabuuchi, K. Kubota, M. Dahbi and S. Komaba, *Chem. Rev.*, 2014, **114**, 11636-11682.

(82)   K. M. Abraham, *ACS Energy Lett.*, 2020, **5**, 3544-3547.

(83)   C. Vaalma, D. Buchholz, M. Weil and S. Passerini, *Nat. Rev. Mater*, 2018, **3**, 18013.

(84)   C. Delmas, C. Fouassier and P. Hagenmüller, *Physica B+C*, 1980, **99**, 81-85.

(85)   J. F. Peters, A. P. Cruz and M. Weil, *Batteries*, 2019, **5**, 10.

(86)   J. Zhao, L. Zhao, N. Dimov, S. Okada and T. Nishida, *J. Electrochem. Soc.*, 2013, **160**, A3077.

(87)   L. Durai, A. Gopalalkrishnan and S. Badhulika, *Mater. Lett.*, 2020, **270**, 127739.

(88)   K. M. Abraham, *ACS Energy Lett.*, 2020, **5**, 3544-3547.

(89)   Y. Wang, W. Li, G. Hu, Z. Peng, Y. Cao, H. Gao, K. Du and J. B. Goodenough, *Chem. Mater.*, 2019, **31**, 5214-5223.

3. Selective Synthesis of Monodisperse CoO Nanooctahedra as Catalysts for Electro-chemical Water Oxidation
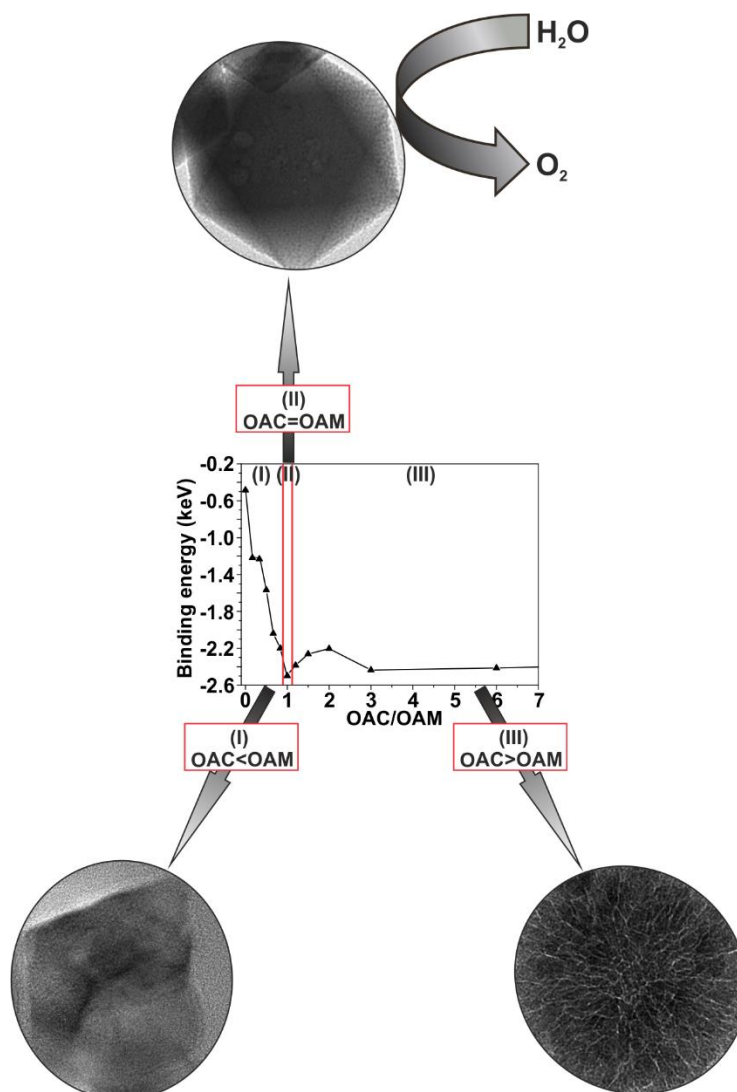
The following chapter is an adapted reproduction from the reference Langmuir, 2020, 36, 13804-13816. It is reproduced with the permission of the American Chemical Society. In the appendix of the dissertation a detailed authorship statement with the contributions of each author is attached.

3.1. Abstract

Thermal decomposition is a promising route for the synthesis of metal oxide nanoparticles because size and morphology can be tuned by minute control of the reaction variables. We synthesized CoO nanooctahedra with diameters of ~48 nm and a narrow size distribution. Full control over nanoparticle size and morphology could be obtained by controlling the reaction time, surfactant ratio, and reactant concentrations. We show that the particle size does not increase monotonically with time or surfactant concentration but passes through minima or maxima. We unravel the critical role of the surfactants in nucleation and growth and rationalize the observed experimental trends in accordance with simulation experiments. The as-synthesized CoO nanooctahedra exhibit superior electrocatalytic activity with long-term stability during oxygen evolution. The morphology of the CoO particles controls the electrocatalytic reaction through the distinct surface sites involved in the oxygen evolution reaction.

3.2. Introduction

The synthesis of well-defined nanocrystals is a central topic in inorganic chemistry. It is vital for applications in areas ranging from catalysis to energy storage, sensing, and nanomedicine. Small nanocrystals have large surface area/volume ratios. This leads to unsaturated and thus reactive surface atoms and short diffusion pathways, which allows for application in heterogeneous catalysis,[1–6] as battery materials,[7,8] or as contrast agents for magnetic resonance imaging.[9–11]

Nanomaterials can be synthesized by physical (top-down) or chemical (bottom-up) approaches. While the physical approach breaks down bulk materials into nanoscale objects, the chemical approach builds up a structure atom-by-atom, molecule-by-molecule, or cluster-by-cluster from solution. This wet-chemical approach is appealing because of its simplicity and usually narrow distribution of particle sizes, and it has reached a level of synthetic control that has a benefit for nanotechnological applications.[10,12,13] Metal and metal oxide nanocrystals can be made in non agglomerated form with well-defined sizes and morphologies by utilizing surfactants as protective shells. This is in stark contrast to the agglomerated materials with ill-defined morphologies obtained from the gas phase,[14] spark-discharge,[15] or laser ablation[16] reactions.

Gas phase approaches are relevant for applied science because they enable scalability up to industrial quantities with high chemical purity and crystallinity.

The control of size and morphology is crucial as they determine the surface structure of nanocrystals. The ability to engineer nanocrystal size may ultimately allow the tuning of solid state reactivity, e.g., for electrode materials or catalytic reactivity and selectivity (water-splitting reactions).[17–20] This is valuable when preparing colloidal nanocrystals with metal oxides because the interplay between reactivity and surface structure is well-understood from single-particle studies (TiO$_2$, MnO, Fe$_3$O$_4$, CoO, Co$_3$O$_4$, ZnO).[21–26] Many metal oxides are employed as catalysts in a large number of industrial-scale catalytic processes.[23,27] Cobalt monoxide (CoO) nanoparticles are significant because of their potential application based on magnetic, catalytic, and gas-sensing properties.[28–34] CoO adopts the rock-salt structure and is antiferromagnetic. Particle size and crystal structure affect its magnetic properties. It is present typically as a thin shell on ferromagnetic cobalt particles that exceeds the superparamagnetic limit of small cobalt clusters due to magnetic exchange coupling.[28] Wurtzite-type CoO has been prepared and studied as an "end member" of the solid solution series Zn$_{1-x}$Co$_x$O[35] because transition-metal-substituted semiconductors can exhibit ferromagnetism with high Curie temperatures.[36] Pure CoO nanocrystals are difficult to prepare because the surface of nanoscale CoO is oxidized easily,[37] which affects the product quality of hydro/solvothermal,[38] organic,[39] and condensation[40] reactions. CoO nanocrystals with rock-salt and wurtzite structure have been prepared by the reduction of Co(acac)$_3$ in oleylamine,[41] similarly as for monodisperse MnO and FeO$_x$ nanoparticles.[42–44]

In this process, where oleic acid (OAC) is used together with oleylamine (OAM), we analyzed the behavior of the surfactants on the phase composition and morphology of the CoO particles. The organic solvent prevents the precipitation of metal hydroxides, and the thermolysis of molecular precursors leads to a controlled formation of particles with specific size, morphology, phase selectivity, crystallinity, and surface coordination.[45]

Much effort has been devoted to understand how particle size,[42,46–48] phase composition,[45,49,50] and morphology[48,51] can be tuned by a careful choice of solvents and capping agents. Morphology control is an important goal because facet-dependent reactivity and stability of cobalt oxides have been reported for the oxygen evolution reaction (OER),[52,53] which has a slow kinetics and poor energy efficiency due to the overpotential associated with the four-electron reaction $2H_2O = 4H^+ + O_2 + 4e^-$ (in acidic media) or $4OH^- = 2H_2O + O_2 + 4e^-$ (in alkaline media). Cobalt oxalate microcrystals with distinct morphologies have been employed for catalyzing the OER in alkaline solution[54] with the goal to replace precious metal oxides

(IrO_2, RuO_2) as the electrocatalyst.[55] Similarly, $Co(OH)_2$, CoO and $Co@CoO_x$ nanomaterials have shown promising results for electrocatalytic water oxidation.[56−58]

The thermal decomposition of labile molecular precursors is an appealing route for the synthesis of monodisperse nanocrystals. Still, the apparent simplicity of the synthesis is counterbalanced by the complex interplay of reaction variables that determine the final particle size, composition, and morphology. We have studied recently the effects of concentration, reaction time, and surfactants (OAC and OAM) on growth, size, and monodispersity of manganese and iron oxide particles.[42,45−48] Precursor concentrations and the reaction temperature control the nanoparticle size, while the surfactants control the reaction kinetics by binding to the growing particle surfaces, where they play a critical role in their morphology and size distribution. Finding optimum conditions is therefore a crucial task. Here, we present a detailed experimental and theoretical study for the synthesis of CoO nanooctahedra with different sizes. Reaction time, surfactants ratio, and concentrations of the precursors were experimental variables whose effects on the resulting CoO nanocrystals were screened and unravelled. The CoO nanooctahedra are efficient electrocatalysts for the electrochemical splitting of water.

3.3. Results and Discussion

Synthesis of CoO Nanoparticles. In the first step, the synthesis of CoO nanoparticles was studied and optimized. Because of its solubility, $Co(OAc)_2$ was used as the metal precursor with the capping ligands OAC and OAM. Nonpolar 1-octadecene (ODE) was used as the solvent and heated up to 330 °C with a fixed temperature profile. The reaction of $Co(OAc)_2$ to CoO could be traced even visually by a color change of the solution (Figure 3.9 SI) from purple (Co^{2+} precursor) at ∼65 °C to blue at 330 °C, indicating the formation of $Co(OH)_2$. During the cooling process, the color changed to brown, which indicates the formation of CoO by a condensation reaction of $Co(OH)_2$. By changing either the reaction time or the concentration of the ligands, the formation of CoO nanoparticles could be tuned.

Insight into the formation of the CoO nanoparticles was obtained by (i) varying the precursor concentrations while keeping the ratio of the OAC and OAM surfactants at a constant 1:1 ratio (series A) and (ii) varying the reaction times from 15 min up to 60 min (series B and C). (iii) In another trial run (series D) the ratio of the OAC and OAM surfactants was varied while keeping the total amount of the ligands constant. (iv) In a last set of experiments (series E and F) the concentration effect of each individual ligand was studied (Table 3.1). From the results of these experiments (series A− F), it can be concluded that in a first step $Co(OAc)_2$ dissolves in ODE.

30

Increasing the temperature leads to ligand exchange between acetate and OAC, indicated by the formation of a purple viscous mass that was obtained after very short reaction times. OAM acts as a nucleophile leading to the decomposition of a Co intermediate. The color change to blue indicates that the decomposition occurs at 330 °C and $Co(OH)_2$ was formed. Maintaining the reaction temperature at 330 °C leads to the formation of CoO through the condensation reaction of $Co(OH)_2$ as indicated by the color change from blue to brown. In the next sections, the effects of reaction time, surfactant concentration, and surfactant ratio on the product composition, morphology, and polydispersity are analyzed in detail.

Surfactant Concentration. The progress of the reaction depends on the total amount and the ratio of the surfactants. The resulting CoO nanoparticles showed systematic changes in size and morphology. The color of the solution allowed tracking of the reaction even visually. The effect of the total amount of the surfactants was analyzed in series A, for a fixed reaction time of 60 min and a reaction temperature of 330 °C with 1 mmol of $Co(OAc)_2$ in 10 mL of ODE and a constant surfactant ratio of 1:1 (OAC:OAM). Each surfactant was increased stepwise from 3 to 12 mmol (Figure 3.1).
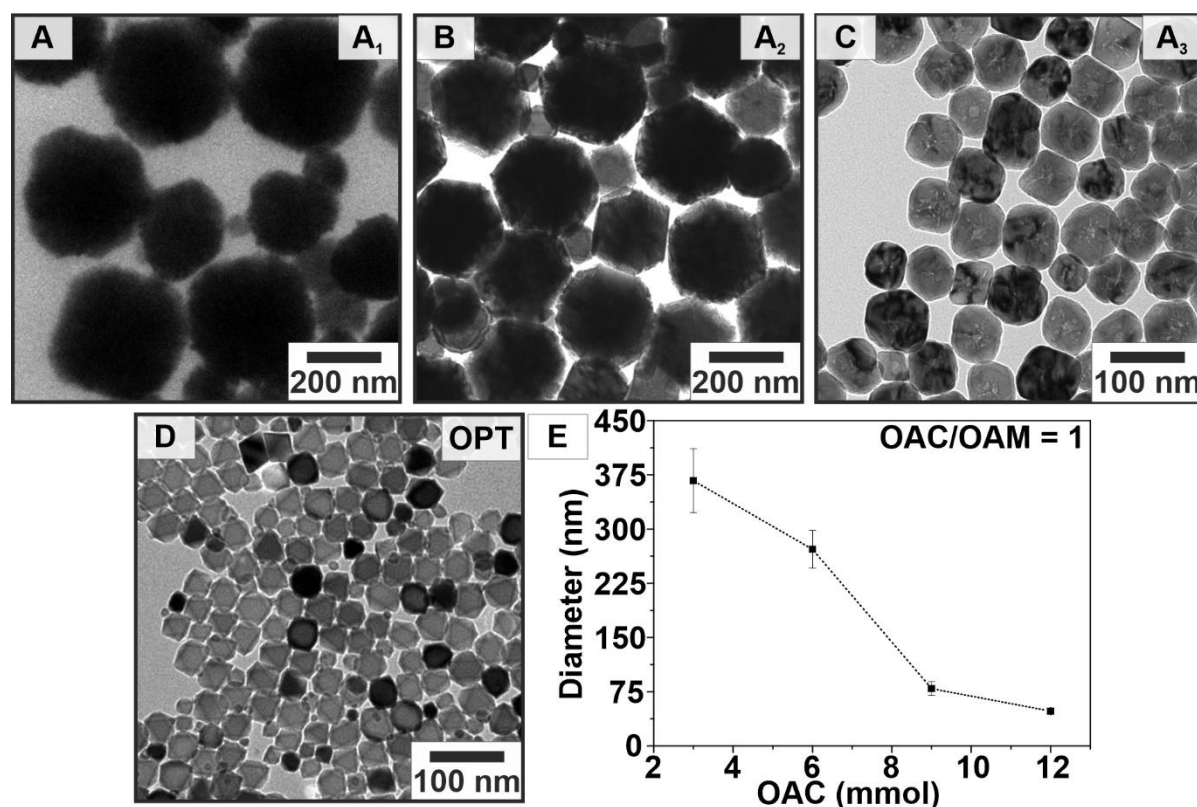

Figure 3.1. TEM images of series A: (A) concentration of OAC:OAM 3:3, (B) 6:6, (C) 9:9, and (D) 12:12. (E) Size evolution as a function of OAC concentration.

The color of the reaction solution showed a full conversion to brown CoO for all ligand concentrations. At a concentration of 3 mmol for each surfactant, agglomerates with

367 ± 44 nm (Figure 3.1A, A_1, PDI = 12%) were obtained. By increasing the amount of the surfactants, the agglomerates had diameters of $272 \pm 2\ 6$ nm (Figure 3.1B, A_2, PDI = 10%), while for reactions with 9 mmol of ligand, nanoparticles with diameters of 79 ± 9 nm (Figure 3.1C, A_3, PDI = 12%) were obtained. By increasing the amount of both surfactants to the optimum concentration of 12 mmol, the diameter of the nanoparticles further decreased to 48 ± 3 nm (Figure 3.1D, optimized synthesis (OPT), PDI = 6%). The corresponding particle size distribution is shown in Figure 3.10 (SI). After the total amount of the surfactants was increased at a fixed 1:1 ratio, the nanoparticles showed a continuous decrease in size (Figure 3.1E). OAM is known to facilitate thermal decomposition.[42] Thus, increasing the OAM concentration leads to a higher number of nuclei and to smaller particles. An increase of the OAC concentration led to a better surface stabilization and prevented particle agglomeration, resulting in nanoparticles with smaller size. By changing the concentration of the surfactants, we could control size and shape to obtain the CoO nanoparticles with almost perfect octahedral morphology at an optimum surfactant concentration.

Reaction Time. The effect of reaction time was analyzed with 1 mmol of $Co(OAc)_2$ in 10 mL of ODE at a reaction temperature of 330 °C with 3 mmol (B) and 12 mmol (C) of each OAC and OAM. It was changed in steps of 15 min up to an hour of reaction time. Starting with series B, we obtained particles with diameters of 91 ± 8 nm (Figure 3.11A (SI), B_1, PDI = 9%) after 15 min; the particle diameter decreased after 30 min to 75 nm $\pm$ 10 nm (Figure 3.11B (SI), B_2, PDI = 13%) and increased again to 120 ± 21 nm (Figure 3.11C (SI), B_3, PDI = 18%) after a reaction time of 45 min. Large agglomerates with diameters of 367 ± 55 nm (Figure 3.11D (SI), $B_4 = A_4$, PDI = 16%) were obtained after 60 min. In summary, series B reveals that the particle size steadily increases from 30 to 60 min, while the PDI remains large (Figure 3.11E). Increasing the reaction time leads to an agglomeration of the particles caused by the low concentration of the surfactant, which is not able to cover the particles sufficiently anymore. The lowest polydispersity was obtained after 15 min of reaction time (B_1, PDI = 9%). The particle size distribution for each individual synthesis is shown in Figure 3.12 (SI). In series C (Figure 3.13 (SI)) the reaction time was varied in the presence of 24 mmol of the capping ligands (12 mol each). No nanoparticles were obtained after 15 min (C_1). The formation of a purple product indicated that the reaction slowed down. Nanoparticles with diameters of 80 ± 17 nm (Figure 3.13A (SI), C_2, PDI = 21%) were obtained after 30 min. The color changed from purple to blue and finally to brown. Therefore, a longer reaction time was needed for higher concentrations of the capping ligand. The particle diameter decreased to 70 ± 11 nm (Figure 3.13B (SI), C_3, PDI = 16%) after 45 min. After 60 min the diameter and the

polydispersity decreased to 48 ± 3 nm (Figure 3.13C (SI), C_4/OPT, PDI = 6%). The particle size distribution of each synthesis is shown in Figure 3.14 (SI). A higher concentration of capping ligands in series C led to longer reaction times (compared to series B). By changing the reaction time from 30 to 45 and 60 min, the PDI value and the particle size decreased steadily. The lowest PDI values were obtained for 60 min reaction time (C_4/OPT, PDI = 6%). Compared to reaction times of 30 and 45 min, the particles obtained after 60 min showed a morphologically well-defined structure. The CoO nanoparticles exhibited an octahedral morphology (Figure 3.1D), which could not be obtained after any other reaction time. In comparison to series B, we were able to suppress the agglomeration of the nanoparticles at 60 min, by using an optimum concentration of 12 mmol OAC and OAM each, instead of 3 mmol each.

Surfactant Ratio. The composition of the surfactant mixture may affect the size, morphology, and even the crystal structure of the nanoparticles. This was analyzed in different test series with 1 mmol of $Co(OAc)_2$ in 10 mL of ODE and a reaction time of 60 min at 330 °C. In series D a constant amount of 24 mmol of the surfactants was used, while the surfactant ratios were varied systematically in steps of 3 mmol, starting with 24 mmol of OAC and no OAM to 24 mmol of OAM and no OAC, respectively. The formation of CoO ceased when the OAC/OAM ratio was >1. For an OAC/OAM ratio of 24:0 (D_1) to 15:9 (D_4), no CoO was obtained (series D, Table 3.1 (SI), D_1−D_4). For an OAC/ OAM ratio of 12:12, we obtained octahedral shaped nanoparticles (OPT). Decreasing the OAC/OAM ratio to <1 lead in general to the formation of elemental cobalt (Co) as a side or main product, depending on the exact ratio. An OAC/OAM ratio of 9:15 led to the formation of well-defined nanoparticles with a size of 38 nm $\pm$ 5 nm (Figure 3.2A, D_6, PDI = 13%).
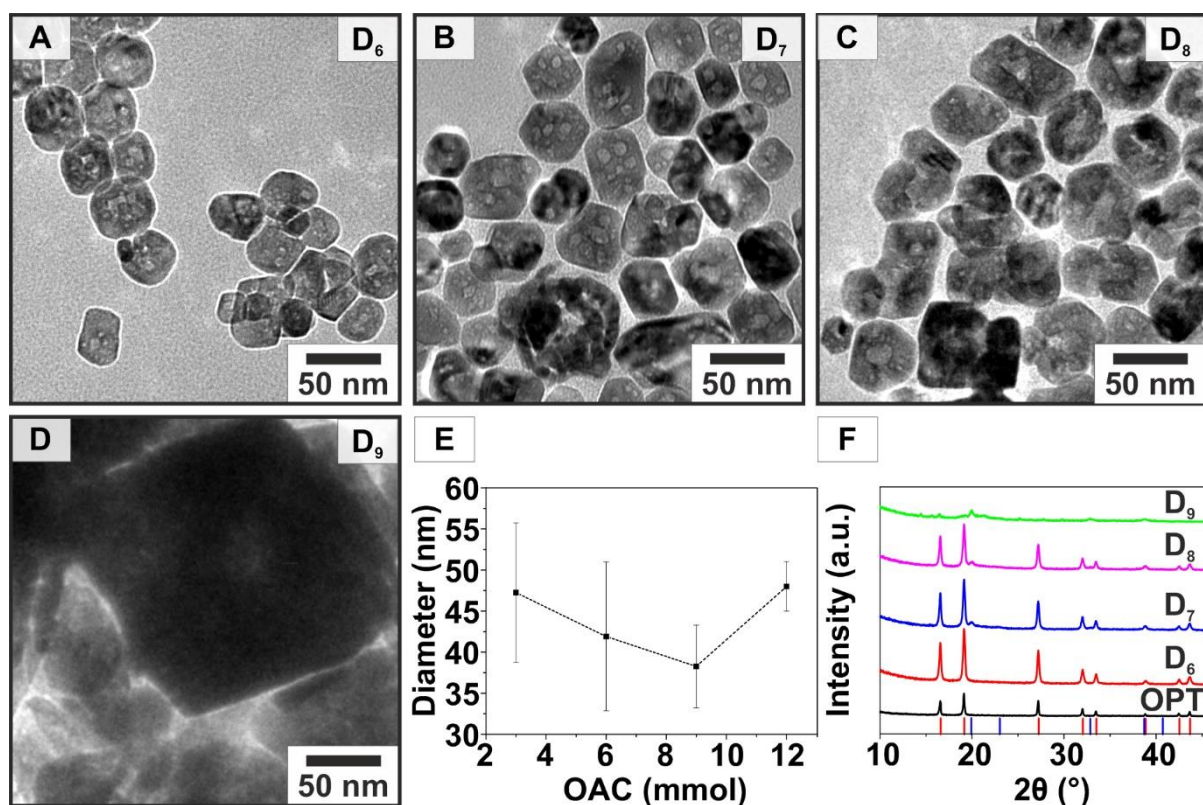
Figure 3.2. TEM images of series D: (A) concentration of OAC:OAM 9:15, (B) 6:18, (C) 3:21, and (D) 0:24. (E) Size evolution of the nanoparticles, while the total concentration of OAC and OAM is 24 mmol. (F) XRD pattern of series D with reflections of CoO (red ticks) and elemental Co (blue ticks).

Besides the main product CoO, a small amount of elemental Co was formed (D_6, Figure 3.2F). By decreasing the OAC/OAM ratio to 6:18, CoO nanoparticles with a size of 42 nm ± 9 nm (Figure 3.2B, D_7, PDI = 22%) were obtained, again with impurities of elemental Co. A further decrease of the OAC/OAM ratio to 3:21 still led to the formation of well-defined nanoparticles with an average diameter of 47 nm ± 8 nm (Figure 3.2C, D_8, PDI = 18%). In the presence of pure OAM, nanoparticles with ill-defined morphologies were obtained (Figure 3.2D, D_9). Due to the reducing properties of OAM and the absence of OAC, no CoO was formed and the sample contained only elemental Co (D_9, Figure 3.2F)

We assume that the OAC surfactant forms labile complexes with Co^{2+} cations which are decomposed at elevated temperature. In addition, it interacts with the growth species during the thermal decomposition of the cobalt intermediate. This affects the size and morphology of the resulting nanoparticles. An optimized ratio of the surfactants is essential, as it strongly affects the CoO formation kinetics. The diameter of the CoO nanoparticles decreased when the OAC/OAM ratio increased, until a 1:1 ratio (Figure 3.2E), indicating a significant change in the kinetics, by using the same concentration of OAC and OAM.

OAM has reducing properties and no strong affinity for oxide surfaces. Therefore, elemental Co was formed besides CoO for OAC/OAM ratios up to 9:15. By increasing the OAC/OAM ratio, the unprotonated OAM concentration was reduced through the acid−base equilibrium $OAC + OAM = OAC^- + OAMH^+$. As a result, the reducing properties are weakened, and no elemental Co was formed. An equal amount of OAC and OAM is required to prevent the formation of phases other than CoO. We further studied the effect of the OAC/OAM composition to substantiate this hypothesis by changing the concentrations of one ligand, while keeping the concentration of the other one constant.

Variable Amount of OAM with Constant OAC Concentration. The effect of the OAC concentration as a capping ligand was analyzed in a test series with a constant amount of OAC. For this purpose, 1 mmol of $Co(OAc)_2$ was dissolved in 10 mL of ODE for a reaction time of 60 min at 330 °C. In series E the amount of OAC was set to 12 mmol, while the amount of OAM was varied from 0 to 12 mmol in steps of 3 mmol. Nanoparticle formation ceased with decreasing OAM concentration, indicating that OAM is needed to facilitate the thermal decomposition of the cobalt intermediates. The products of each synthesis in series E were characterized by TEM; the yield was not sufficient to allow X-ray diffraction analysis. Starting with the optimized ratio of 12:12 OAC/ OAM (Figure 3.3A, OPT), the OAM concentration was stepwise decreased. With an OAM concentration of 9 mmol, the particle diameters were 149 ± 16 nm (Figure 3.3B, E_4, PDI = 11%). By further decrease of OAM (6 mmol), only a few particles with average diameters of 119 ± 18 nm (Figure 3.3C, E_3, PDI = 15%) were obtained. For a low concentration of OAM (E2, 3 mmol) and in the absence of OAM (E1), no nanoparticles were formed.
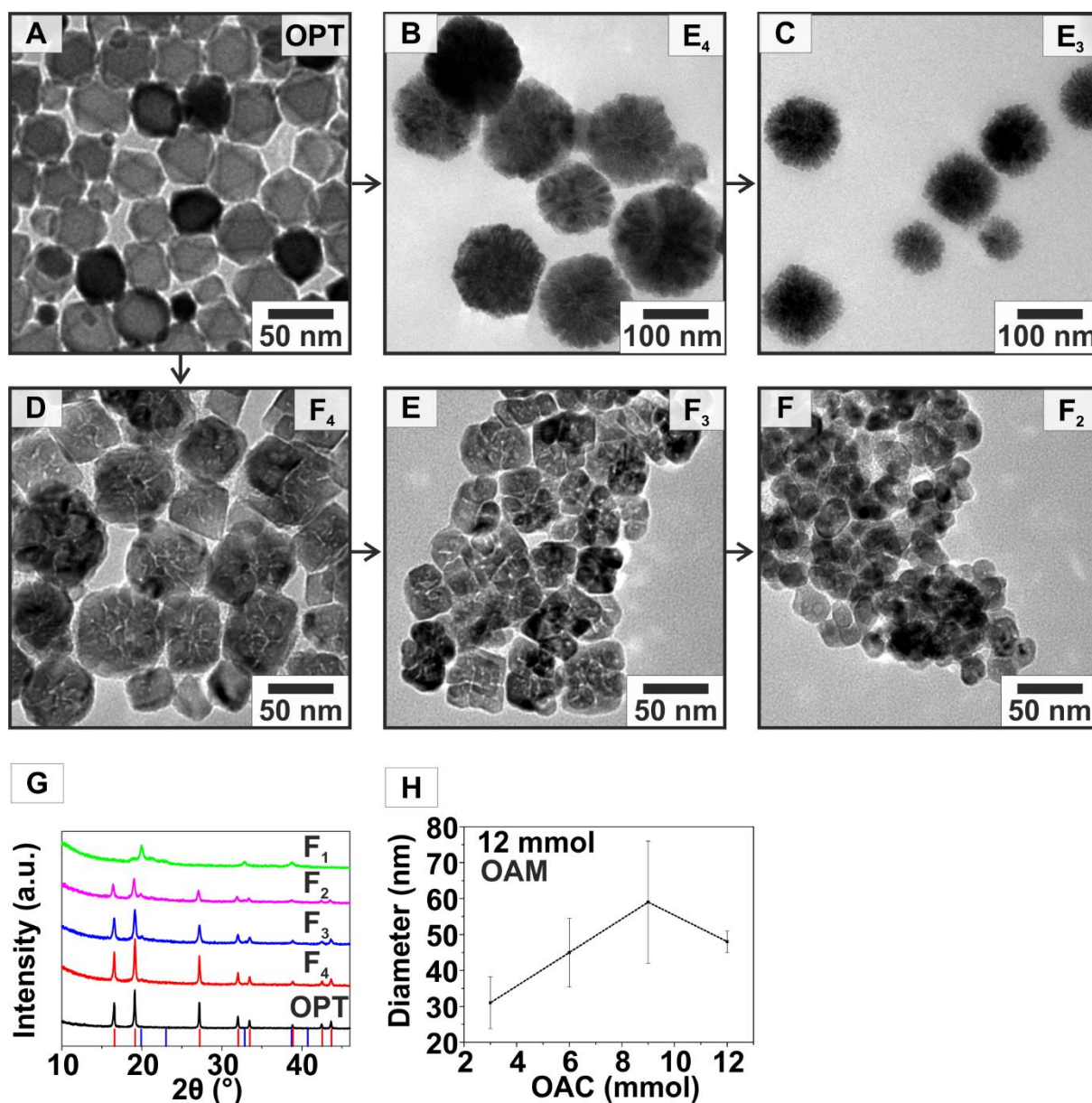
Figure 3.3. TEM images of series E (variable OAM, constant OAC concentration) and F (variable OAC, constant OAM concentration). (A) Concentration of OAC:OAM 12:12 (optimum ratio). Series E: (B) OAC:OAM 12:9, (C) 12:6. Series F: (D) 9:12, (E) 6:12, (F) 3:12. (G) XRD patterns of series F with CoO (red ticks) and Co (blue ticks) as references. (H) Size evolution of series F.

A viscous purple mass was obtained instead, indicating the formation of an intermediate during the synthesis. This observation was similar as for series B, where a longer reaction time was necessary for thermal decomposition with high OAC concentrations. Series E supports the importance of the OAC/OAM acid−base equilibrium for the formation of particles with octahedral morphology. Thermal decomposition is impeded for low amounts of OAM because fewer nuclei and therefore larger nanoparticles are formed. The TEM images (sample E_4 and E_3, Figure 3.3B−C) revealed meso-crystalline structures (consisting of smaller subcrystals) for particles of series E. Thus, the particle morphology can be tuned via the OAC/OAM ratio.

Variable Amount of OAC with Constant OAM Concentration. The effect of OAM as the reductant and base was analyzed in series F with a constant amount of OAM. Here, 1 mmol of $Co(OAc)_2$ was dissolved in 10 mL of ODE, and the reaction time and temperature were set again at 60 min and 330 °C. The amount of OAM was kept constant at 12 mmol, while the amount of OAC was varied from 0 to 12 mmol in steps of 3 mmol. At an amount of 9 mmol OAC, we obtained reasonably well-developed octahedral nanoparticles with diameters of 59 ± 17 nm (Figure 3.3D, F_4), although the polydispersity (PDI = 29%) was still high compared to the optimized synthesis with 12 mmol OAC and OAM (PDI = 6%). We observed, like in series D, the formation of elemental Co at ratios of <1 (Figure 3.3G). For 6 mmol of OAC, the TEM image shows nanoparticles with slightly irregular, but already emerging octahedral morphology with an average diameter of 45 ± 10 nm (Figure 3.3E, F_3, PDI = 21%). At a concentration of 3 mmol of OAC, particles with an average diameter of 31 ± 7 nm (PDI = 23%) and ill-defined morphology were obtained (Figure 3.3F, F_2). In the absence of OAC (0 mmol, F_1), a macrostructured product with ill-defined morphology was obtained consisting of elemental Co only (Figure 3.3G, F_1). Nanoparticles with octahedral morphology and low PDI value were obtained only for equal amounts of OAC and OAM particles with octahedral morphologies but significantly higher PDI value and elemental Co impurities were formed for higher OAM concentrations (compared to OAC). Still higher OAM concentrations led to increased nucleation and smaller particles. The particle diameters increased with increasing OAC concentration (Figure 3.3H), equal concentrations of OAC and OAM being the only exception. In the optimized synthesis, the PDI dropped significantly, and only CoO with homogeneous particle size and morphology was formed. In summary, large OAM concentrations led to the preferred formation of elemental Co by reduction. Increasing the amount of OAC decreased the reducing properties of the OAC/OAM mixture and therefore led to the nucleation of CoO. The acid−base equilibrium $OAC + OAM = OAC^- + OAMH^+$ leads at the optimum OAC/OAM ratio of 1:1 to the controlled formation of oleate ligands that can bind to the CoO particle surfaces. It is known that the absence of free protons (originating from OAC) by protonation of OAM prevents the desorption of oleate ligands from the CoO particle surface. This inhibition of desorption slows down the kinetics of particle growth and leads to the formation of smaller particles with a narrow size distribution.[46,47] Furthermore, it prevents the reduction of the cobalt precursor to Co.

Characterization of CoO Nanooctahedra. For the final product, we focused on two samples: (i) the optimized synthesis (OPT) and (ii) sample F_4 (using 9 mmol of OAC and 12 mmol of OAM). Caused by the low yield of sample E_4 (12 mmol OAC and 9 mmol OAM), no further

analytics rather than HRTEM were possible. The BET surface areas are 14.62 m2 /g (48 ± 3 nm) for sample OPT and 11.85 m2 /g (59 ± 17 nm) for sample F$_4$. HRTEM images in Figure 3.4 reveal their high crystallinity. The associated fast Fourier transforms (FFTs, shown as insets) show a single set of reflections for each sample, confirming that the nanoparticles are single crystalline or contain several domains sharing identical facets. From the FFTs we obtained for all three samples a d value of 2.46 Å for the lattice plane distance, corresponding to the (111) plane (d = 2.4659) of CoO. The HRTEM images of sample F$_4$ and OPT (Figure 3.4A−B) show well-defined lattices fringes, with an interplanar distance of 2.46 Å corresponding as well to the (111) planes
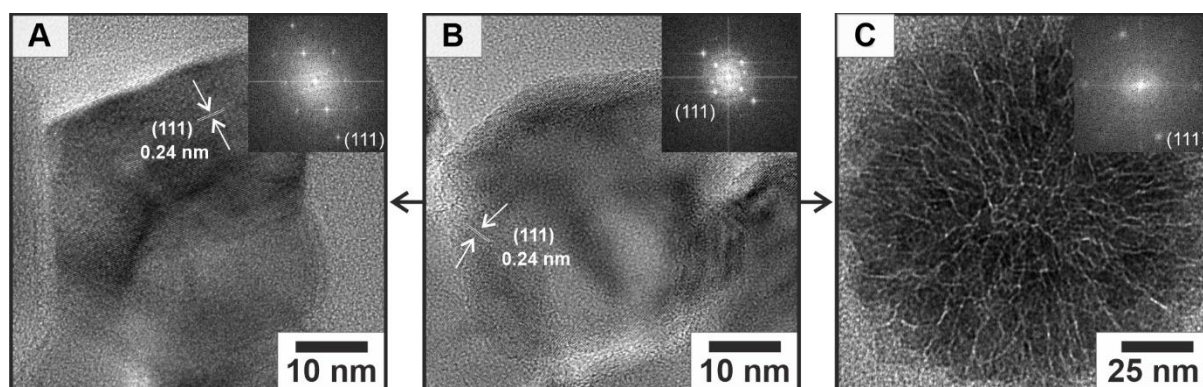

Figure 3.4. HRTEM images of selected samples (FFT as insets). (A) Sample F$_4$ (9 mmol OAC and 12 mmol OAM), (B) OPT (12 mmol OAC and 12 mmol OAM), and (C) sample E$_4$ (12 mmol OAC and 9 mmol OAM).
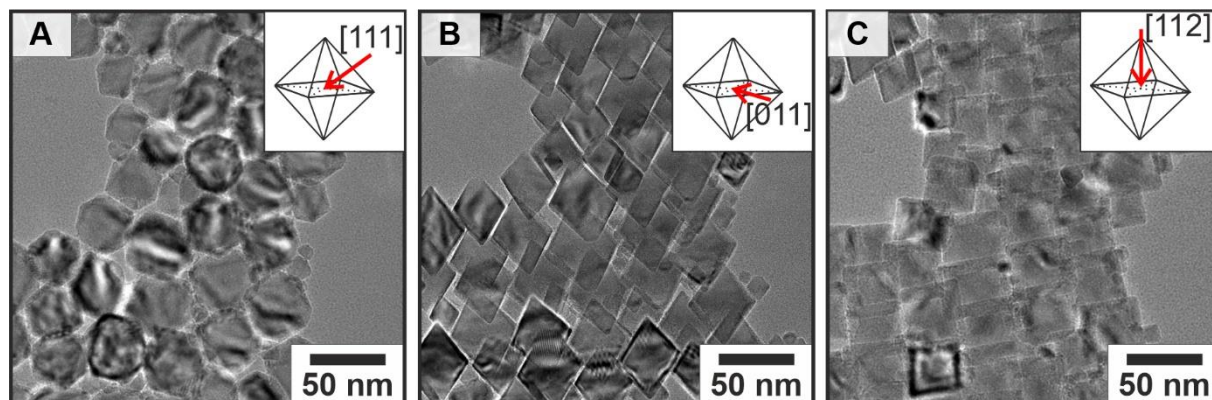

Figure 3.5. HRTEM tilt series for CoO nanooctahedra resulting from an optimized synthesis. Projections are shown in the insets. (A) Projection along [111] (0°), (B) projection along [011] (-40°), (C) projection along [112] (+ 40°).

The octahedral morphology of the particles is related to the minimization of the (100), (010), and (001) surfaces. Nanoparticles of the optimized synthesis expose the (111) surface (Figure 3.5A) containing only either Co^{2+} or O$^{2−}$ ions. Tilt series were performed to exclude the possibility of overlapping triangular nanoplates rather than octahedral nanoparticles. The

38

images show the octahedral particles from different perspectives (Figure 3.5). Most of them show a hexagonal structure (for a tilt angle of 0°) corresponding to the [111] zone axis (Figure 3.5A). After the TEM grid is tilted, the particles appear as rhombohedra (Figure 3.5B) or rectangles (Figure 3.5C) corresponding to the [011] and [122] zone axis. No triangles were observed, which confirms the octahedral morphology of the CoO particles. Furthermore, no Co_3O_4 shell was observed, as reported in previous work.[37] The corresponding SAED through the [111] zone axis is shown in Figure 3.17 (SI), confirming that pure, single-phase, and perfectly octahedral CoO particles were formed. Their (111) surfaces are stabilized by the oleate capping ligands that prevent surface oxidation. The full tilt series is shown in Figure 3.18 (SI). Based on an ideal octahedron with eight {111} facets, the HRTEM images for sample F4 and OPT confirm that the nanoparticles are enclosed by {111} facets.

The octahedral morphology appears to be related to the oleate capping ligands. The IR spectra in Figure 3.6A show the presence of the surfactant on the particle surface for sample F_4 (Figure 3.6A, red ticks) and the product of the optimized synthesis (OPT, Figure 3.6A, black ticks). The spectra of both samples show vibrational bands at identical wavenumbers. The band at 3675 cm^{-1} belongs to the stretch of the free hydroxyl groups on the (111) surface of CoO.[63] The bands at 2924 and 2854 cm^{-1} are characteristic for the asymmetric and symmetric stretches of the OAC methylene groups.[61] OAC and OAM are involved in an acid−base equilibrium. Therefore, we observe the asymmetric and symmetric vibrations at 1553 and 1415 cm^{-1} caused by the OAC carboxylate group.[62] The band at 1017 cm^{-1} is associated with the C−O vibration of the carboxylate group, and the band at 669 cm^{-1} is associated with the Co−O stretch.[60] The absence of the C=O stretch at ~1700 cm^{-1} indicates a chemisorption of OAC as an anionic carboxylate ligand onto the particle surface. No characteristic band of an amine ligand appears that might be compatible with surface-bound OAM. This supports our assumption that OAC is the preferred surfactant that controls the growth of the (111) facets, while OAM is responsible only for the deprotonation of OAC and for the nucleophilic attack on the cobalt intermediate.
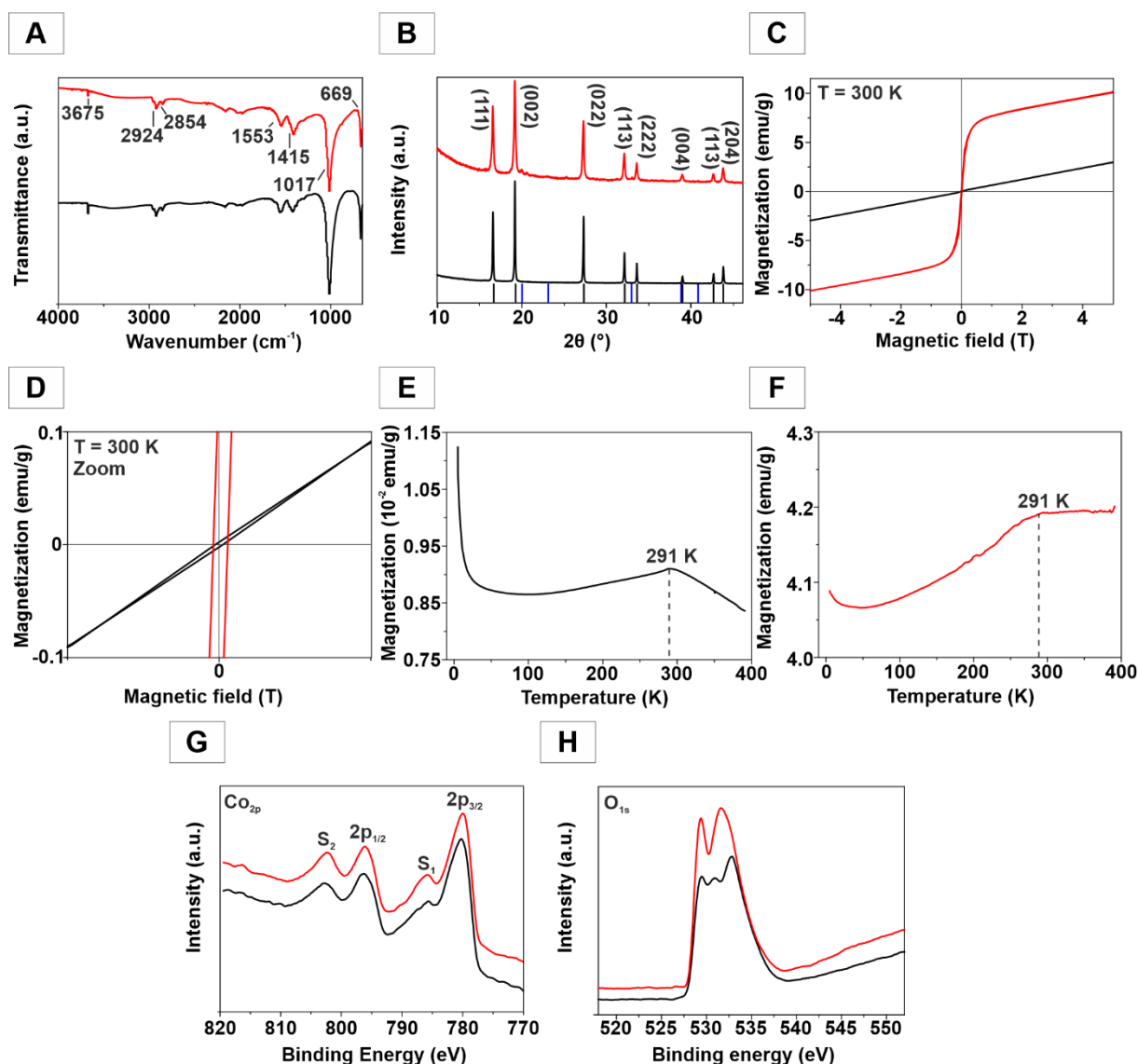
Figure 3.6. Analysis of sample F_4 (9 mmol OAC and 12 mmol OAM, red ticks) and the product of the optimized synthesis OPT (black ticks). (A) FTIR spectra, (B) powder X-ray diffractograms with CoO (black ticks) and Co (blue ticks) as references. (C) Magnetization as a function of the applied field at 300 K; (D) magnified image of (C); (E) magnetization as a function of the temperature for the optimized synthesis and (F) for the sample F_4. (G) Co2p XPS spectra and (H) O1s spectra.

The X-ray powder diffractograms (Figure 3.6B) show that phase-pure CoO (without Co contamination) was formed in bulk amounts under optimized conditions (OPT), while sample F_4 shows small impurities of elemental Co. Bulk CoO and Co_3O_4 show antiferromagnetic ordering with Neel´ temperatures of $T_N = 291$ K (CoO) and $T_N = 40$ K (Co_3O_4). Figure 3.6C shows the magnetization as a function of the applied field at 300 K. A magnified image for Figure 3.6C is given in Figure 3.6D. The M(H) curves show a ferromagnetic response indicating the presence of different magnetic phases. Nanoparticles are known to have a magnetic behavior different from the bulk materials because surface magnetism becomes important for high surface-to-volume ratios. The ferromagnetic response is caused by uncompensated magnetic moments on the particle surfaces.[64] This is supported by the data for sample F_4, which shows

40

a much stronger magnetic response than the product of the optimized synthesis (OPT). The average diameter for sample F_4 is 59 ± 17 nm (PDI = 29%), while the particle diameter is 48 ± 3 nm for sample OPT (PDI = 6%). Taking into account the PDI, a higher fraction of nanoparticles with small diameters leads to a higher signal (larger hysteresis) for sample F_4 than for monodisperse CoO nanooctahedra obtained from the optimized synthesis. This is supported by the magnetization data as a function of temperature. A maximum at 291 K appears for the monodisperse nanooctahedra (Figure 3.6E), whereas sample F_4 shows no pronounced maximum of the susceptibility (Figure 3.6F). This is compatible with the higher polydispersity of the particles which leads to a significantly broader maximum. Neither CoO nanooctahedra obtained from the optimized synthesis nor sample F_4 shows a maximum at 40 K indicating an antiferromagnetic ordering of Co_3O_4. This shows that no surface oxidation occurs because both products contain only CoO and no Co_3O_4. The peak positions of the XPS spectra (Figure 3.6G) for both samples are at 780 eV (for 2p3/2) and at 796 eV (for 2p1/2). CoO and Co_3O_4 are known to have significant differences in their XPS spectra. CoO shows intense shakeup satellite structures, while the satellites for Co_3O_4 are very weak or even missing. The Co 2p3/2 spin−orbital component has a satellite located at about S1 = 786 eV, while the Co 2p1/2 satellite is located at S2 = 803 eV (Figure 3.6G). Both satellites show intense signals, indicating the presence of Co^{2+}, while there are no signals indicating the presence of Co^{3+} species. The O1s signals at higher binding energies allow to differentiate clearly between both samples (Figure 3.6H). The broadened O1s signal for sample F_4 appears at 531.6 eV (with a shoulder); for the nanooctahedra from the optimized synthesis a distinct split signal is centered at 530.9 eV and 532.8 eV, and the signals at lower binding energies are located at the same position (529.4 eV). An explanation for the differences of the O1s signals could be the higher polydispersity of sample F_4. While latter signal (lower binding energy) is associated with the Co−O bonds, the signal at higher binding energies is associated with hydroxyl groups on the particle surface and may be affected more strongly by the polydispersity.[65] In summary, there is no indication of Co^{3+}, which could indicate the presence of a Co_3O_4 surface shell on the CoO particles.

Binding Energy vs OAC/OAM Ratio. Simulation experiments were done to determine the dependence of the binding energy in relation to the OAC/OAM ratio. Based on the Monte Carlo calculations (Figure 3.19 (SI)), the nanoparticles with the lowest spread in the adsorption values and the highest adsorption energy were chosen, so that the rest of the simulation experiments could be carried out on only 2 representative particles instead of all 50 different diameters. Therefore, additional simulations were carried out with nanoparticles having sizes of 2.7 and 3.2 nm. The simulations are based on the different series described above. We considered 12

molecules of OAC in the solution, and the number of OAM molecules was increased in steps of 3 molecules from 0 to 12 OAM molecules. The same procedure was done vice versa by fixing the number of molecules for OAM at 12 and increasing the number of molecules for OAC. Furthermore, the same simulations were done with a fixed number of 24 molecules of OAC or OAM. It was also taken into account that the hydrogen from the deprotonated OAC can protonate OAM. In all the simulated scenarios, the systems with an OAC/ OAM ratio of 1 gave the highest negative binding energy (Figure 3.7A–B). This implies that this ratio will give the most stable configurations. This is in agreement with the experimental observation that the ideal ratio of OAC/OAM of 1 allows the formation of small, stable nanoparticles with an octahedral morphology and with a narrow size distribution. By increasing the total number of molecules in the solution from 24 (12 fixed) to 48 (24 fixed) at the ideal ratio of 1, the smaller nanoparticles (i.e., the 2.7 nm representative of the smaller nanoparticles in the simulation experiments) have a slightly higher negative binding energy compared to the representative larger nanoparticles (i.e., with a diameter of 3.2 nm). Thus, an increase in the number of molecules in the solution leads to the formation of smaller nanoparticles at this ideal ratio. This is confirmed by the experimental observation (Figure 3.1E) that an increase in the concentration of each surfactant leads to a decrease of both the nanoparticle diameter and the PDI (series A). Another important observation is that the negative binding energy increases as the OAC/OAM ratio increases. This predicts that the smaller nanoparticles will be more stable for ratios with excess OAC compared to nanoparticles with excess OAM. By using an excess of OAC (series E), we obtained meso-crystalline structures (consisting of smaller subcrystals, Figure 3.3B–C).
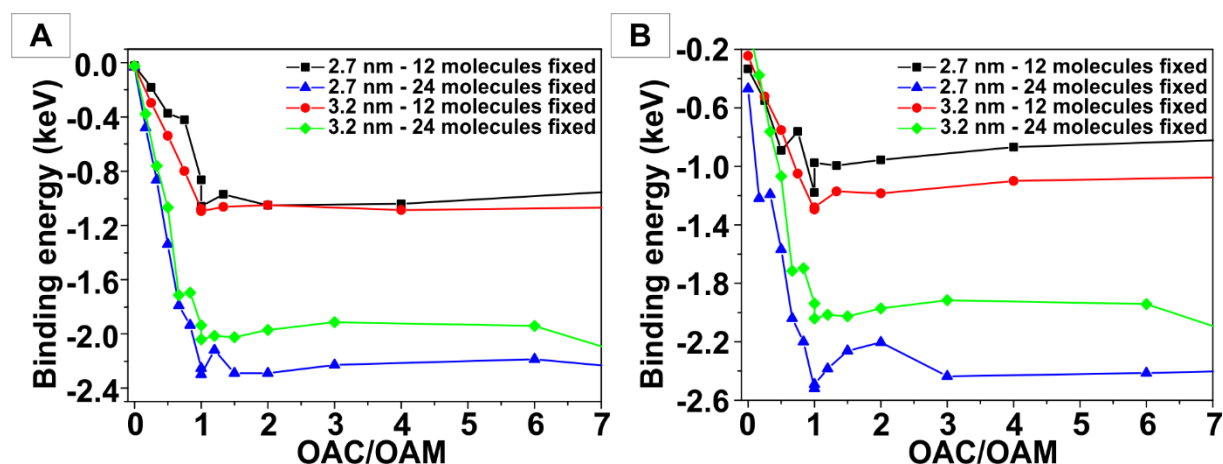

Figure 3.7. Summary of the simulation experiments in a plot of binding energy versus OAC/OAM ratio for nanoparticles with a size of 2.7 and 3.2 nm. The number of OAC molecules was fixed at 12 or 24 molecules. OAM were increased stepwise from 0 to 12 or 24 molecules, and the same procedure was done vice versa. (A) The hydrogen from the deprotonated OAC protonates OAM; (B) OAM is not protonated.

In the absence of OAM, when only OAC is present in solution, the binding energy is less than the ideal ratio of 1, implying that the simulated system becomes more and more unstable. The reason is that the protons (from the deprotonated OAC that adsorbed onto the nanoparticle surfaces) create electrostatic pressure and, at some point, some OAC desorbs from the nanoparticle to balance this effect.[61] This, in turn, leads to a less stable nanoparticle surface. As a result, particle growth is not inhibited, which leads to uncontrolled particle growth. Considering series B, the reaction time depends on the concentration of the surfactants. High surfactant concentrations lead to longer reaction times. Furthermore, we could show that OAM facilitates the thermal decomposition of the cobalt intermediate. Therefore, no uncontrolled nanoparticles growth was observed within a reaction time of 60 min in the absence of OAM. In the absence of OAC, the negative binding energy for all the simulated systems was comparatively low. Thus, the CoO nanoparticles would not be stable in this configuration without OAC. This agrees with the experimental results that only elemental Co forms in the absence of OAC (Figure 3.3G, F_1). In summary, the following mechanism can be proposed based on the simulations and the experimental results. OAC is the preferred surfactant that controls the growth and stabilizes the CoO nanoparticles, while OAM is responsible for the deprotonation of OAC and the nucleophilic attack on the Co intermediate. The systems where OAM is not protonated by oleic acid (Figure 3.7B) seem to be slightly more stable than the counterpart where OAM is protonated by OAC (Figure 3.7A). We assume that, after OAM has deprotonated OAC, the weak van der Waals bond between the nitrogen and hydrogen atoms (to form NH_3^+ functional groups) can easily be broken by the CoO surface to form surface hydroxyl groups (as observed experimentally by the FTIR data). Therefore, the OAM molecules return to their original state (with NH2 groups) where they are available for the deprotonation of OAC by nucleophilic attack. Figure 3.20 (SI) shows a representative energy and geometry-optimized configuration image for all simulated systems, considering OAC as the surfactant, while OAM is only responsible for the deprotonation of OAC as well as for the nucleophilic attack on the precursor.

CoO Nanooctahedra as Catalysts for the Oxygen Evolution Reaction (OER). The electrochemical performance of the as-fabricated electrodes with samples OPT and F_4 is provided in Figure 3.8. The electrodes were baked at 350 °C prior to the measurements to improve mechanical stability.
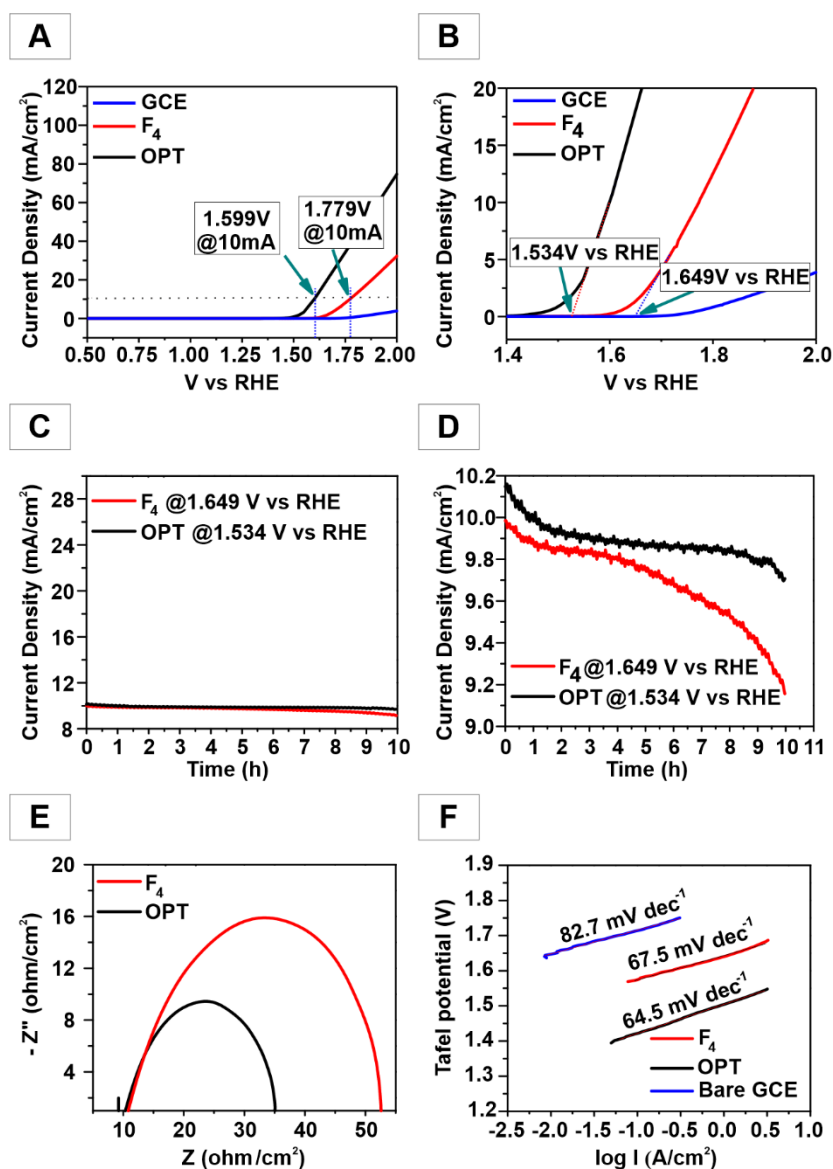
Figure 3.8. Morphology-dependent electrochemical water oxidation performance of CoO: (A, B) normal and magnified LSV plots, (C, D) normal and magnified electrostability curves, (E) EIS Nyquist, and (F) Tafel plots.

The LSV curves in Figure 3.8A and B show that the onset water oxidation potential for the electrodes prepared from sample OPT is shifted to a lower V_{onset} value of 1.53 V compared to sample F4 (V_{onset} = 1.65 V). Factors other than the particle size may affect the shift of the onset potential (e.g., different catalytic centers). These may be surface sites, defects, etc. that lower the activation energy and therefore the catalytic activity. These sites may be present on the surfaces of the CoO OPT samples due to the preparation, and they are nontrivial to detect. The current density was up to 10 mAcm^{-2} at 1.60 and 1.78 V for the electrode from particles of sample OPT and F$_4$, respectively. A long-term stability test was carried at 10 mA cm^{-2} standard current at 1.60 V for sample OPT and at 1.78 V for samples OPT and F$_4$, respectively (Figure 3.8C and D). In both cases, the initial current density drop was followed by a persistent

stability period, where the current density showed little polarization. However, the electrode from sample F_4 showed a significant current decay from 9.8 mA cm^{-2} (after 4 h) to 9.1 mA cm^{-2} (after 10 h), i.e., a 9% decay of the initial current. In contrast, the electrode surface of the OPT particles surface showed a much higher resilience to electric decay. It sustained its electric stability up to 9 h, followed by a slight decay to 9.7 mA cm^{-2} , approximately a 3% loss of the initial current density. The better current sustaining stability of the electrode from OPT particles could be attributed to the metal surface sites of the CoO particles with octahedral morphology, which led to a swift electron transfer and hence supported the surface reaction kinetics of adsorbed species (i.e., water molecules). In addition, we have measured the size histogram and surface area using BET for both OPT and F_4 samples. The histogram shows that the optimized sample (OPT) has particle diameters of 48 ± 3 nm (PDI = 6%) and sample F_4 has particle diameters of 59 ± 17 nm (PDI = 29%). Sample OPT had a BET surface area of 14.62 m^2 /g, and sample F_4 a BET surface area of 11.85 m^2 /g. These parameters also favor the enhanced electrochemical activity of sample OPT. It should be mentioned that most of the surfactant molecules are decomposed during the sintering of the electrodes (as demonstrated by FT-IR spectroscopy (Figure 3.20C (SI)). There is no contribution of surfactant molecules to the generated current. These results show that the particle morphology with Co^{2+} sites exposed on the (111) surfaces plays a significant role in the charge transfer mechanism, as the optimized (OPT) particles maintained almost all (∼97%) of the initial current compared to 91% (for sample F_4). Moreover, the long-term stability test with no countable increase in the overpotential is strong evidence of the viable OER process assisted by the modified electrode. The stability with respect to the phase and the morphology of the nanoparticles after the electrochemical treatment was monitored by X-ray diffraction. The X-ray diffractogram (Figure 3.20D (SI)) of the electrodes after preparation, sintering, and electrochemical measurments clearly confirm that the phase of the CoO nanomaterials is conserved. The morphology of the nanoparticles at elevated temperature was confirmed by TEM after annealing the nanoparticles at 350 °C (Figure 3.20A−B (SI)). The electrode kinetics were assessed from the charge transfer resistance with electrochemical impedance spectroscopy (EIS). The semicircles of the comparative Nyquist plots in Figure 3.8E at low frequency (high Z) increase in order, i.e., bare GCE > F_4 > OPT, indicating a facilitated charge flow for the OPT particles. The EIS plots indicate a decreasing charge/ mass transfer resistance in the order GCE > F_4 > OPT. This behavior validates the fast transfer of electrons between the electrolyte−electrode interface as a function of particle diameter, morphology, and surface structure. Similarly, structural defects have been reported to promote electronic conduction in

CoO particles with hexagonal star morphology, thereby leading to improved electrocatalytic water oxidation at lower overpotentials.[34]

Tafel plots were obtained by LSV analysis recorded at 2 mV s^{-1}. The results for bare GCE, F$_4$, and OPT electrodes are provided in Figure 3.8F. The electrode from the OPT nanoparticles has a small Tafel slope of 64.5 mV dec^{-1} compared to 67.5 mV dec^{-1} for F$_4$ nanoparticles. The Tafel slope for the electrode prepared with OPT particles is compatible with a kinetically faster OER process and mass transfer between the electrode interface and electrolyte, which is more beneficial for electrochemical applications.[66] The smallest value of the Tafel slope for the electrode prepared with OPT particles suggests an adsorption of the active species on the electrode surface. This is compatible with a single electron transfer mechanism, the most established pathway reported for cobalt-based OER catalysts[34,66,67] according to Shinagawa et al.,[68] who provided theoretical insight into how Tafel plot values may be assigned to a specific mechanism. A Tafel slope of 120 mV dec^{-1} is characteristic for processes where the surface species formed in the step just before the rate-determining step is predominant. Tafel slopes >120 mV dec^{-1} are characteristic when surface-adsorbed species produced in the early stage of the OER are dominant.[65] The electrochemical performance of the electrodes prepared from the CoO nanomaterials synthesized in this work is compared with the performance of materials reported before [20,30,56,57,69,71−76] with regard to their onset potential (V vs RHE) measured at 10 mA cm^{-2} in Table 3.2 (SI).

3.4. Conclusion

We demonstrated that control of CoO nanoparticle size and morphology was achieved for the thermal decomposition of Co(OAc)$_2$ by changing (i) the surfactant ratio of OAC/OAM and (ii) the reaction time. We could show that a ratio of OAC/OAM > 1 ceased the formation of nanoparticles, while decreasing the ratio lead to the formation of meso-crystalline CoO. When the ratio was <1, elemental Co was formed as a side product beside CoO. The optimized ratio (1:1) led to the formation of well-defined CoO nanooctahedra. There are two competing mechanisms influencing the nucleation and growth of the nanoparticles: (i) concentration-dependent monomer diffusion and (ii) monomer stabilization by excess surfactant. While the former controls the size for changing the amount of solvent, both mechanisms control the particle size when the precursor concentration is changed by way of the surfactants/ precursor ratio. The resulting nanoparticles were superparamagnetic at room temperature and ferro-ferrimagnetic at low temperature. Different simulation experiments support the experimental

observations with the theoretical data, allowing to put the experimental results on a secure basis and to suggest a molecular mechanism for the reaction processes. Most importantly, the CoO nanooctahedra showed a high performance toward catalyzing OER in alkaline medium, manifesting a small OER onset potential, large anodic current, and long-term durability. With an onset potential of 1.61 V vs RHE,[69] they compared favorably with previously reported Co-based OER electrocatalysts,[70–72] and they were superior to "conventional" spherical CoO particles or CoO nanoparticles with multioctahedral morphology.

3.5. Experimental Section

Materials. Cobalt acetate, $Co(OAc)_2 \cdot 4\,H_2O$ (98% ABCR), oleylamine (OAM) (>50 % Tokyo Chemical Industry), oleic acid (OAC) (90% Sigma Aldrich), 1-octadecene (ODE) (90% Sigma Aldrich), cyclohexane (99% Fisher Chemical), ethanol (98% Honeywell).

Optimized synthesis. 1 mmol of solid $Co(OAc)_2 \cdot 4\,H_2O$ (249 mg) was given into a 100 mL three-necked flask, and 10 mL of ODEand 12 mmol (4 mL) of OAM and OAC were added. The solution was heated to 65°C under stirring (600 rpm) and kept at that temperature during degassing (10^{-2} mbar). Subsequently, the flask was flushed with argon, and the process was repeated twice. The resulting solution was heated to 330°C (3°C/min) for 60 minutes under stirring (600 rpm). Subsequently, the reaction solution was cooled to room temperature. For purification, the product was washed three times with ethanol and cyclohexane and dried *in vacuo* at room temperature. The variations within the series A-F were done following to the same procedure as above while changing the parameters given in **Table S1**.

X-ray powder diffraction (XRPD). X-ray diffraction patterns were recorded on a STOE Stadi P diffractometer equipped with a Dectris Mython 1k detector in transmission mode using Mo Kα_1 radiation. Crystalline phases were identified according to the PDF–2 database using Bruker AXS EVA 10.0 software.

IR Spectroscopy. ATR-IR spectra were measured on a Nicolet iS10 Spectrometer manufactured by Thermo Scientific. The spectra were recorded in a frequency range from 650 cm^{-1} to 4000 cm^{-1} with a resolution of 1.4 cm^{-1} per data point.

Transmission electron microscopy (TEM). Transmission electron microscopy (TEM) mages for determining the size and morphology were acquired on a FEI Tecnai G2 Spirit microscope operating at 120 kV (LaB$_6$ filament), equipped with a Gatan US1000 CCD-camera (16-bit, 2048 × 2048 pixels), using the Gatan Digital Micrograph software. Samples for TEM were

prepared by placing one drop (10 µL) of a diluted nanoparticle solution in cyclohexane (0.1 mg mL^{-1}) on a carbon-coated copper grid and by letting it dry at room temperature. Size evaluation of individual nanoparticles on the TEM images was performed with ImageJ.

High Resolution Transmission electron microscopy (HRTEM). The samples were prepared by adding a drop of CoO in cylcohexan on a carbon coated copper grid. The samples were measured with the FEI Tecnai F30 ST TEM at 300 kV acceleration voltage equipped with a Gatan US4000 4k CCD camera.

Superconducting quantum interference device (Squid). The magnetization as function of the applied field or the temperature were carried out with a QuantumDesign MPMS-XL-5 SQUID (superconducting quantum interference device) magnetometer.

X-ray photoelectron spectroscopy (XPS). X-ray photoelectron spectroscopy (XPS) measurements were performed on a Kratos AXIS Ultra DLD instrument using a monochromatic Al Ka x-ray source.

Simulation methodology. Nanoparticles with different diameters ranging from 1.0 nm to 6.0 nm in steps of 0.1 nm where simulated and 1 OAC molecule was adsorbed onto the nanoparticle surface. This was done to select the nanoparticle diameters with the highest adsorption energy, so that the rest of the simulation experiments could be carried out on only 2 representative particles as set out below instead of on all 50 different diameters. The nanoparticles with diameters of 2.7 and 3.2 nm was selected as these diameters had the highest adsorption energy and a relatively small spread in the adsorption values based on the Monte Carlo calculations. Thereafter, sixteen (16) different simulation experiments were conducted as follows:

(a) The number of OAC molecules adsorbed onto the CoO nanoparticles was fixed at 12 molecules while the number of OAM in the solution was varied from 1 to 12 in steps of 3 molecules. During this experiment the hydrogen from the deprotonated OAC was not allowed to protonate the OAM molecules.

(b) The number of OAC molecules adsorbed onto the CoO nanoparticles was again fixed at 12 molecules with varying number of OAM (1 to 12 in steps of 3), but this time the hydrogen from the deprotonated OAC was allowed to protonate the OAM molecules.

(c) The number of OAM molecules was then fixed at 12 molecules, and the number of OAC was allowed to vary from 1 to 12 in steps of 3 molecules. Similar to before, at first the hydrogen from the deprotonated OAC was not allowed to protonate the OAM molecules.

(d) The number of OAM molecules was again fixed at 12 molecules and the number of OAC was varied from 1 to 12 (step 3 molecules) and the hydrogen from the deprotonated OAC was allowed to protonate the OAM molecules

(e) (a) to (d) was then repeated but this time for 24 molecules fixed in each case for either OAC or OAM respectively and the other molecules was varied with step sizes of 4 molecules.

(f) Thereafter (a) to (d) as well as (e) was repeated but for CoO nanoparticles with a diameter of 3.2 nm.

All these simulation experiments were carried out to determine the binding energy for each scenario and from the binding energy values predict the most likely (most stable) CoO-OAC/OAM system. This was done as follows:

I.   *Adsorption*

Material Studio (*MS7.0*) was used to perform Monte Carlo, simulated annealing schemes, with 10 most likely outcomes. Different ratios of OAC/OAM as described above, were used and the molecules were simultaneously adsorbed onto the nanoparticle surface. Most likely adsorption configurations were identified by doing Monte Carlo searches of the configurational space of the substrate-adsorbate systems as the temperature was slowly decreased. Initially a universal forcefield was used with charges assigned by the *QEq charge equilibration method*. The same experiments as described above were also repeated using the *charge consistent valence forcefield (cvff)* with charges assigned by the forcefield, and similar results were generated. The electrostatics and the Van der Waals interactions summation method were both atom based with an '*ultra-fine*' quality selected, i.e. with 10 cycles and 100,000 steps per cycle.

II.   *Geometry optimization*

Geometry optimization was carried out via molecular mechanics on each of the scenarios as described above. '*Discover*' was employed with a *cvff forcefield* and charges assigned by the forcefiled. An '*atom-based*'-summation method was used with settings applied to both Van der Waals and Coulomb forces. A '*smart minimization*' algorithm was employed. This uses combinations of the steepest descent, conjugate gradient and newton methods. The Fletcher-Reeves algorithm was used for the conjugate gradient method and for the newton method, Broyden-Fletcher-Goldfarb-Shanno (BFGS) algorithms was used.

III.   *Molecular dynamics simulations*

After geometry optimization as described above, molecular mechanics were carried out on all of the simulated systems. A constant temperature, constant volume (NVT) ensemble at room temperature was used with a time step of 1.0 femtosecond and a dynamics time of 20.0

picoseconds. The *Anderson-thermostat* with a collision ratio of 1.0 was used with 20,000 simulation steps. Thereafter, the final molecular dynamics output was again geometry optimized as described above to arrive at the final, geometry- and energy- optimized systems.

IV.   Binding Energy

The binding energy of the OAC/OAM (E_M) onto the nanoparticle surface (E_{NP}) was calculated by subtracting E_M and E_{NP} from the total energy of the system (E_{Total}), since the total system energy is just the energy of each separate system plus the binding energy (E_B), i.e.

$$E_B = E_{Total} - E_{NP} - E_M \qquad (3.1)$$

This was done as follows. After the optimum configurations of the nanoparticle-molecules systems were determined, a single point energy calculation was conducted. Thereafter, the nanoparticle was removed from the system and a single point energy calculation was carried out, from which the energy of the molecules was determined. The energy of the nanoparticle was then determined by removing the molecules and conducting a single point energy calculation.

Electrode preparation. The as-synthesized F_4 and OPT. nanoparticles (5 mg) were added to 1 mL of ethanol/water solution ($V_{ethanol} : V_{water} = 1 : 3$). 30 μL of 5 wt% Nafion solution was added to this solution to enhance the binding affinity of the electrocatalyst with the GCE surface. This was subjected to sonication for one hour to prepare a homogeneous slurry. The GC working electrode was prepared by taking 5 μL of the slurry and drop-casted with a micropipette. The electrodes were allowed to dry overnight at room temperature in a clean chamber and subsequently sintered at 350 °C. To monitor the crystal structure stability after electrochemical measurements, electrodes were prepared under similar experimental condition (as stated above) on conductive FTO glass as GC surfaces could not be used as support for X-ray diffraction.

The electrocatalytic performance of the CoO nanooctahedra was measured with an electrochemical analyzer (CH Instruments, Model CHI660E) in 1.0 M KOH solution at 25 °C. A three-electrode electrochemical cell consisting of (i) a saturated calomel electrode (SCE) as reference electrode, (ii) a Pt gauze-auxiliary electrode, and (iii) a 3 mm (0.07 cm^2) glassy carbon working electrode (GCE) was used to record the electrochemical function and output measurements. Initially, compensation for *iR* drop was recorded for all samples (100%). Full scan linear sweep voltammograms (LSVs) were acquired for the determination of the Tafel plot for all samples (i.e., bare GCE, F_4, and opt) electrodes. The long term stability of the samples as electrocatalyst was monitored by chronoamperometric (*I-t*) analysis. Electronic impedance spectroscopy (EIS) was used to determine the charge transfer behavior at the interface of the

respective electrode. EIS was carried out at 1.55 V (vs. a reversible hydrogen electrode (RHE)).

All electrochemical results were plotted with respect to the RHE by using the Nernst equation

$$E_{(RHE)} = E_{(SCE)} + 0.242 + 0.059 \text{ (pH)} \tag{3.2}$$

For the overpotential (η) equation (1) was modified according to

$$\eta = E_{Ag/AgCl} + (0.197 + 0.059 \times \text{pH}) - 1.23 \tag{3.3}$$

3.6. References

(1)   Genuino, H.; Huang, H.; Njagi, E.; Stafford, L.; Suib, S. L. A Review of Green Synthesis of Nanophase Inorganic Materials for Green Chemistry Applications. In *Handbook of Green Chemistry*, 1st ed.; Perosa, A., Selva, M., Eds.; Wiley-VCH: Weinheim, Germany, 2012; Vol. *8*.

(2)   Li, J.; Güttinger, R.; More, R.; Song, F.; Wan, W.; Patzke, G. R. Frontiers of water oxidation: the quest for true catalysts. *Chem. Soc. Rev.* **2017**, *46*, 6124-6147.

(3)   Jia, J.; Qian, C.; Dong, Y.; Li, Y. F.; Wang, H.; Ghoussoub, M.; Butler, K. T.; Walsh, A.; Ozin, G. A. Heterogeneous catalytic hydrogenation of CO_2 by metal oxides: defect engineering – perfecting imperfection. *Chem. Soc. Rev*. **2017**, *46*, 4631-4644.

(4)   Huang, X.; Zhao, G.; Wang, G.; Irvine, J. T. S. Synthesis and applications of nanoporous perovskite metal oxides. *Chem. Sci.* **2018**, *9*, 3623–3637.

(5)   Liu, L.; Corma, A. Metal Catalysts for Heterogeneous Catalysis: From Single Atoms to Nanoclusters and Nanoparticles. *Chem. Rev*. **2018**, *118*, 4981−5079.

(6)   Vedrine, J. C. Metal Oxides in Heterogeneous Oxidation Catalysis: State of the Art and Challenges for a More Sustainable World. *ChemSusChem*. **2019**, *12*, 577–588.

(7)   Reddy, M. V.; Subba Rao, G. V.; Chowdari, B. V. R. Metal Oxides and Oxysalts as Anode Materials for Li Ion Batteries. *Chem. Rev*. **2013**, *113*, 5364−5457.

(8)   Tahir, M. N.; Oschmann, B.; Buchholz, D.; Dou, X.; Lieberwirth, I.; Panthöfer, M.; Tremel, W.; Zentel, R.; Passerini, S. Extraordinary performance of carbon-coated anatase TiO_2 as sodium-ion anode. *Adv. Energy. Mater*. **2016**, *6*, 1501489.

(9)   Na, H. B.; Song, I. C.; Hyeon, T. Inorganic Nanoparticles for MRI Contrast Agents. *Adv. Mater.* **2009**, *21*, 2133–2148.

(10)   Schladt, T. D.; Schneider, K.; Schild, H.; Tremel, W. Engineered Multifunctional Nanotools for Biological and Cancer Applications. *Dalton Trans.* **2011,** *40*, 6315-6343.

(11) Shin, T.-H.; Choi, Y.; Kim, S.; Cheon, J. Recent advances in magnetic nanoparticle-based multi-modal imaging. *Chem. Soc. Rev*. **2015**, *44*, 4501-4516.

(12) (a) Park, J.; Joo, J.; Kwon, S. G.; Jang, Y.; Hyeon, T. Synthesis of Monodisperse Spherical Nanocrystals. *Angew. Chem.* **2007**, *119*, 4714; (b) *Angew. Chem., Int. Ed.* **2007**, *46*, 4630-4660.

(13) Kim, D.; Shin, K.; Kwon, S. G.; Hyeon, T. Synthesis and Biomedical Applications of Multifunctional Nanoparticles. *Adv. Mater.* **2018**, *30*, 1802309.

(14) *Gas-Phase Synthesis of Nanoparticles*; Huttel, Y., Ed.; Wiley-VCH: Weinheim, Germany, 2017.

(15) Belmonte, T.; Hamdan, A.; Kosior, F.; Noël, C.; Henrion, G. Interaction of discharges with electrode surfaces in dielectric liquids: application to nanoparticle synthesis. *J. Phys. D: Appl. Phys.* **2014**, *47*, 224016.

(16) Zhang, D.; Gökce, B.; Barcikowski, S. Laser Synthesis and Processing of Colloids. Fundamentals and Applications. *Chem. Rev*. **2017**, *117*, 3990−4103.

(17) Poizot, P.; Laruelle, S.; Grugeon, S.; Dupont, L.; Tarascon, J.-M. Nano-sized transition-metal oxides as negative-electrode materials for lithium-ion batteries. *Nature* **2000**, *407*, 496-499.

(18) Smith, R. D. L.; Prévot, M. S.; Fagan, R. D.; Zhang, Z.; Sedach, P. A.; Siu, M. K. J.; Trudel, S.; Berlinguette, C. P. Photochemical Route for Accessing Amorphous Metal Oxide Materials for Water Oxidation Catalysis. *Science* **2013**, *340*, 60-63.

(19) Zhou, Y.; Dong, C.-K.; Han, L.−L.; Yang, J.; Du, X.-W. Top-Down Preparation of Active Cobalt Oxide Catalyst. *ACS Catal.* **2016**, *6*, 6699–6703.

(20) Nishi, T.; Hayasaka, Y.; Suzuki, T. M.; Sato, S.; Isomura, N.; Takahashi, N.; Kosaka, S.; Nakamura, T.; Sato, S.; Morikawa, T. Electrochemical Water Oxidation Catalysed by $CoO-Co_2O_3-Co(OH)_2$ Multiphase-Nanoparticles Prepared by Femtosecond Laser Ablation in Water. *ChemistrySelect* **2018**, *3*, 4979–4984.

(21) Li, Y.-F.; Selloni, A. Pathway of Photocatalytic Oxygen Evolution on Aqueous TiO_2 Anatase and Insights into the Different Activities of Anatase and Rutile. *ACS Catal.* **2016**, *6*, 4769−4774.

(22) Jupille, J.; Thornton, G. Excess Electrons at Oxide Surfaces, In *Defects at Oxide Surfaces*; Springer: Heidelberg, Germany, 2015.

(23) Puigdollers, A. R.; Schlexer, P.; Tosoni, S.; Pacchioni, G. Increasing Oxide Reducibility: The Role of Metal/Oxide Interfaces in the Formation of Oxygen Vacancies. *ACS Catal.* **2017**, *7*, 6493−6513.

(24) Jia, X.; Ma, J.; Xia, F.; Xu, Y.; Gao, J.; Xu, J. Carboxylic acid-modified metal oxide catalyst for selectivity-tunable aerobic ammoxidation. *Nat. Commun.* **2018**, *9*, 933.

(25) Arefi, M.; Saberi, D.; Karimi M.; Heydari, A. Superparamagnetic $Fe(OH)_3$@Fe_3O_4 Nanoparticles: An Efficient and Recoverable Catalyst for Tandem Oxidative Amidation of Alcohols with Amine Hydrochloride Salts. *ACS Comb. Sci.* **2015**, *17*, 341–347.

(26) Kunat, M.; Girol, S. G.; Burghaus, U.; Wöll, C. The Interaction of Water with the Oxygen-Terminated, Polar Surface of ZnO. *J. Phys. Chem. B*, **2003**, *107*, 14350–14356.

(27) *Metal Oxide Catalysis*, Jackson, S. D.; Hargreaves, J. S. Eds.;, Wiley-VCH: Weinheim, Germany 2009.

(28) Skumryev, V.; Stoyanov, S.; Zhang, Y.; Hadjipanayis, G.; Givord, D.; Nogues, J. Beating the superparamagnetic limit with exchange bias. *Nature* **2003**, *423*, 850−853.

(29) Lin, H.-K.; Chiu, H.-C.; Tsai, H.-C.; Chien, S.-H.; Wang, C.-B. Synthesis, characterization and catalytic oxidation of carbon monoxide over cobalt oxide. *Catal. Lett*. **2003**, *88*, 169−174.

(30) Jiang, Z.-J.; Jiang, Z. Interaction Induced High Catalytic Activities of CoO Nanoparticles Grown on Nitrogen-Doped Hollow Graphene Microspheres for Oxygen Reduction and Evolution Reactions. *Sci. Rep.* **2016**, *6*, 27081.

(31) Wang, L.; Zhang, W.; Wang, S.; Gao, Z.; Luo, Z.; Wang, X.; Zeng, R.; Li, A.; Li, H.; Wang, M.; Zheng, X.; Zhu, J.; Zhang, W.; Ma, C.; Si, R.; Zeng, J. Atomic-level insights in optimizing reaction paths for hydroformylation reaction over Rh/CoO single-atom catalyst. *Nat. Commun*. **2016**, *7*, 14036.

(32) Gil-Sepulcre, M.; Gimbert-Suriñach, C.; Aguilà, D.; Velasco, V.; García-Antón, J.; Llobet, A.; Aromí, G.; Bofill, R.; Sala, X. Catalytic H_2 Evolution with CoO, $Co(OH)_2$ and CoO(OH) Nanoparticles Generated from a Molecular Polynuclear Co Complex. *Eur. J. Inorg. Chem.* **2018**, 1499–1505.

(33) Liao, L.; Zhang, Q.; Su, Z.; Zhao, Z.; Wang, Y.; Li, Y.; Lu, X.; Wei, D.; Feng, G.; Yu, Q.; Cai, X.; Zhao, J.; Ren, Z.; Fang, H.; Robles-Hernandez, F.; Baldelli, S.; Bao, J. Efficient solar water-splitting using a nanocrystalline CoO photocatalyst. *Nature Nanotechnol.* **2014**, *9***,** 69–73.

(34) Liang, Z.; Huang, Z.; Yuan, H.; Yang, Z.; Zhang, C.; Xu, Y.; Zhang, W.; Zheng, H.; Cao, R. Quasi-single-crystalline CoO hexagrams with abundant defects for highly efficient electrocatalytic water oxidation. *Chem. Sci.* **2018**, *9*, 6961–6968.

(35) Risbud, A. S.; Snedeker, L. P.; Elcombe, M. M.; Cheetham, A. K.; Seshadri, R. Wurtzite CoO. *Chem. Mater.* **2005**, *17*, 834−838.

(36) Ohno, H. Making Nonmagnetic Semiconductors Ferromagnetic. *Science* **1998**, *281*, 951−956.

(37) Fontannna-Troitinno, N.; Liebana-Vinas, S.; Rodríguez-Gonzalez, B.; Li, Z.-A.; Spasova, M.; Farle, M.; Salgueirino, V. Room-Temperature Ferromagnetism in Antiferromagnetic Cobalt Oxide Nanooctahedra. *Nano Lett.* **2014**, 14, 640−647.

(38) Ye, Y.; Yuan, F.; Li, S. Synthesis of CoO nanoparticles by esterification reaction under solvothermal conditions. *Mater. Lett*. **2006**, *60*, 3175−3178.

(39) Sun, X.; Zhang, Y.-W.; Si, R.; Yan, C.-H. Metal (Mn, Co, and Cu) Oxide Nanocrystals from Simple Formate Precursors. *Small* **2005**, *1*, 1081−1086.

(40) Jaffari, G. H.; Lin, H.-Y.; Ni, C.; Shaha, S. I. Physiochemical phase transformations in Co/CoO nanoparticles prepared by inert gas condensation. *Mater. Sci. Eng.* B. **2009**, *164*, 23−29.

(41) Seo, W. S.; Shim, J. H.; Oh, S. J.; Lee, E. K.; Hur, N. H.; Park, J. T. Phase- and Size-Controlled Synthesis of Hexagonal and Cubic CoO Nanocrystals. *J. Am. Chem. Soc.* **2005**, *127*, 6188-6189.

(42) Schladt, T. D.; Graf, T.; Tremel, W. Synthesis and Characterization of Monodisperse Manganese Oxide Nanoparticles – Evaluation of the Nucleation and Growth Mechanism. *Chem. Mater.* **2009**, *21*, 3183-3190.

(43) Hou, Y. L.; Xu, Z. C.; Sun, S. H. Controlled Synthesis and Chemical Conversions of FeO Nanoparticles. *Angew. Chem., Int. Ed*. **2007**, *46*, 6329−6332.

(44) Zhang, H. T.; Xu, Z. C.; Sun, S. H. Controlled Synthesis and Anomalous Magnetic Properties of Relatively Monodisperse CoO Nanocrystals. *Nanotechnology* **2005**, *16*, 2288-2294.

(45) Kluenker, M.; Tahir, M. N.; Dören, R.; Deuker, M.; Komforth, P.; Plana-Ruiz, S.; Barton, B.; Shylin, S. I.; Ksenofontov, V.; Panthöfer, M.; Wiesmann, N.; Herzberger, J.; Möller, A.; Frey, H.; Brieger, J.; Kolb, U.; Tremel, W. Iron Oxide Superparticles with Enhanced MRI Performance by Solution Phase Epitaxial Growth, *Chem. Mater.* **2018**, *30*, 13, 4277-4288.

(46) Dehsari, H. S.; Ribeiro, A. H.; Ersöz, B.; Tremel, W.; Jakob, G.; Asadi, K. Effect of precursor concentration on size evolution of iron oxide nanoparticles. *CrystEngComm.* **2017***, 19***,** 6694-6702.

(47) Dehsari, H. S.; Heidari, M.; Ribeiro, A. H.; Tremel, W.; Jakob, G.; Donadio, D.; Potestio, R.; Asadi, K. Combined Experimental and Theoretical Investigation of Heating Rate on Growth of Iron Oxide Nanoparticles. *Chem. Mater.* **2017**, *29*, 9648–9656.

(48) Dehsari, H. S.; Harris, R. A.; Ribeiro, A. H.; Tremel, W.; Asadi, K. Optimizing the Binding Energy of the Surfactant to Iron Oxide Yields Truly Monodisperse Nanoparticles. *Langmuir* **2018**, *34*, 6582–6590.

(49) Daniel, P.; Shylin, S. I.; Lu, H.; Tahir, M. N.; Panthöfer, M.; Weidner, T.; Möller, A.; Ksenofontov, V.; Tremel, W. The surface chemistry of iron oxide nanocrystals: Surface reduction of γ-Fe_2O_3 to Fe_3O_4 by redox-active catechole surface ligands. *J. Mater. Chem. C* **2018**, *6*, 326-333.

(50) Tahir, M. N.; Natalio, F.; Cambaz, M. A.; Panthöfer, M.; Branscheid, R.; Kolb, U.; Tremel, W. Controlled synthesis of linear and branched Au@ZnO hybrid nanocrystals and their photocatalytic properties. *Nanoscale* **2013**, *5*, 9944-9949.

(51) Tahir, M. N.; Herzberger, J.; Natalio, F.; Köhler, O.; Branscheid, R.; Mugnaioli, E.; Ksenofontov, V.; Panthöfer, M.; Kolb, U.; Frey, H.; Tremel, W. Hierachical Ni@Fe_2O_3 superparticles through epitaxial growth of γ-Fe_2O_3 nanorods on in situ formed Ni nanoplates. *Nanoscale* **2016**, *8*, 9548-9555.

(52) Chen, Z.; Kronawitter, C. X.; Koel, B. E. Facet-dependent activity and stability of Co_3O_4 nanocrystals towards the oxygen evolution reaction. *Phys. Chem. Chem. Phys*. **2015**, *17*, 29387–29393.

(53) Sidhureddy, B.; Dobdapati, J. S.; Chen, A. Shape-controlled synthesis of Co_3O_4 for enhanced electocatalysis of the oxygen evolution reaction. *Chem. Comm.* **2019**, *55*, 3626-3629.

(54) Liu, X.; Jiang, J.; Ai, L. Non-precious cobalt oxalate microstructures as highly efficient electrocatalysts for oxygen evolution reaction. *J. Mater. Chem. A* **2015**, *3*, 9707-9713.

(55) Lee, Y.; Suntivich, J.; May, K. J.; Perry, E. E.; Shao-Horn, Y. Synthesis and Activities of Rutile IrO_2 and RuO_2 Nanoparticles for Oxygen Evolution in Acid and Alkaline Solutions. *J. Phys. Chem. Lett.* **2012**, *3*, 399−404.

(56) Qi, J.; Zhang, W.; Cao, R. Aligned cobalt-based Co@CoO_x nanostructures for efficient electrocatalytic water oxidation. *Chem. Commun.* **2017**, *53*, 9277-9280.

(57) Liang, Z.; Zhang, C.; Xu, Y.; Zhang, W.; Zheng, H.; Cao, R. Dual Tuning of Ultrathin α-$Co(OH)_2$ Nanosheets by Solvent Engineering and Coordination Competition for Efficient Oxygen Evolution. *ACS Sustainable Chem. Eng*. **2019**, *7*, 3527-3535.

(58) Guo, D.; Chen, F.; Zhang, W.; Cao, R. Phase-transfer synthesis of α-$Co(OH)_2$ and its conversion to CoO for efficient electrocatalytic water oxidation. *Science Bulletin* **2017**, *9*, 626-632.

(59) Locmelis, S.; Binnewies, M. Chemical Transport of MnO/ZnO, FeO/ZnO, and CoO/ZnO Mixed Crystals. *Z. Anorg. Allg. Chem.* **1999**, *625*, 1573.

(60) Tsyganenko, A. A.; Filimonov, V. N. Infrared Spectra of Surface Hydroxyl Groups and Crystalline Structure of Oxides. *Spec. Lett.* **1972**, *5*, 477.

(61) Harris, R.A.; Shumbula, P. M.; v.d. Walt, H. Analysis of the Intercation of Surfactants Oleic Acid and Oleylamine with Iron Oxide Nanoparticles through Molecular Mechanics Modeling. *Langmuir* **2015**, *31*, 3934.

(62) Klokkenburg, M.; Hilhorst, J.; Erne, B. H. Surface analysis of magnetite nanoparticles in cyclohexane solutions of oleic acid and oleylamine. *Vibr. Spec.* **2006**, *43*, 243.

(63) Busca, G.; Guidetti, R.; Lorenzelli, V. Fourier-transform Infrared Study of the Surface Properties of Cobalt Oxides. *J. Chem. Soc. Faraday Trans*. **1990**, *86*, 989.

(64) Ghosh, M.; Sampathkumaran, E. V.; Rao, C. N. R. Synthesis and Magnetic Properties of CoO Nanoparticles. *Chem. Mater.* **2005**, *17*, 2348-2352.

(65) Natile, M. M.; Glisenti, A. Study of Surface Reactivity of Cobalt Oxides Interaction with Methanol. *Chem. Mater.* **2002**, *14*, 3090.

(66) Ranaweera, C. K.; Zhang, C.; Bhoyate, S.; Kahol, P. K.; Ghimire, M.; Mishra, S. R.; Perez, F., Gupta, B. K.; Gupta, R. K. Flower-shaped cobalt oxide nano-structures as an efficient, flexible and stable electrocatalyst for the oxygen evolution reaction. *Mater. Chem. Front*. **2017**, *1*, 1580-1584.

(67) Wang, Y.; Zhou, T.; Jiang, K.; Da, P.; Peng, Z.; Tang, J.; Kong, B.; Cai, W.-B.; Yang, Z.; Zheng, G. Reduced Mesoporous Co$_3$O$_4$ Nanowires as Efficient Water Oxidation Electrocatalysts and Supercapacitor Electrodes. *Adv. Energy Mater*. **2014**, *4*, 1400696.

(68) Shinagawa, T.; Garcia-Esparza, A. T.; Takanabe, K. Insight on Tafel slopes from a microkinetic analysis of aqueous electrocatalysis for energy conversion. *Sci. Rep*. **2015**, *5*, 13801.

(69) Yiliguma, Z.; Wang, W.; Xu, Y.; Wang, X.; Cui, A.M.; Al-Enizi, Y.; Tang, G.; Zheng, G. Bridged-multi-octahedral cobalt oxide nanocrystals with a Co-terminated surface as an oxygen evolution and reduction electrocatalyst, *J. Mater. Chem. A* **2017**, *5,* 7416-7422.

(70) Yu, M.; Waag, F.; Chan, C. K.; Weidenthaler, C.; Barcikowski, S.; Tüysüz, H. Laser Fragmentation-Induced Defect-Rich Cobalt Oxide Nanoparticles for Electrochemical Oxygen Evolution Reaction. *ChemSusChem* **2020**, *13*, 520-528.

(71) Schenk, A. S.; Eiben, S.; Goll, M.; Reith, L.; Kulak, A. N.; Meldrum, F. C.; Jeske, H.; Wege, C.; Ludwigs, S. Virus-directed formation of electrocatalytically active nanoparticle-based Co$_3$O$_4$ tubes. *Nanoscale* **2017**, *9*, 6334-6345.

(72)   Gong, L.; Chng, X. Y. E.; Du, Y.; Xi, S.; Yeo. B. S. Enhanced Catalysis of the
       Electrochemical Oxygen Evolution Reaction by Iron(III) Ions Adsorbed on Amorphous
       Cobalt Oxide, *ACS Catal.* **2018**, *8*, 807−814.

(73)   Zhang, N.; Wang, Y.; Hao, Y.; Ni, Y.; Su, X.; Yin, A.; Hu, C. Ultrathin cobalt oxide
       nanostructures with morphology-dependent electrocatalytic oxygen evolution activity.
       Nanoscale **2018**, *10*, 20313-203220.

(74)   Seo, B.; Sa, Y. J.; Woo, J.; Kwon, K.; Park, J.; Shin, T. J.; Jeong, H. Y.; Joo, S. H. Size-
       Depentend Activity Trends Combined with in Situ X-ray Absorption Spectroscopy
       Reveal Insights into Cobald Oxide/Carbon Nanotube-Catalyzed Bifunctional Oxygen
       Electrocatalysis. *ACS Catal.* **2016**, *6*, 4347-4355.

(75)   Xie, C.; Wang, Y.; Yan, D.; Tao, L.; Wang, S. In situ growth of cobalt@cobalt-borate
       core-shell nanosheets as highly-efficient electrocatalysts for oxygen evolution reaction in
       alkaline/neutral medium. *Nanoscale* **2017**, *9*, 16059-16065.

(76)   Gu, L. F.; Chen, J. J.; Zhou, T.; Lu, X. F.; Li, G. R. Engineering cobalt oxide by interfaces
       and pore architectures for enhanced electrocatalytic performance for overall water
       splitting. *Nanoscale* **2020**, *12*, 11201-11208.

3.7. Supporting Information

Table 3.1. Series chart with the sample labels and the corresponding synthesis parameters.

Series	Label	OAM (mmol)	OAC (mmol)	Reaction time at 330 °C (min)
A	A_1	3	3	60 min
	A_2	6	6	60 min
	A_3	9	9	60 min
	A_4/OPT*	12	12	60 min
B	B_1	3	3	15 min
	B_2	3	3	30 min
	B_3	3	3	45 min
	B_4/A_1	3	3	60 min
C	C_1	12	12	15 min
	C_2	12	12	30 min
	C_3	12	12	45 min
	C_4/OPT*	12	12	60 min
D	D_1	0	24	60 min
	D_2	3	21	60 min
	D_3	6	18	60 min
	D_4	9	15	60 min
	D_5/OPT*	12	12	60 min
	D_6	15	9	60 min
	D_7	18	6	60 min
	D_8	21	3	60 min
	D_9	24	0	60 min
E	E_1	0	12	60 min
	E_2	3	12	60 min
	E_3	6	12	60 min
	E_4	9	12	60 min
F	F_1	12	0	60 min
	F_2	12	3	60 min
	F_3	12	6	60 min
	F_4	12	9	60 min

*Optimized synthesis

Table 3.2. Comparison of CoO electrodes with reference data from the literature.

#	Material composition and synthesis method	Morphology & Phase	Onset Potential (V vs. RHE)	Electrostability @ Current Density	Ref.
1.	Bridged-multi-octahedral cobalt oxide nanocrystals	Octahedral morphology with (111) facet	1.60 V at 10 mA cm^{-2}	13 h at 10 mA cm^{-2}	69
2.	Ultrathin α-Co(OH)2 Nanosheets by solvent engineering	Nanosheets with α-Co(OH)$_2$ form (JCPDS no. 46-0605)	1.50 V at 10 mA cm^{-2}	25 h at 10 mA cm^{-2}	57
3.	Ultrathin cobalt oxide nanostructures by one-step hydrothermal synthesis	Thin nanosheets with the quasi amorphous phase	1.55 V at 50 mA cm^{-2}	24 h at 50 mA cm^{-2}	73
4.	Aligned cobalt-based Co@CoO$_x$ nanostru-ctures by pyrolysis	2D morphlogy	1.52 V at 10 mA cm^{-2}		56
5.	CoOx/CNTs by colloidal synthesis	Spherical NPs, with cubic structure (*JCPDS 9-0402*)	1.59 V at 10 mA cm^{-2}	400 min at 5 mA cm^{-2}	74
6.	CoO Nanoparticles Grown on Nitrogen-Doped Hollow Graphene Microspheres by three step wetchemistry technique	No information given	1.63 V at 10 mA cm^{-2} for CoO	Lost more than 20% activity after 10 hours	30
7.	Co@Co–Bi/Ti by two-step method of electrochemical deposition	3D morphology with metallic cobalt (JPDS no. 05-0727 and 15-0806	1.56 V at 10 mA cm^{-2}	20 000 s at a potential of 1.56 V.	75
8.	Nanoparticle-based Co$_3$O$_4$ tubes	Hierarchical Tubular morphology	1.62 V at 10 mA cm^{-2}	10 min at 10 mA cm^{-2}	71

9.	Macroporous CoO covered by Co/N-doped graphitic carbon nanosheet arrays (mac-CoO@Co/NGC NSAs) prepared by the ultrasonic-assisted wet-chemistry technique	Porous CoOx heterostructures with CoO = JPDF#43-1004 and Co = JPDF#15-0806))	1.62 V	35 h at 10 mA cm^{-2}	76
10.	Cobalt oxide (CoO$_x$) with adsorbed Fe^{3+} ions prepared by electrodeposition	JCPDS 00-003-0913	1.55 V at 10 mA cm^{-2}	20 h at 10 mA cm^{-2}	72
11.	CoO-Co$_2$O$_3$-Co(OH)$_2$ Multiphase-Nanoparticles Prepared by Femtosecond Laser Ablation in Water	Spherical NPs	1.65 V at 1.0 mA cm^{-2}	Significantly lower current density achieved even at 1.7 V *vs.* RHE	20
12.	Selective Synthesis of Monodisperse CoO Nanooctahedra as Cata-lysts for Electrochemical Water oxidation	CoO nanoparticles with octahedron shape	1.59 V at 10 mA cm^{-2}	10 h at 10 mA cm^{-2} Loss only ~3.5 % activity after 10 h	This Work
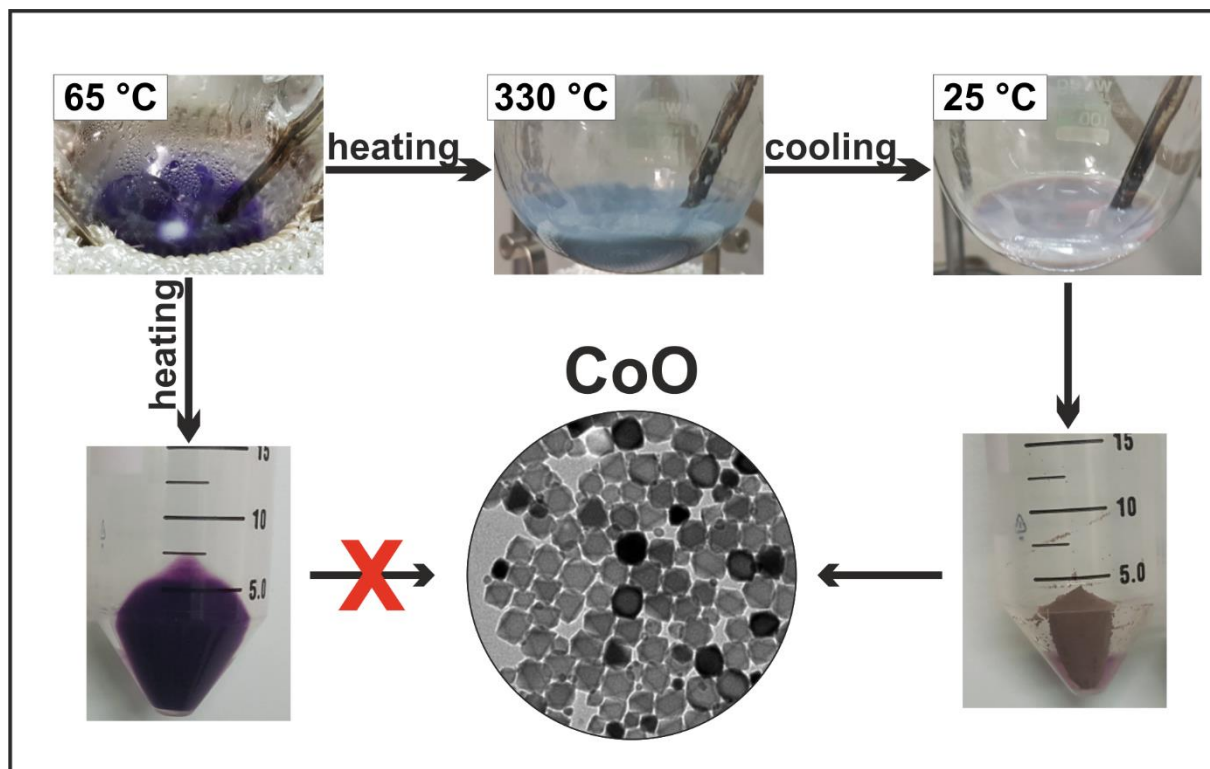
Figure 3.9. Color changes during synthesis. Purple color at 65 °C, blue color at 330 °C, brown color after the synthesis at 25 °C. The brown powder indicates the conversion to CoO, while the purple viscos mass indicates no conversion.
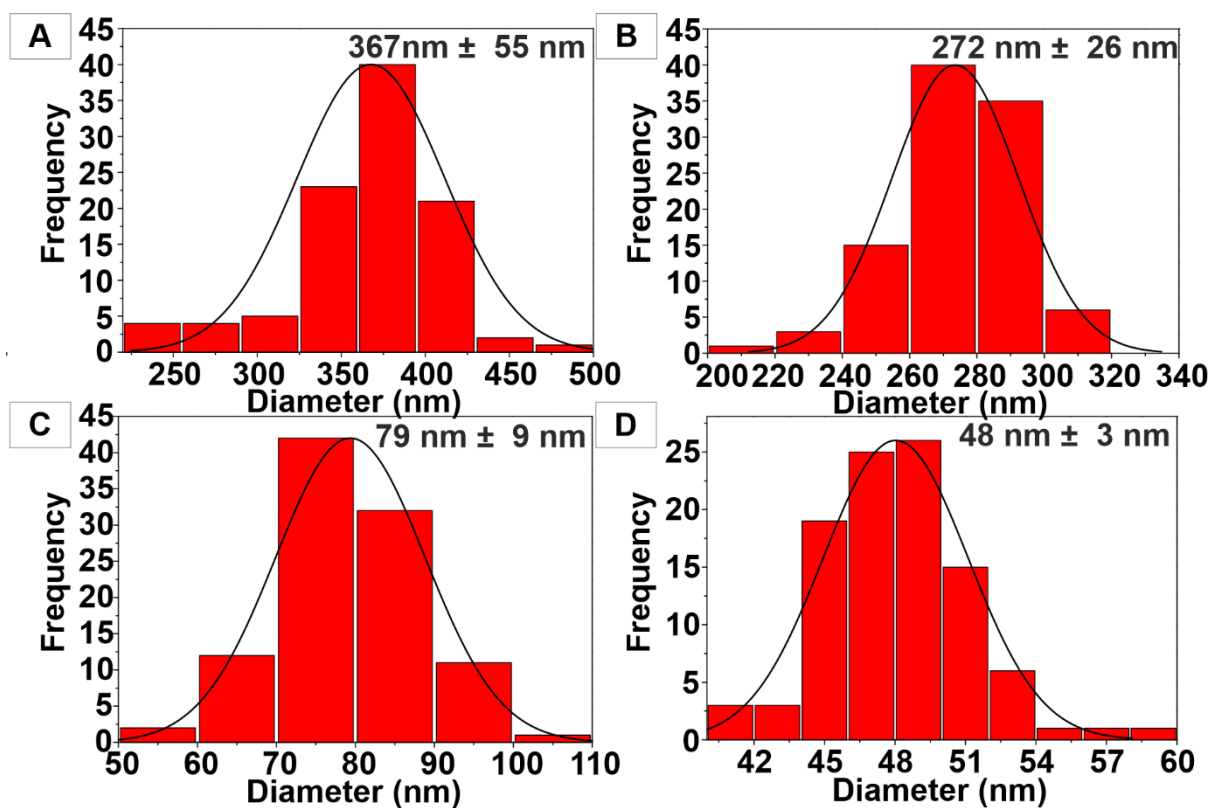
Figure 3.10. Particle size distributions obtained by the TEM images for series A. (A) Particles size distribution for sample A_1, (B) sample A_2, (C) sample A_3 and (D) sample A_4 (OPT).
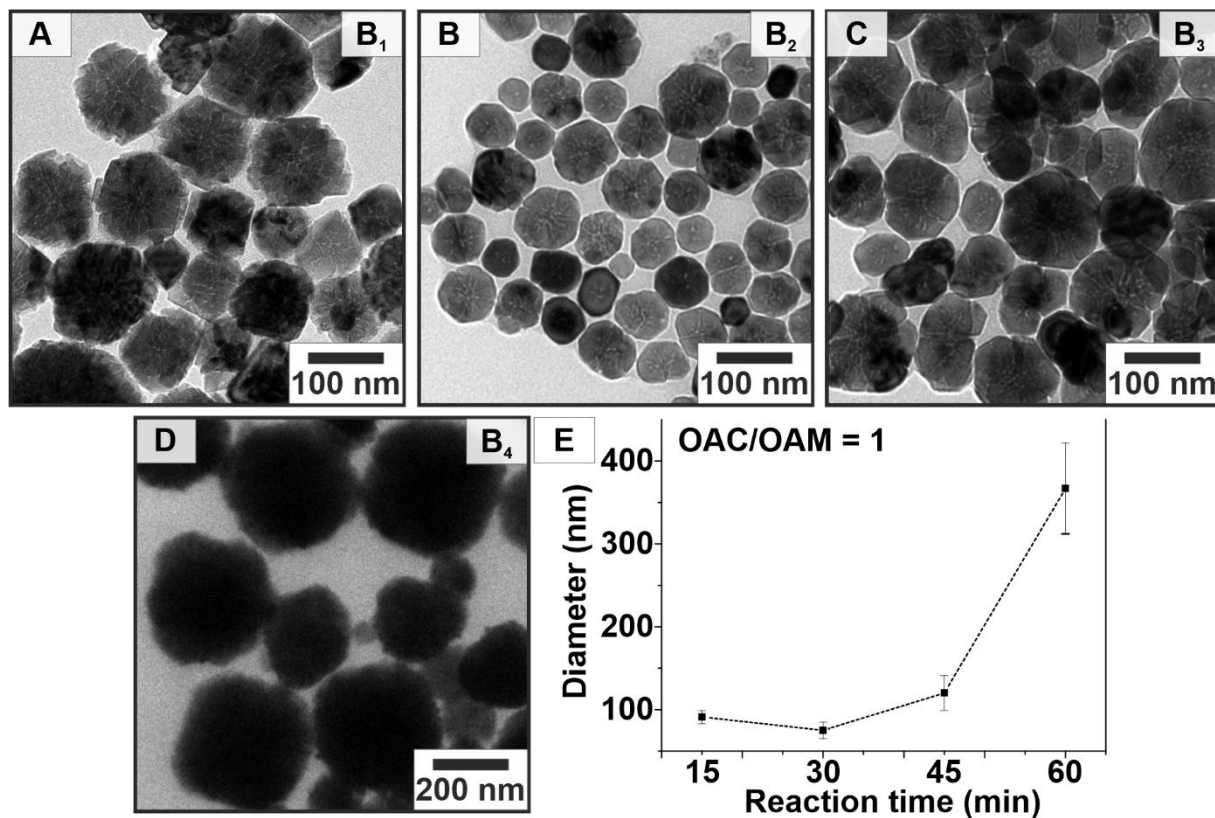
Figure 3.11. TEM snapshots after 15, 30, 45, and 60 minutes for the synthesis of CoO nanoparticles (series B) with a concentration of 3 mmol for each, OAC and OAM. (A) After 15 minutes at 330 °C, (B) 30 minutes, (C) 45 minutes and (D) 60 minutes. (E) Size evolution as a function of the reaction time.
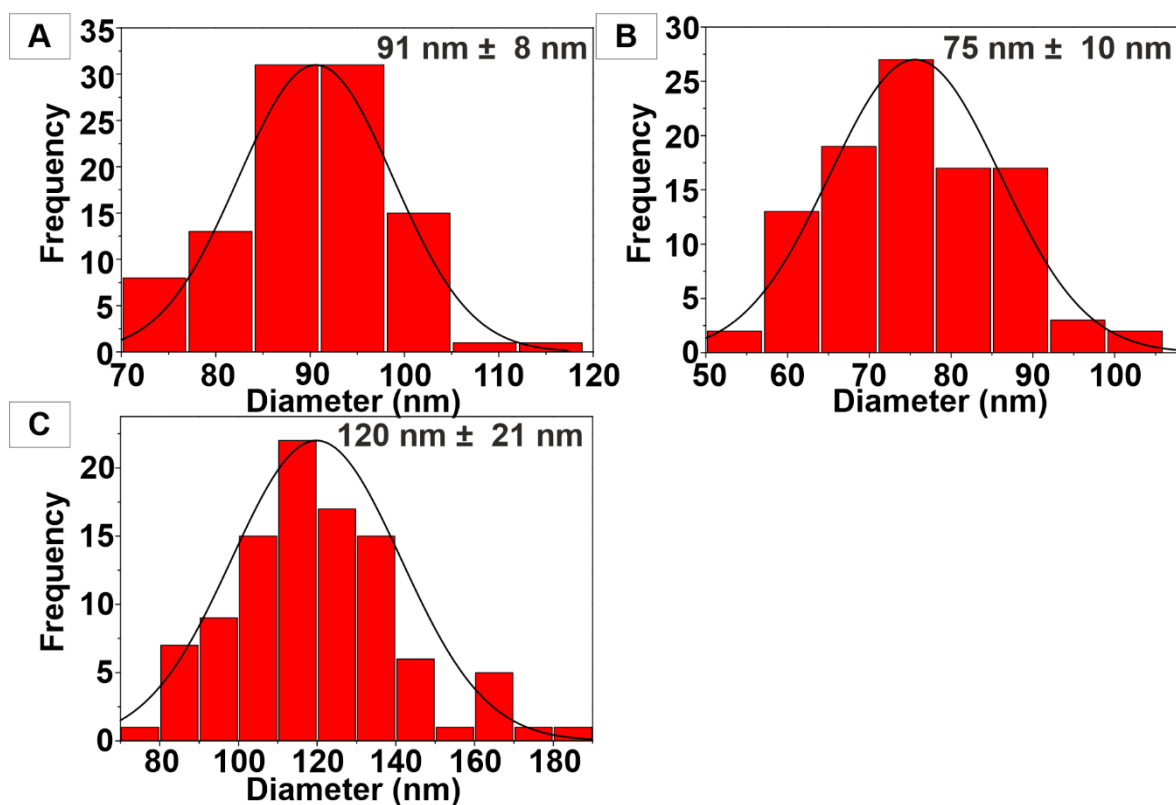
Figure 3.12. Particle size distributions for the synthesis of CoO nanoparticles obtained from TEM snapshots after 15, 30, 45 and 60 min (series B). (A) Particles size distribution for 15 minutes reaction time, (B) 30 minutes, (C) 45 minutes. The particle size distribution for 60 minutes is shown in Figure 3.10A (sample $B_4 = A_1$).
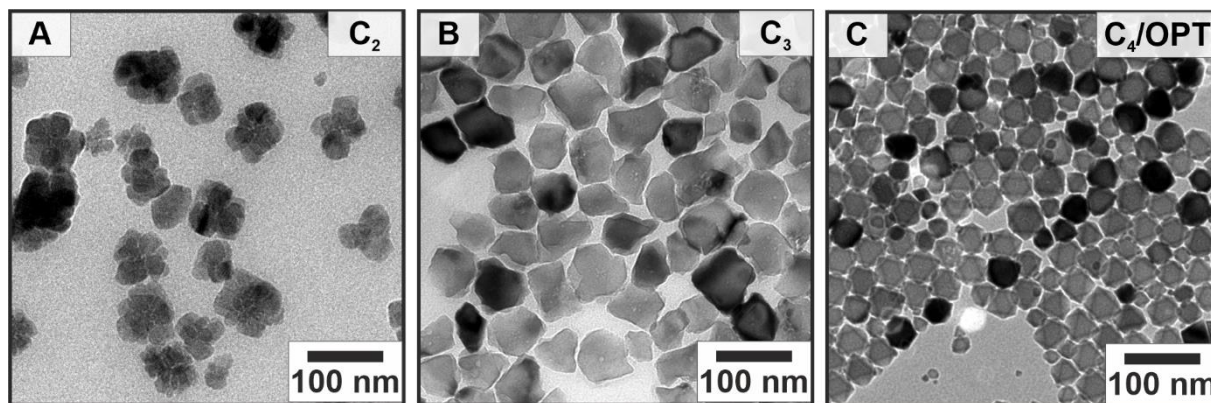
Figure 3.13. TEM snapshots after 15, 30, 45 and 60 min (series B) for the synthesis of CoO nanoparticles with a concentration of 12 mmol for each, OAC and OAM. After 15 minutes no conversion had occurred. (A) After 30 minutes at 330 °C, (B) 45 minutes and (C) 60 minutes (OPT).
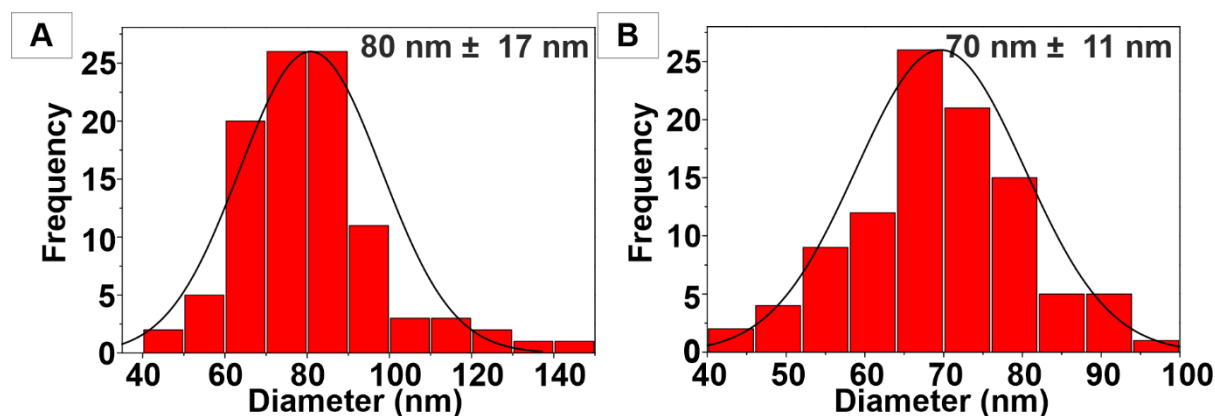
Figure 3.14. Particle size distributions for the synthesis of CoO nanoparticles obtained from TEM snapshots after 15, 30, 45 and 60 min (series C). (A) Particles size distribution for 30 minutes reaction time and (B) 45 minutes reaction time. Particle size distribution for 60 minutes (OPT) is shown in Figure 3.10D.
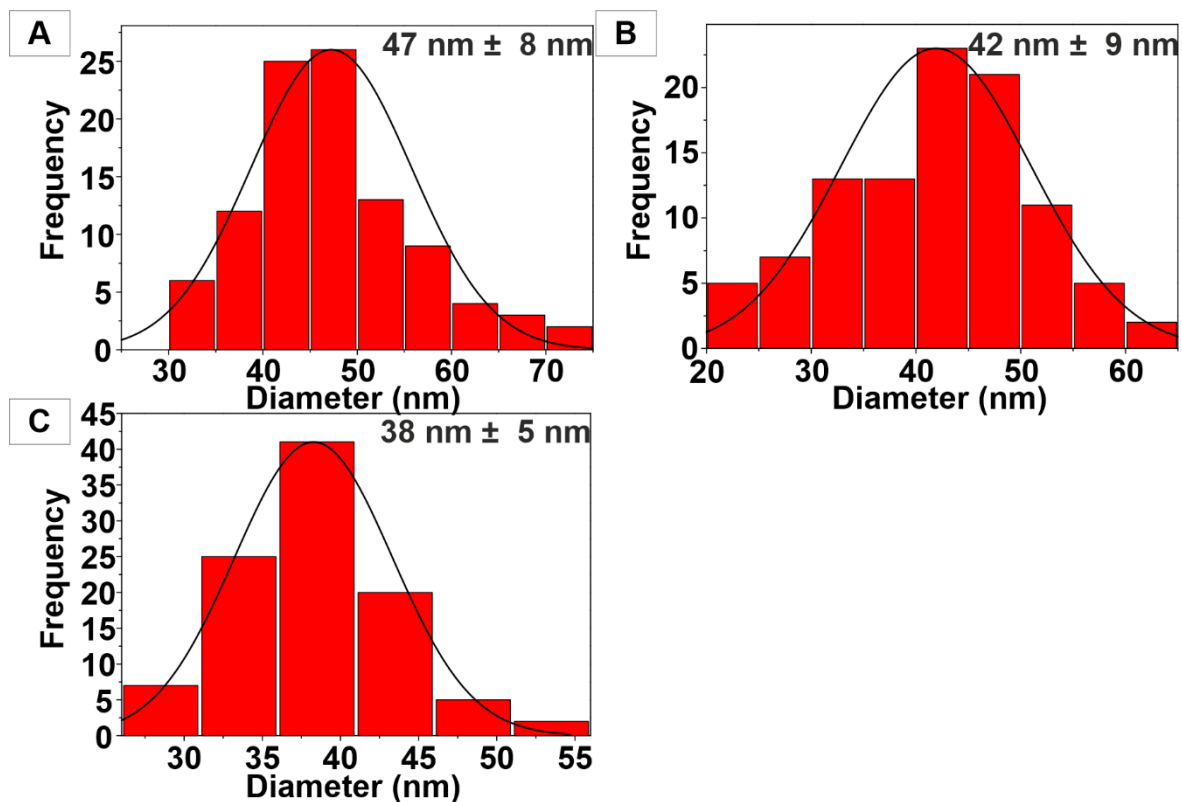
Figure 3.15. Particle size distributions obtained from TEM images for the synthesis of CoO nanoparticles (series D). (A) Particles size distributions for sample D_8, (B) sample D_7, and (C) sample D_6.
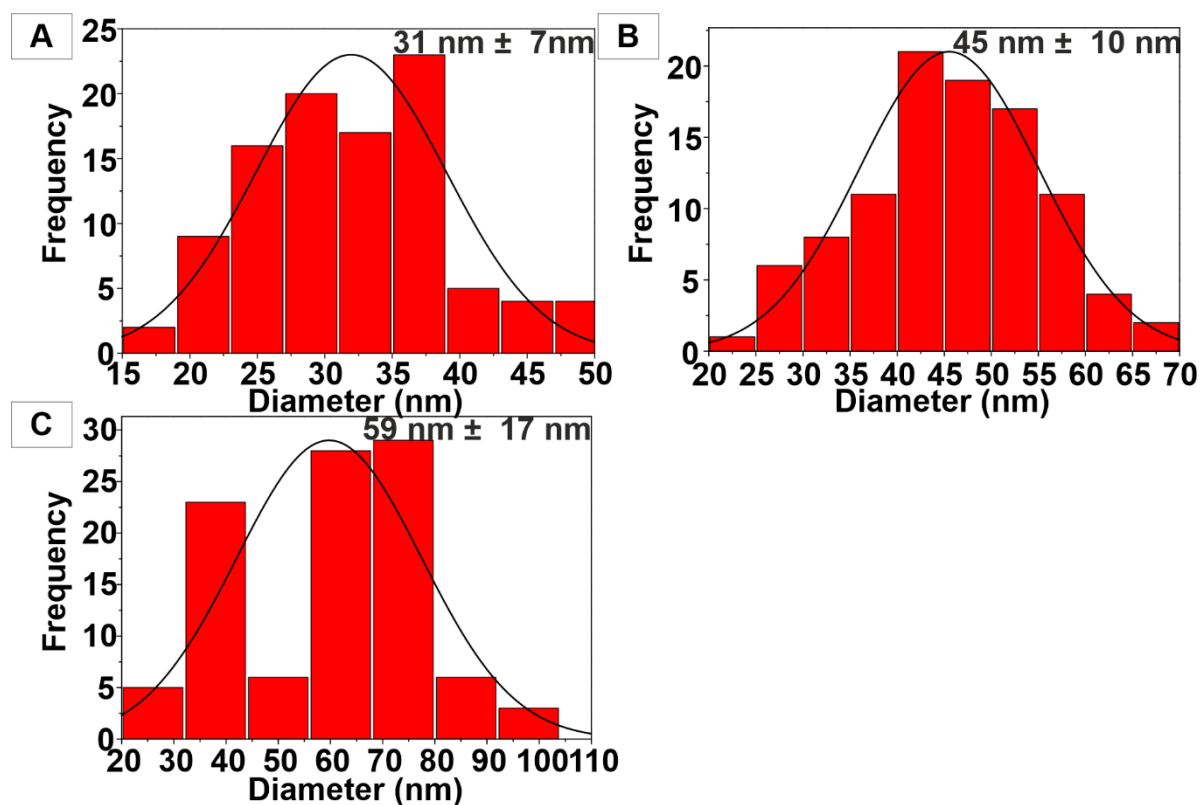
Figure 3.16. Particle size distributions obtained from TEM images for the synthesis of CoO nanoparticles (series F). (A) Particle size distribution for sample F_2, (B) sample F_3 and (C) sample F_4.
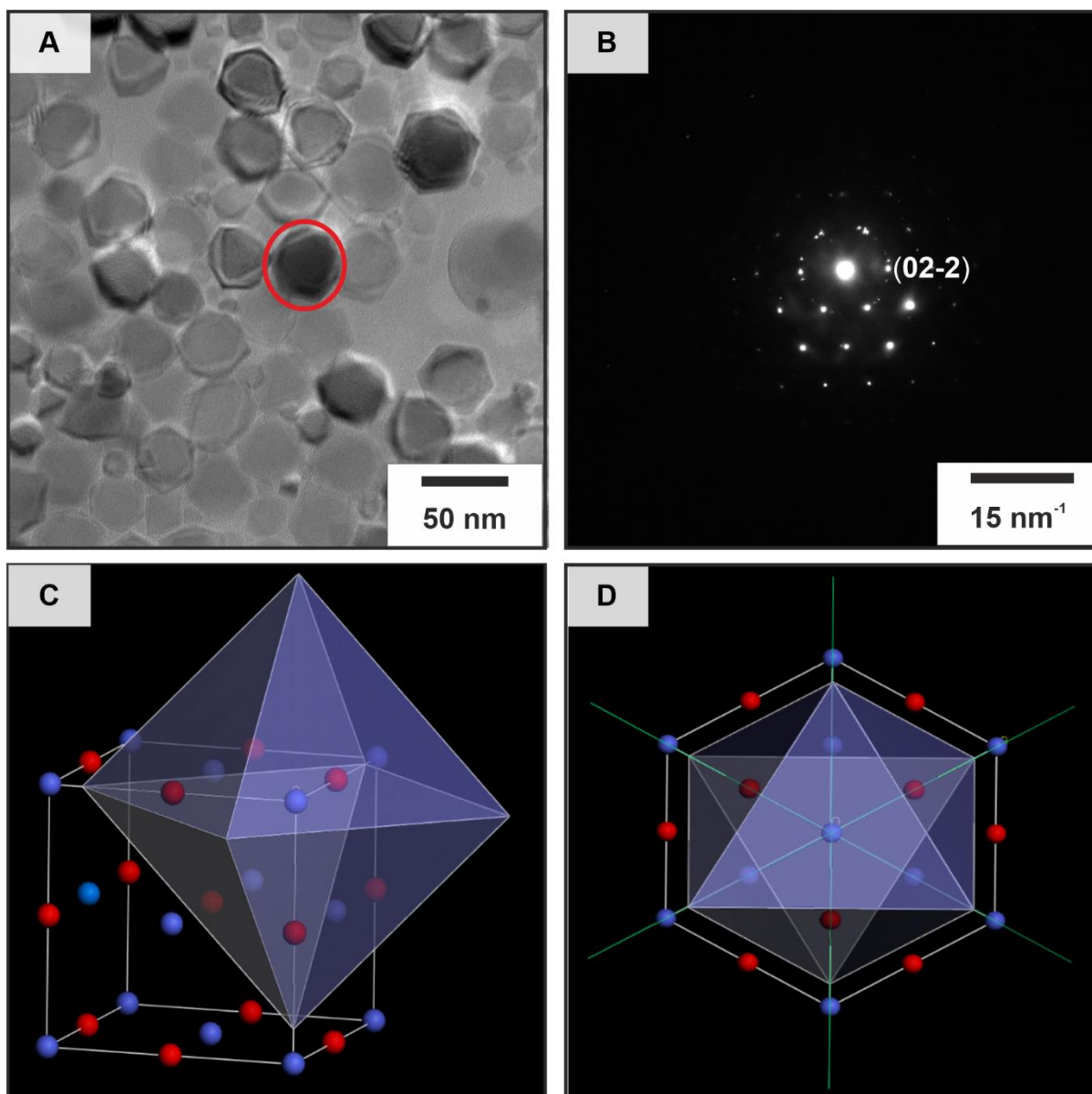
Figure 3.17. Phase analysis of sample OPT. (A) HRTEM image of sample OPT, the red circle marks the corresponding particle on which SAED measurements were performed. (B) SAED, the indexed diffraction pattern corresponds to a distance of 1.53 Å, corresponding to the {022} planes. (C) Crystal facets for CoO, with minimized {001} planes, the red atoms represent oxygen, while blue atoms represent cobalt. (D) Projection through the [111] direction, the green line corresponds to the {022} planes, perpendicular to the (111) plane.
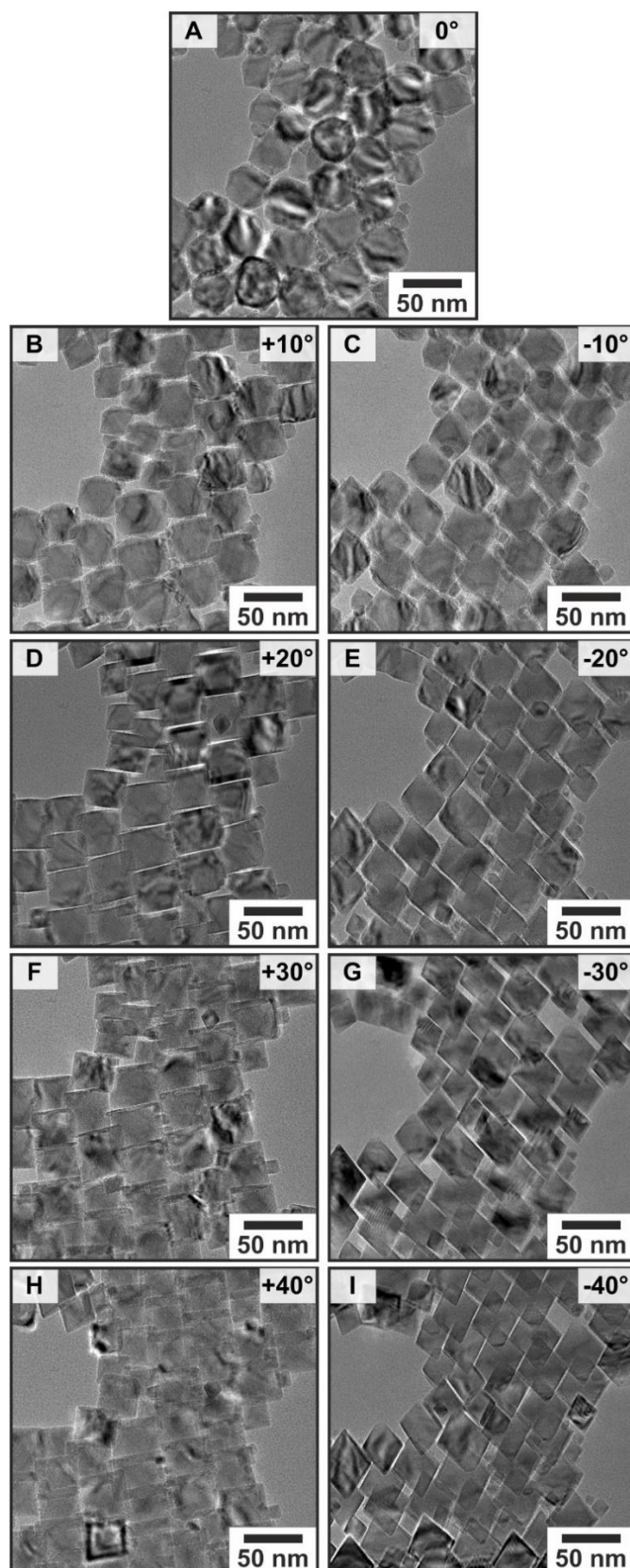
Figure 3.18. HRTEM tilt series of the optimized synthesis OPT. (A) HRTEM image at 0° tilt. (B) At +10° and (C) -10°. (D) At +20° and (E) -20°. (F) At +30° and (G) -30°. (H) At +40° and (I) -40.°
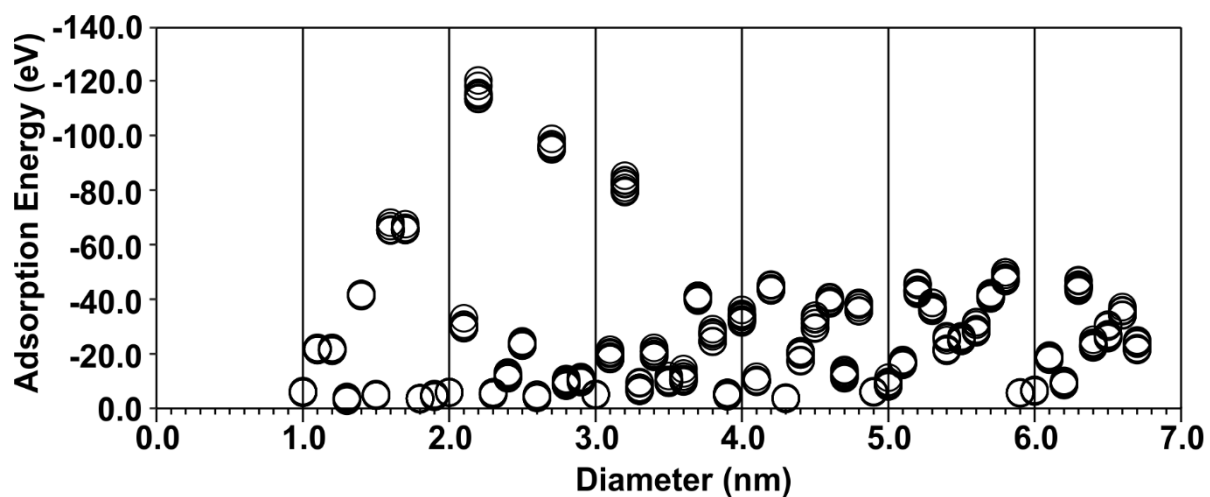
Figure 3.19. Adsorption energy vs. nanoparticle size. The nanoparticles with diameters of 2.7 nm (representative of "small" nanoparticles) and 3.2 nm (representative of "large" nanoparticles) were selected since these have both (i) the highest probable adsorption energy as well as (ii) the smallest spread in the values.
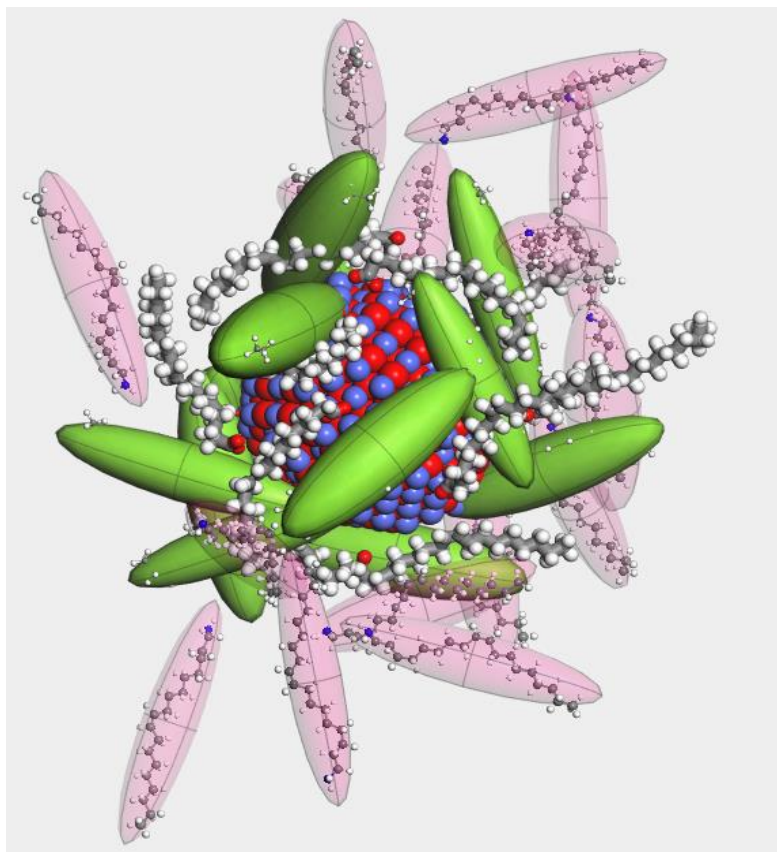
Figure 3.20. Representative energy- and geometry – optimized simulated systems. The red atoms are Oxygen, the purple is Cobalt, the green molecules are OAC molecules that have chemisorbed onto the Co *via* the carboxyl function group, the pink molecules are the OAM molecules (not adsorbed) and the remaining molecules are OAC that have only physisorbed and not chemisorbed onto the CoO.
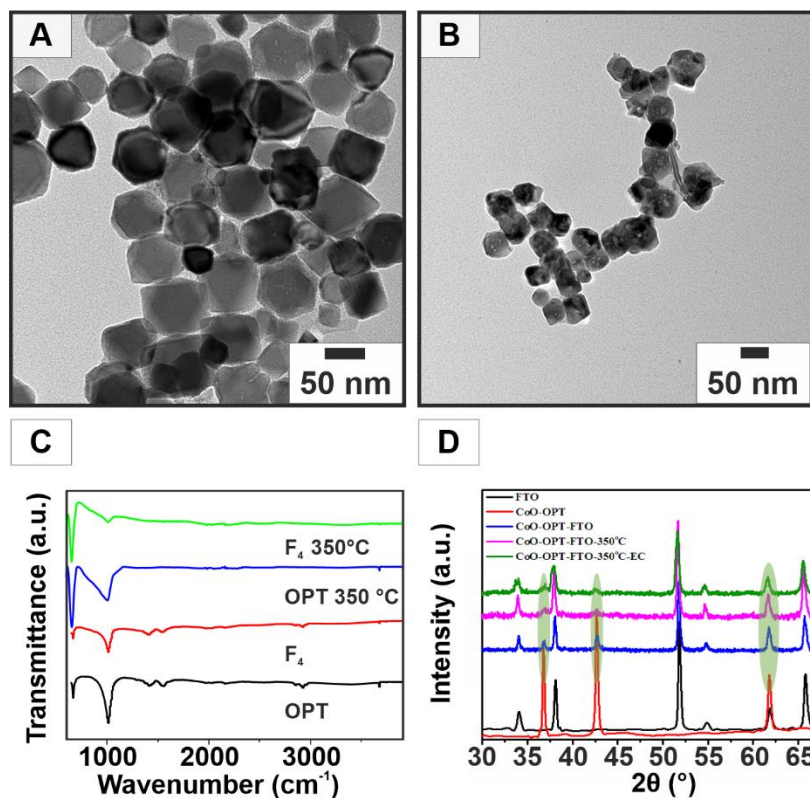
Figure 3.21. Analysis for the OER. TEM images of the annealed samples (A) OPT and (B) F$_4$ with the corresponding (C) FT-IR spectra. (D) XRD patterns of sample OPT (red), FTO (black), OPT-FTO (blue), OPT-FTO annealed at 350 °C (violet) and OPT-FTO annealed at 350 °C, after OER.

4. A Simple Microfluidic Benchtop System for High-Throughput Synthesis of CeO₂
Nanoparticles in Segmented Flow for Highly Transparent Nanocomposites Repelling
Pseudomonas aeruginosa PA14 Biofilms

4. A Simple Microfluidic Benchtop System for High-Throughput Synthesis of CeO₂ Nanoparticles in Segmented Flow for Highly Transparent Nanocomposites Repelling *Pseudomonas aeruginosa* PA14 Biofilms
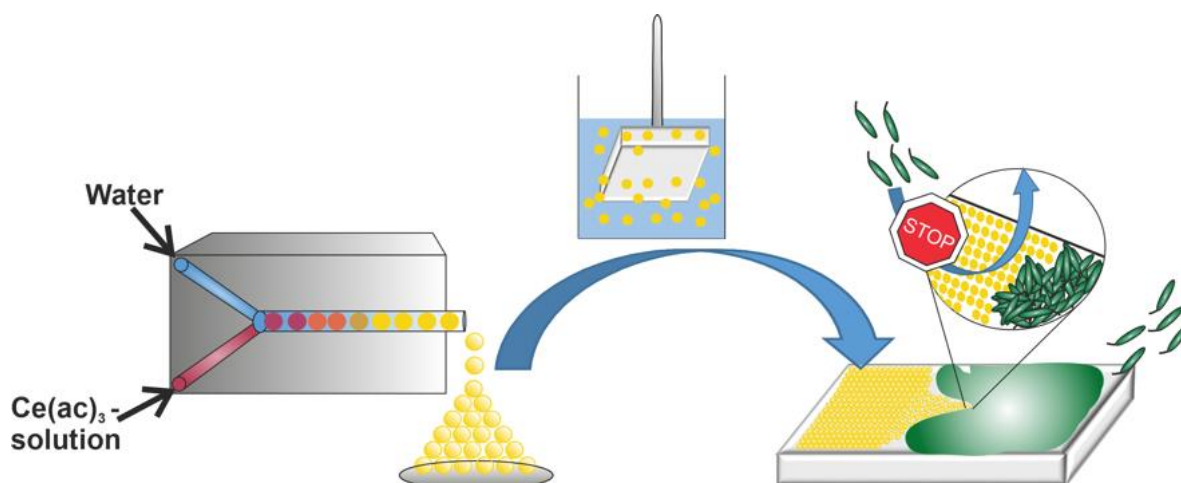
The following chapter is revised and resubmitted for Advanced Materials Interfaces. In the appendix of the dissertation a detailed authorship statement with the contributions of each author is attached.

4.1. Abstract

Transparent, hardened CeO_2/polycarbonate surfaces that prevent adhesion, proliferation, and spread of *Pseudomonas aeruginosa* PA14 were manufactured. Large amounts of monodisperse CeO_2 nanoparticles for this application were synthesized in segmented flow using a high-throughput microfluidic benchtop system using water/benzyl alcohol mixtures and oleylamine as capping agent. This reduced the reaction time for nanoceria by more than one order of magnitude compared to conventional batch methods. Ceria nanoparticles prepared by segmented flow showed high catalytic activity in halogenation reactions, which makes them highly efficient functional mimics of haloperoxidase enzymes. Haloperoxidases are used in nature by macroalgae to prevent formation of biofilms *via* halogenation of signaling compounds that interfere with bacterial cell-cell communication ("quorum sensing"). CeO_2/polycarbonate nanocomposites were prepared by dip-coating plasma-treated polycarbonate panels in CeO_2 dispersions. These showed a reduction in bacterial biofilm formation of up to 85% using *P. aeruginosa* PA14 as model organism. Besides biofilm formation, also the production of the virulence factor pyocyanin is under control of the entire quorum sensing systems *P. aeruginosa*. CeO_2/PC showed a decrease of up to 55% in pyocyanin production, whereas no effect on bacterial growth in liquid culture was observed. This indicates that CeO_2 nanoparticles affect quorum sensing and therefore inhibit biofilm formation in a non-biocidic manner. The engineered polycarbonate surfaces have the promise to repel biofilms as green antimicrobials on plastics (drinking bottles, glasses, food containers), where biocides are prohibited, or on touch panels and portable devices for consumer electronics (e.g., mobile phones).

4.2. Introduction

Biofilms are an accumulation of microorganisms, mostly bacteria, living in close community within a mucous substance.[1] They can form on almost any surface. Typical examples are plastic surfaces in the domestic environment (e.g. shower curtains, touch surfaces),[2] or on consumer electronics[3] Many industries suffer from the ill-effects of biofilm growth, which leads to costs for cleaning and maintenance.

There are different strategies for the design of antibiofouling surfaces: (i) coating with antimicrobial materials,[4] (ii) inhibit adhesion with hydrophilic surfaces, like polyethylene glycol (PEG) polymers,[5] with zwitterionic materials,[6] amphiphilic block copolymers,[5,7] and

4. A Simple Microfluidic Benchtop System for High-Throughput Synthesis of CeO₂
Nanoparticles in Segmented Flow for Highly Transparent Nanocomposites Repelling
Pseudomonas aeruginosa PA14 Biofilms

stimuli-responsive materials,[8] (iii) micro-nano structuring,[9] (iv) photoactivation of surfaces,[10] or (v) superamphiphobic or -oleophobic surfaces[11] that mimic the architecture of the lotus leaf.[12] Each of them has its limitations, such as mechanical weakness, poor substrate adhesion, non-uniform coating, leaching of toxines, insufficient long-term stability, low biocompatibility or cost-benefit ratio. A simple, sustainable, and inexpensive method to prepare durable, polymer surfaces with uncompromised mechanical properties, which repel a variety of contaminants, has immediate relevance in many applications that suffer from the above issues. A new and environmentally benign solution is inspired by nature. Macroalgae have evolved molecular mechanisms to limit biofilm formation (biofouling) of their surfaces.[13] The lack of microbial fouling of these algae is associated with the formation of brominated furanones that inhibit bacterial quorum sensing,[32] a process by which bacteria monitor cell density and regulate their communal behavior such as biofilm formation, virulence, or swarming motility among other responses.[14-16] Many bacteria secrete small signaling molecules, called autoinducers (AI) as their quorum sensing compounds.[14] The halogenated messenger compounds have been shown to disrupt quorum sensing by displacing the signaling molecules from their corresponding receptor or by covalent modification, i.e. inactivation of the associated enzyme.[14-16]

These biohalogenation reactions are catalyzed by haloperoxidases (HPOs), a group of enzymes that use hydrogen peroxide, generated in micromolar quantities in sunlight, and halides (Cl^-, Br^-) to form hypohalous acids (HOX, X = Cl, Br). These short-lived reaction intermediates are powerful halogenating and oxidizing agents that halogenate a wide range of substrates.[17-19] Some halogenated metabolites have antimicrobial activity and/or prevent the formation of biofilms, i.e., Nature uses oxidative halogenation as a chemical defense strategy against biofouling.

Several metal complexes,[20-24] V_2O_5,[25] and CeO_2[26] nanoparticles (NPs) can mimic the catalytic activity of haloperoxidase enzymes under ambient conditions.[27] Therefore, these NP enzyme mimics[28-31] display a sustained and long-term activity at ambient conditions to produce sufficient amounts of hypohalous acids to prevent biofouling in moist environments or surface water films.[32] Incorporating these nanomaterials in polymers or coatings may reduce biofilm formation and lead to materials with long-term stability. Assuming that concentrations of halide anions and peroxide on polymer surfaces are similar as in natural waters, a related behavior might be expected on polymer coatings.[33,34] This may open new and sustainable applications in everyday life (e.g. textiles, touch surfaces, food packaging, foils) and circumvent

the use of biocides like silver or copper ions, antibiotics, chlorohexidine, or quaternary ammonium salts.[35,36]

Nanoceria is biologically benign.[37-39] Its application in transparent polymer coatings or nanocomposites requires large-scale synthesis of non-aggregated CeO_2 NPs with well-defined size and crystallinity to enable blending or dispersing NPs in polymers with high optical transparency while maintaining antibacterial properties. Large scale routes to nanoceria are based on high-temperature gas phase reactions, which lead to highly agglomerated particles incompatible with the required transmittance and low haze in display films, coatings or lenses. Precipitation in batch reactors is a straightforward route to ceria NPs, but it suffers from long cycle times and difficulties in controlling particle size due to poor heat and mass transfer. Alternative routes to CeO_2 NPs are sol-gel or hydrothermal/solvothermal synthesis.[40] The size and morphology of CeO_2 NPs can be tailored by adjusting the process parameters (e.g. pH value, reaction time, counter ions and addition of surfactants).[41-45] Larger quantities of NPs (e.g. ceria, yttria, and zirconia nanoceramics) with low polydispersity and control over particle size can be obtained by continuous flow synthesis.[46-50] However, these reactions require high energy input, special equipment and they are difficult to parallelize.

Here we present a simple and highly scalable microfluidic benchtop system for high-throughput synthesis of CeO_2 NPs with homogeneous size, morphology and crystallinity in segmented flow. The synthesis was carried out with oleylamine and cerium(III)-acetate in benzyl alcohol as reaction and water as carrier medium. Investigation of their surface chemistry revealed a very high haloperoxidase-like activity of the CeO_2 NPs. Surface coating of polycarbonate panels with CeO_2 NPs resulted in transparent nanocomposites with very low surface roughness and an enhanced Young's modulus as a measure of stiffness. CeO_2/PC nanocomposites inhibit bacterial biofilm formation of *P. aeruginosa.* Production of the virulence factor pyocyanin in *P. aeruginosa* showed that the bacteria repelling properties are probably due to *quorum quenching*, an effect also termed *quorum quenching.* CeO_2/PC nanocomposites may find application as biocide-free "green" antimicrobials on plastics for electronic, automotive, aircraft, or railway components, for drinking bottles, glasses and food containers, where traditional biocides are strictly prohibited because of toxicity. In the health sector this may prevent infections that are becoming increasingly troublesome with the emergence of drug resistant bacteria and help reducing the use of antibiotics.

4.3. Results and Discussion

Batch synthesis. A single step approach was devised for the synthesis of ceria NPs based on a non-hydrolytic sol-gel route in benzyl alcohol. It allows excellent control over particle size, phase, and crystallinity, but also simplifies transfer into the flow setup.[51-53] Ce(ac)$_3$ or Ce(acac)$_3$ were used as starting compounds because of their availability and good solubility in benzyl alcohol. In a typical non-hydrolytic sol-gel reaction, the Ce(ac)$_3$ precursor - or secondary complexes - experience an increased thermodynamic driving force to form "monomers". Further reaction of these monomers with benzyl alcohol[51] leads to the formation of CeO$_2$ nuclei. The nucleation of nascent NPs is triggered by heating, and continued heating allows the nuclei to grow into mature NPs. Heating involves specific subtleties resulting from the interplay of reaction variables such as precursor concentration, solvent, reaction temperature and time. All these variables affect the final size and size distribution of the NPs.

A possible scenario could be as follows: In the reaction of cerium acetate hydrate (Ce(ac)$_3$ x H$_2$O) in benzyl ether an acid-base equilibrium ac$^-$ + HOCH$_2$C$_6$H$_5$ = ac-OCH$_2$C$_6$H$_5$ + OH$^-$ precedes the formation of Ce(OH)$_3$ in an initial step at 120°C (from Ce^{3+} and OH$^-$ anions formed in the acid-base equilibrium). Ce(OH)$_3$ is sensitive to aerial oxygen and oxidized to CeO$_2$ in a topotactic condensation reaction, where water is eliminated.[54] In benzyl alcohol this water may be involved in a second acid-base reaction with oleylamine according to H$_2$O + H$_2$N-R = OH$^-$ + $^+$NH$_3$-R. In a competing reaction oleylamine acts as a capping agent in the surface complexation of the growing CeO$_2$ NPs. The hexagonal structure of the Ce(OH)$_3$ intermediate allows topotactic growth of anisotropic particles (e.g., nanorods) of CeO$_2$ (which adopts the cubic fluorite structure).[55] The capping agent plays an important role for the size distribution of the NPs by binding to the growth species and controlling its growth rate.[56-58] Terminating the reaction at this stage leads to the formation of single-domain crystalline CeO$_2$ NPs with diameters of 2-7 nm, which could be dispersed in nonpolar solvents such as cyclohexane or toluene.

Figure 4.1A shows commercially available CeO$_2$ NPs synthesized on an industrial scale. They have an ill-defined morphology and strong agglomeration. For the latter application small NPs with a high surface area are necessary, therefore the control of the morphology and size is mandatory. CeO$_2$ NPs from the batch (high-resolution transmission electron microscopy (HR)TEM images in Figure 4.1B) are much smaller (two orders of magnitude) than their

commercial counterparts and therefore suitable for application in nanocomposites. In the second step, the batch synthesis was transferred into a continuous setup.

Synthesis of CeO$_2$ NPs under segmented flow conditions. The HRTEM micrograph in Figure 4.1C shows that the CeO$_2$ NPs by segmented flow synthesis have essentially the same morphology as those obtained from the batch reaction (Figure 4.1B). Compared to the commercial CeO$_2$ particles (Figure 4.1A) the NPs from the segmented flow synthesis show a uniform morphology and size.
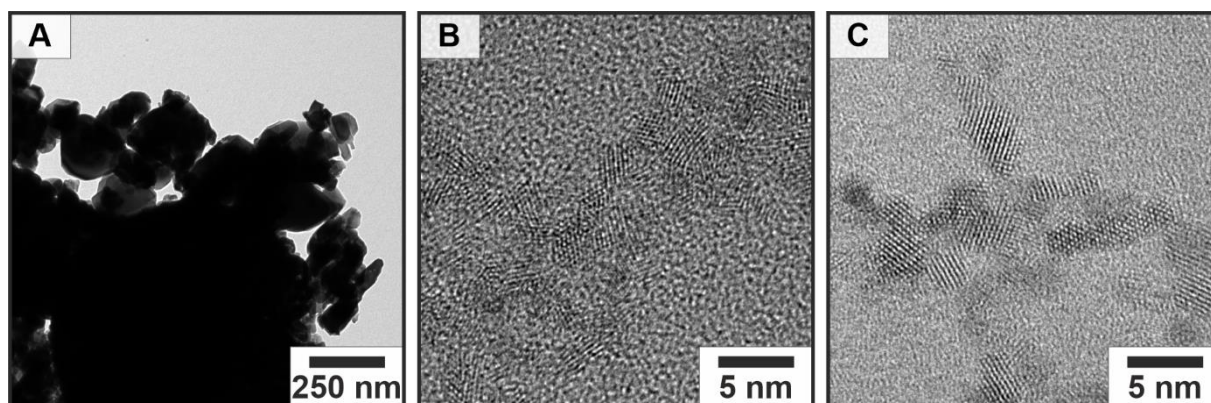
Figure 4.1. (A) TEM image of commercial CeO$_2$. HRTEM images of CeO$_2$ NPs obtained by non-aqueous sol-gel chemistry. (B) NPs obtained from batch chemistry and (C) under segmented flow conditions.

However, clogging of the reactor could not be prevented under continuous flow conditions. Therefore, the synthesis was carried out under segmented flow using water as carrier medium. Advantages of this setup are the low costs and the boiling temperature of water. Water evaporates when the flow passes through the heating element. The water vapor leads to additional pressure between the segmented droplets of the reaction medium and thus prevents – independent of the flow rate – clogging of the reaction channel. A constant flow rate of the reaction medium and the water through the PTFE tube was achieved with a peristaltic pump. Nucleation was triggered by warming the reactant stream in a heating element.

Two heating elements (120° and 180°C) were used to simulate the temperature profile of the batch process. The setup is shown in Figure 4.9 (SI). The suitability of the PTFE tubing for the thermally induced formation of CeO$_2$ NPs was assessed in preliminary experiments under continuous flow conditions. The residence times in each oil bath was set to 2.7 min to simulate the reaction conditions from the batch synthesis (*vide supra)*. The reaction solution had a reddish color and turned purple after passing through the tubes. Two phases were obtained: the

upper phase was an emulsion of water, benzyl alcohol and oleylamine, the lower phase contained the precipitated yellow NPs (Figure 4.9 (SI)).

Importantly, the reactions could be carried out in automated form with much shorter reaction times. For the batch synthesis, the product yield was 0.7 mg/min, while 15.8 mg/min (i.e., 22 times as much) were produced at the same temperature in segmented flow (Figure 4.9 (SI)). The average crystallite sizes of the NPs (bulk sample) were determined by powder X-ray diffraction (PXRD, Figure 4.2 red line) and Rietveld refinement (blue line, difference green line).[59,60] Details concerning the refinement are given in the Supporting Information (Table 4.1-2 (SI)). The NPs are single-crystalline. The X-ray diffractograms of the CeO$_2$ NPs by batch synthesis (Figure 4.2A.1) are very similar to those obtained by segmented flow reaction (Figure 4.2A.2) and show the expected intensities for (bulk) CeO$_2$ (lattice parameter a = 5.42 Å). Reflection broadening allowed extracting the particle size (average 3.2 nm and 5.8 nm by Rietveld analysis of the PXRD patterns for CeO$_2$ NPs (batch/segmented flow synthesis). The morphologies of the NPs from both processes are similar, the NPs from segmented flow process are slightly larger than those obtained by batch synthesis. However, a scale up was possible, due to the segmented flow setup, which avoided clogging of the tubes, i.e., it allows a high-throughput automated synthesis single crystalline CeO$_2$ NPs in large quantities.

Surface chemistry of CeO$_2$ NPs. The oleylamine surfactant required an analysis of the CeO$_2$ surface chemistry to assess the effect of the organic ligands on the catalytic activity. FT-IR spectroscopy was used to identify the surface ligands of the as-synthesized CeO$_2$ NPs. Figure 4.2B shows the spectrum of pure oleylamine. The spectra of the CeO$_2$ NPs from the batch (Figure 4.2C) and the segmented flow synthesis (Figure 4.2D) indicate the presence of surface-bound oleylamine. The broad band between 3500 cm^{-1} and 3000 cm^{-1} envelopes the symmetric and asymmetric O-H stretches. The bands around 2920 cm^{-1} and 2850 cm^{-1} are characteristic for the C-H stretch of the terminal CH$_3$ group.[56] The absorptions in the range of 1550 cm^{-1} to 1400 cm^{-1} and in the range from 1250 cm^{-1} and 1400 cm^{-1} and close to 1000 cm^{-1} are typical for the stretching and bending vibrations surface-bound bi- and polydentate carbonate groups.[61] The surfactant coverage was determined by TGA (Figure 4.2E-F).
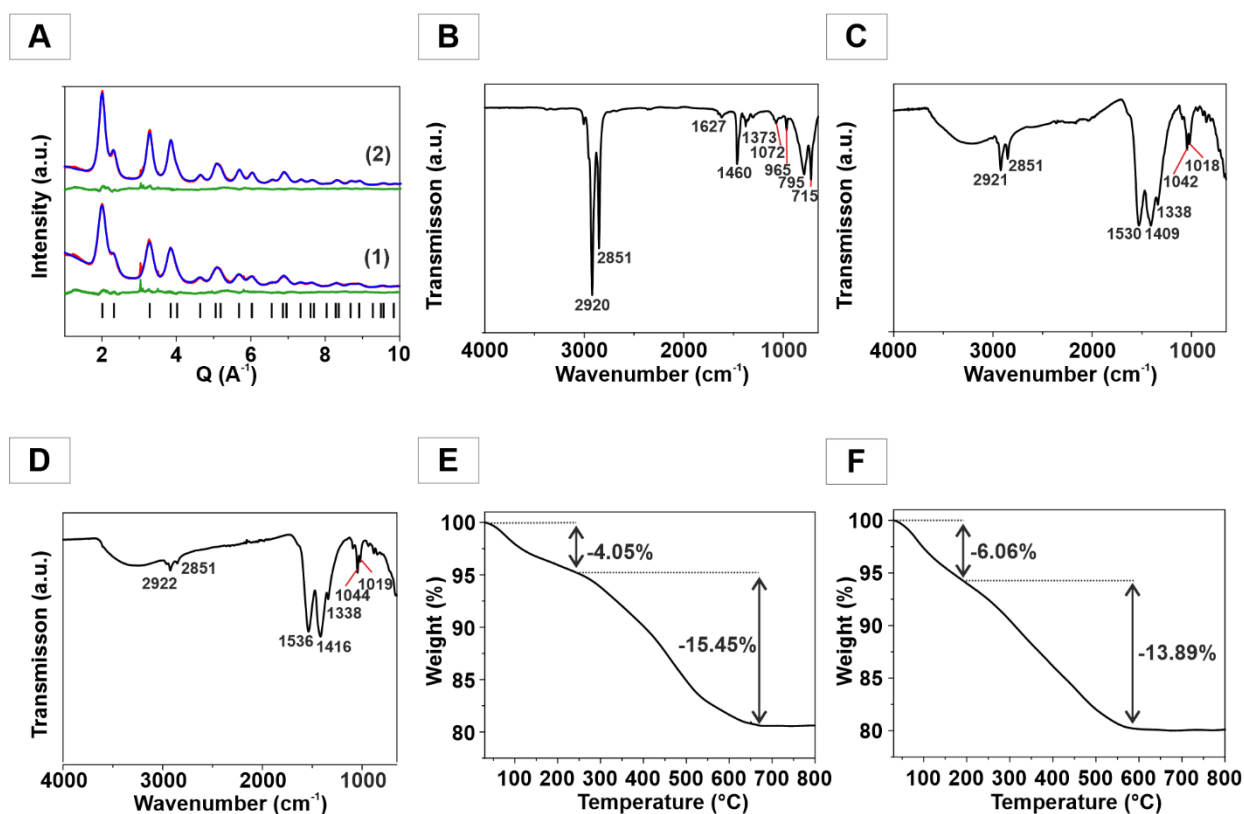
Figure 4.2. (A) X-ray powder diffraction patterns with Rietveld refinements of CeO_2 NPs obtained by batch synthesis (1) and under segmented flow conditions (2). Experimental data (red line), Rietveld refinement (blue line), difference curve (green line). Ticks indicate theoretical positions of Bragg intensities. FT-IR spectra of (B) pure oleylamine, (C) CeO_2 NPs obtained from batch chemistry, and (D) under segmented flow conditions. TGA traces of CeO_2 NPs obtained under (E) batch and (F) segmented flow conditions.

Figure 4.2E shows thermogravimetric traces of the CeO_2 NPs from the batch synthesis. The first step in the diagram is associated with a mass due to surface-bound H_2O ($\Delta m_{rel} = 4.05\%$). This step is initiated between 50 °C and 200 °C. Between 200 °C and 650 °C there is another mass drop corresponding to the remaining organic residues and traces of carbonate being stripped off ($\Delta m_{rel} = 15.45\%$). The remaining solid material was CeO_2. NPs obtained under segmented flow (Figure 4.2F) contained a higher amount of surface-bound H_2O ($\Delta m_{rel} = 6.06\%$) because they were prepared in aqueous environment, while the mass loss of organic residues and carbonate was lower ($\Delta m_{rel} = 13.89\%$) compared to the batch synthesis. The FT-IR spectra of the products obtained by batch and segmented flow synthesis (Figure 4.2C-D) show a weaker intensity of the vibration at around 2920 cm^{-1} and 2850 cm^{-1} for the C-H stretch of the terminal CH_3 group. This indicates a lower share of surface-bound oleylamine. Consequently, a larger amount of H_2O was bound onto the surface. Based on the spectroscopic and thermoanalytical data a temperature-dependent (185 °C, 500 °C, 800 °C) analysis of surface chemistry and the resulting catalytic activity of the NPs was carried out.

X-ray analysis of the CeO_2 NPs from the batch preparation (Figure 4.3A.1) and segmented flow synthesis after annealing for 5h at 185 °C (Figure 4.3A.2) showed no significant changes compared to their non-annealed counterparts (Figure 4.2A). CeO_2 NPs from segmented flow synthesis were also annealed for 5h at 500 °C and 800 °C. The NP diameter increased from 5.8 nm (185 °C) to 16.2 nm (500 °C) and finally to 71.5 nm (800 °C). The sharp reflections at 500 °C and 800 °C (Figure 4.3B-C) and the HRTEM images (Figure 4.10A-C (SI)) show the increase in particle size. Since particle diameter correlated with surface area in an inverse fashion, the surface area was reduced at high annealing temperatures (Figure 4.3D). The surface area for the NPs prepared at ambient temperature was 184 m^2 g^{-1}. It increased to 190 m^2 g^{-1} after annealing at 185 °C. Surface ligands of the CeO_2 NPs (ambient temperature) may cause errors in the BET measurements. Therefore, the surface area increased - formally - slightly after annealing, even though it is unfeasible physically. The surface areas decreased at higher temperatures to 78 m^2 g^{-1} (500 °C) and 17 m^2 g^{-1} (800 °C) due to grain growth.

The FT-IR spectra of the CeO_2 NPs (batch preparation and segmented flow synthesis) showed after annealing for 5h at 185 °C (Figure 4.3E) no organic ligand anymore, indicated by the absence of the bands around 2920 cm^{-1} and 2850 cm^{-1}, which are characteristic for the C-H stretch of the terminal CH_3 group.[56] The absorptions at 1570 cm^{-1}, between 1250 cm^{-1} and 1400 cm^{-1} and close to 1000 cm^{-1} are typical for the stretching and bending vibrations of surface-bound bi- and polydentate carbonate groups.[61-63] CeO_2 shows acid/base properties. Its acidic behavior is responsible for OAM surface binding. Its base properties are responsible for the binding of carbonate groups. This binding of carbonaceous species is responsible for the use of CeO_2 in gas-phase heterogeneous catalysis (e.g. in exhaust catalysts).[64,65] It is also an important feature of hydroxylated and non-hydroxylated CeO_2 NPs in aqueous environment, where active surface sites are blocked by adsorbed species.

After calcination for 5h at 800 °C all vibrational bands of the surface species vanished (Figure 4.3E), and the ζ-potentials of the NPs before and after annealing changed from positive to negative values. For CeO_2 NPs (ambient temperature, segmented flow) an average value of 50.2 mV ± 1.5 mV was obtained. After annealing for 5h at 185 °C the ζ-potential decreased slightly to 47.3 mV ± 0.12 mV. Annealing for 5h at 500 °C reduced the ζ-potential to -4.78 mV ± 0.17 mV, and after annealing for 5h at 800 °C it was -18.9 mV ± 0.59 mV (Figure 4.3F).
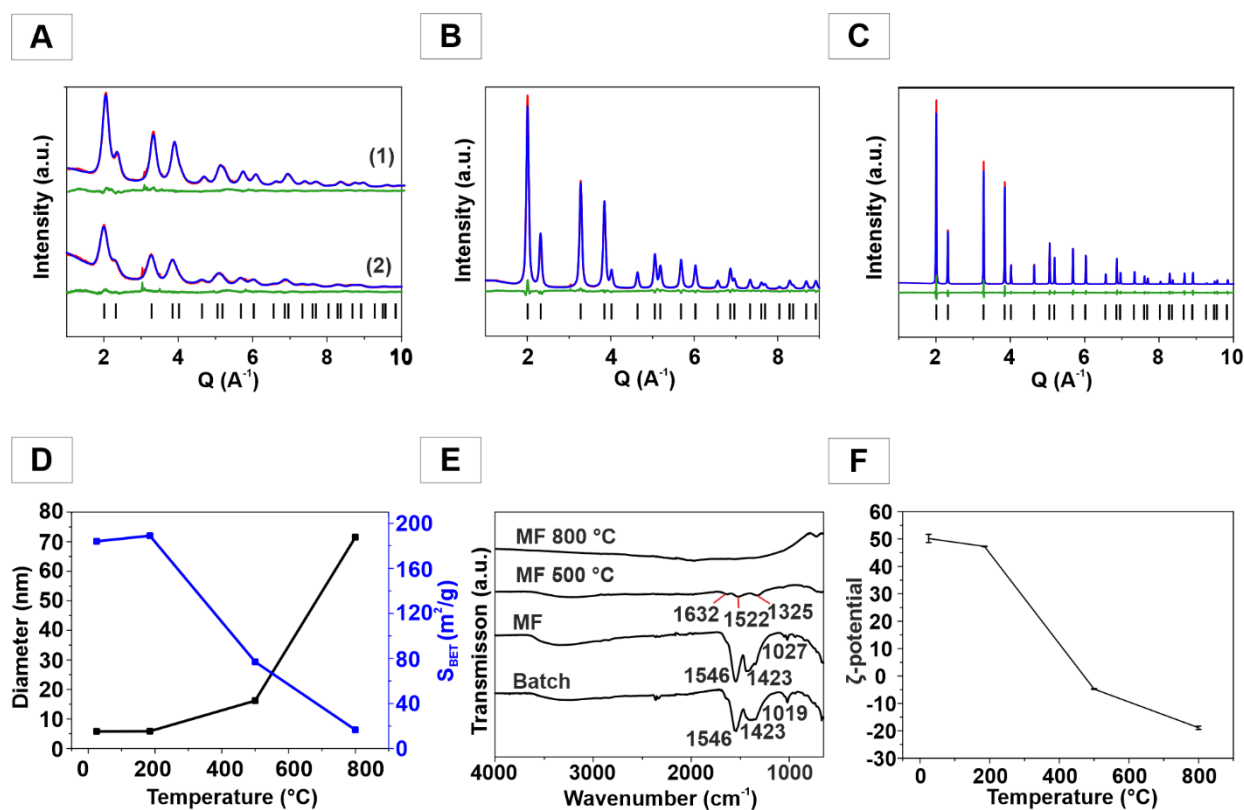
Figure 4.3. X-ray powder diffraction patterns with Rietveld refinements of CeO$_2$ NPs obtained by batch synthesis (A1) and under segmented flow conditions (A2) after annealing for 5h at 185 °C. (B) CeO$_2$ annealed for 5h at 500 °C and (C) 800 °C. Experimental data, Rietveld refinement and difference curve are shown as red, blue and green lines. Ticks indicate calculated positions of the Bragg intensities. (D) Average diameter and surface area as a function of annealing temperature. (E) FT-IR spectra of as-synthesized CeO$_2$ NPs for different annealing temperatures and (F) ζ-potential as a function of annealing temperature.

Haloperoxidase activity. The haloperoxidase activity of CeO$_2$ NPs was determined by UV/Vis spectroscopy with the phenol red (PR) assay (Figure 4.4A). The spectra in Figure 4.4B-C show the time-dependent intensity change of the two principal absorption bands for PR for CeO$_2$ NPs (batch or segmented flow synthesis, after annealing at 185 °C) as haloperoxidation catalyst. The spectral changes and the slope of the absorbance correspond to the reaction rate. Figure 4.4D-E show the absorbance change for PR at 590 nm measured as a function of time for CeO$_2$ (catalyst, 25 µg/mL), H$_2$O$_2$ (300 µM), PR (50 µM) and KBr (25 mM). The shift of the absorption bands is due to the fourfold oxidative bromination of PR to tetrabromophenol blue (TBPB)

As the haloperoxidase activity depends on the concentration of the H$_2$O$_2$ substrate, the Michaelis-Menten kinetics was evaluated by varying the H$_2$O$_2$ concentration. The kinetic data were fitted using the Hill equation. Table 1 shows the parameters derived from a fit to the Hill equation (Figure 4.11 (SI)). Evaluating the kinetic parameters for CeO$_2$ NPs obtained from the

segmented flow synthesis (ambient temperature) was not possible, because their water dispersibility was low due to the OAM surface ligands.
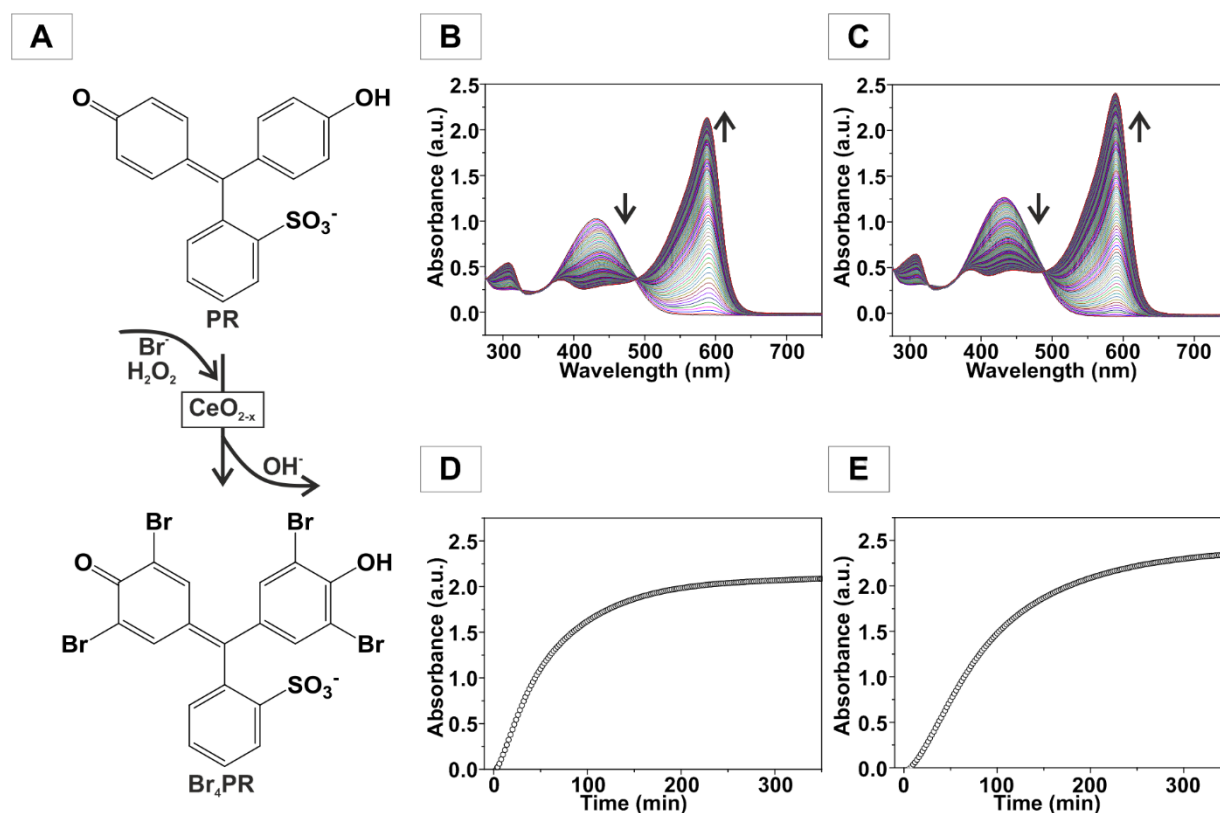

Figure 4.4. Scheme of the (A) oxidative bromination of PR. Spectral changes induced by the oxidative bromination of PR with time for the determination of the haloperoxidase activity of CeO2 obtained (B) from batch chemistry and (C) under segmented flow conditions after annealing at 185 °C, (D) the corresponding absorbance change at 590 nm as a function of time (E) the corresponding absorbance change. Assay components: CeO2 catalyst (25 µg/mL), H2O2 (300 µM), PR.

Table 4.1. Kinetic parameters with H_2O_2 as substrate derived from the Michaelis-Menten equation.

Sample	v_{max} ($\mu M \; min^{-1}$)	K_m (μM)	n
CeO2 – 185 °C	0.15	470.0	1.47
CeO2 – 500 °C	0.36	296.9	1.15
CeO2 – 800 °C	0.03	575.8	0.82

Brunauer-Emmett-Teller (BET) surface areas were determined to normalize the reaction rates to surface areas between 190 $m^2 \; g^{-1}$ (ambient temperature) and 17 $m^2 \; g^{-1}$ (800 °C). Table 1 shows that the bromination rate increases with the annealing temperature (185 °C vs. 500 °C) for CeO2. Based on the surface areas (190 $m^2 g^{-1}$ vs. 78 $m^2 \; g^{-1}$) and the ζ-potentials

(47.3 mV $\pm$ 0.12 mV vs. -4.78 mV $\pm$ 0.17 mV) one may expect a higher activity for the sample treated at 185 °C. However, the bromination rate appears to depend not only on surface area and ζ-potential. Another factor might be the carbonate surface concentration of the CeO_2 sample annealed at 185 °C, as surface bound CO_3^{2-} groups may quench the reaction or block active sites. After annealing at 800 °C the bromination rate dropped significantly. The saturation rate (K_m value) increased, i.e., the affinity for H_2O_2 decreased. The Hill coefficient decreased initially from 185 °C to 800 °C. Thus, cooperative effects decrease by increasing the annealing temperature from 185 °C to 500 °C and finally to 800 °C. The catalytic activity described in terms of the turnover frequency (TOF) or the catalytic constant (k_{cat})[66] depends on the catalyst surface area, time, and mass concentration. The rate of reaction (ROR) is defined by Eq. (4.1).

$$\text{TOF} = \frac{v_{max}}{[Cat]_0} \xrightarrow{[Cat]_0 \rightarrow S_{BET} \cdot \beta(Cat)} \text{ROR} = \frac{v_{max}}{S_{BET} \cdot \beta(Cat)} \qquad (4.1)$$

Here, the accessible surface area per mass equivalent of the catalyst is expressed through the BET surface (S_{BET} in m^2 g^{-1}). The turnover of PR to TBPB is surface specific because only the catalyst surface is accessible for the substrate. Eq. 4.1 can be evaluated based on time (v_{max}/M min^{-1}), surface area (S_{BET}/m^2 g^{-1}) and mass concentration ($\beta(Cat)$ /g L^{-1}) and yields the molar amount of TBPB that was formed by reaction of HOBr with PR per unit surface and time. The calculated ROR value for CeO_2 (185 °C) is 0.031 µmol m^{-2} min^{-1}, while CeO_2 (500 °C) shows the highest ROR value (0.185 µmol m^{-2} min^{-1}). For the CeO_2 annealed at 800 °C we obtained a value of 0.071 µmol m^{-2} min^{-1}. For the application of CeO_2 NPs on polycarbonate surfaces there are two important requirements . (i) A high surface area to volume ratio is essential for catalytic activity. (ii) High dispersibility of the NPs is necessary to ensure uniform distribution of the NPs on the polycarbonate surface during the dip coating process. In this way, we could fabricate a smooth and transparent nanocomposite. CeO_2 NPs annealed at 185 °C were the most successful candidate.

CeO_2/polycarbonate (PC) nanocomposites. In order to bind a sufficiently large amount of CeO_2 NPs to the PC surface, the PC panels were exposed to an oxygen plasma for 20 min. Contact angle measurements of polycarbonate with water, showed a decrease from 86.75° before treatment to 26.88° after oxygen plasma treatment (Figure 4.12 (SI)), indicating a significant change in surface energy. The plasma treatment generated new oxygen containing groups such as C=O, O-C-C or O-C=O as reported by Shikova et al.[67] Dip-coating of the plasma-treated PC panels in a dispersion of CeO_2 particles in cyclohexane (ambient temperature) and water (185 °C) resulted in the binding of the particles to the polycarbonate surface by condensation reaction between the polar groups of polycarbonate surface and the free hydroxyl

84

groups of the particles leading to a very dense and stable coating of CeO$_2$ NPs on the PC surface (10 mg/mL, immersion speed of 60 mm/min, deposition time of 5 s and withdrawal speed 60 mm/min). The coated plates were dried in air (110 °C), excess CeO$_2$ was removed by washing with ultra-pure MilliQ (QMQ) water, and the plates were dried at 80 °C overnight. Surface coating prevented embedding of CeO$_2$ particles in the PC matrix without having an active surface area for catalytic reactions. It also circumvented the problem of producing stable dispersions from a mixture of CeO$_2$ NPs and organic binders which often result in hazy films[68] due to particle aggregation. The coating with CeO$_2$ NPs was demonstrated by SEM/EDX (Figure 4.5A-B, not annealed, annealed at 185 °C).
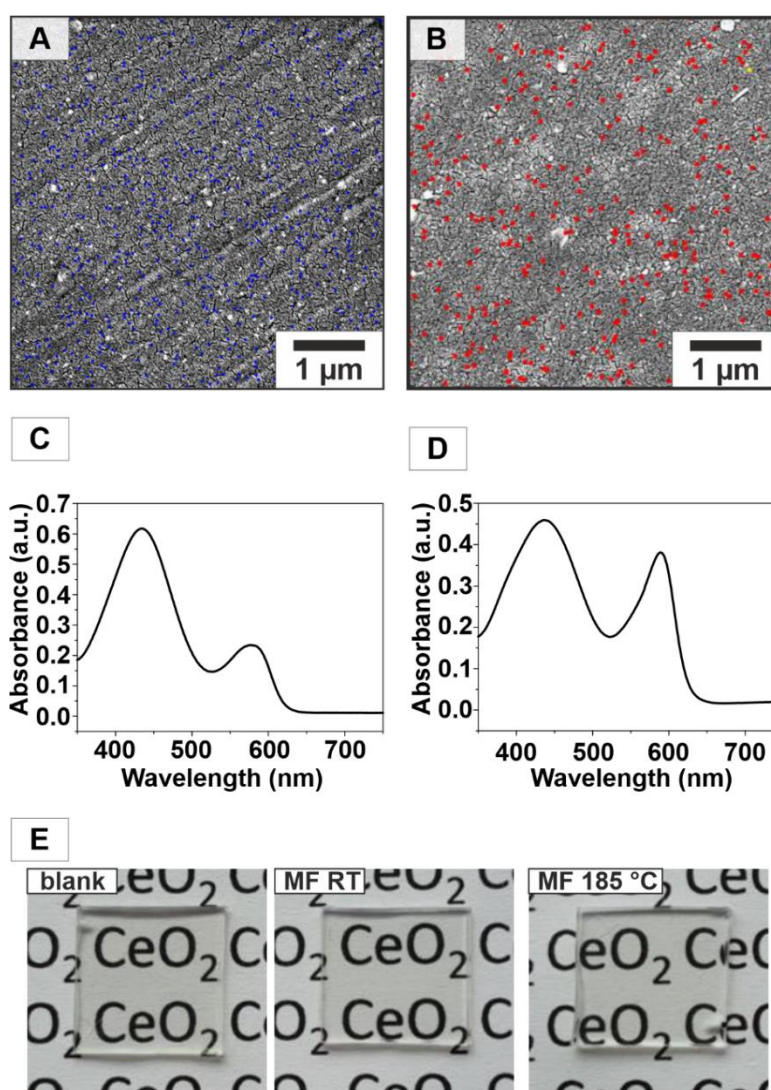
Figure 4.5. CeO$_2$/polycarbonate panels. (A) SEM images of polycarbonate panels with CeO$_2$ NPs from segmented flow synthesis with corresponding (EDX mapping marked as blue dots for Ce). (B) Polycarbonate panels with CeO$_2$ NPs from segmented flow synthesis, annealed at 185 °C (EDX mapping marked as red dots). (C, D) Spectral changes induced by oxidative bromination of PR after 72 h of the CeO$_2$/polycarbonate panels with (C) CeO$_2$ NPs (not annealed) and (D) CeO$_2$ NPs (annealed at 185 °C). (E) Image of a blank polycarbonate panel (left) polycarbonate panels with CeO$_2$ NPs (not annealed/185°C

The binding of the CeO_2 NPs to the surface proved to be successful, as both CeO_2/PC panels showed high catalytic activity (demonstrated by conversion PR to TBPB in the PR assay, Figure 4.5C-D). Importantly, coating of polycarbonate panels with CeO_2 NPs did not lead to any color change. Highly transparent CeO_2/PC sample panels were obtained, which showed no difference in transmission compared to uncoated PC panels (Figure 4.5E; UV-Vis absorption spectra in Figure 4.13 (SI)).

Similar Young's moduli / hardness values were obtained for the CeO_2/PC samples. The Young's moduli for CeO_2/PC with annealed NPs slightly (3.74 GPa $\pm$ 0.06 GPa) increase compared to those of CeO_2/PC with non-annealed NPs (3.73 GPa $\pm$ 0,12 GPa), while the hardness value slightly decreased for the former ones from 274.81 MPa $\pm$ 8.76 MPa (ambient temperature) to 265.80 MPa $\pm$ 9.86 MPa (annealed at 185 °C). These values are much higher than those which were obtained for pure PC 2.32 $\pm$ 0.02 GPa (2.4 GPa ISO 527-1,-2) and 178.77 MPa $\pm$ 2.20 MPa.[69] As expected, the Young's modulus increased with surface-bound CeO_2 content. Comparative hardness values of polystyrene, polypropylene, polyethylene, poly(ethylene terephthalate), and poly(methyl methacrylate) polymer films without NPs coating are typically close to 10 MPa,[70] while the Young's modulus and hardness of pure ceramic CeO_2 coatings prepared by magnetron sputtering are 80.5 $\pm$ 1.3 GPa and 4.1 $\pm$ 0.3 GPa.[71] Although Young´s modulus and scratch resistance are independent parameters, the ratio E/H of Young´s modulus and hardness paralles the ratio of the contact depth over the total penetration.[72] This indicates that CeO_2 coating of PC panels increases the scratch resistance of polycarbonate surfaces.

CeO_2/PC nanocomposites inhibit biofilm formation and affect pyocyanin production in _P. aeruginosa_. CeO_2/PC composites were tested on their potential to inhibit bacterial biofilm formation and on the ability to interfere with bacterial quorum sensing with _P. aeruginosa_, a Gram-negative soil bacterium, recognized for its ubiquity, its antibiotic resistance mechanisms, which is known to contaminate drinking water distribution systems. Furthermore, _P. aeruginosa_ is a potent biofilm producer and therefore widely used as an indicator strain.[73] Additionally, _P. aeruginosa_ is known to be responsible for opportunistic infections in situations with limited barriers, such as skin defects in wounds, or epithelial impairment in advanced stages of chronic pulmonary diseases or cystic fibrosis.[74]

To test biofilm formation on CeO_2 coated PC surfaces, the bacteria were grown for 72 h at 30 °C on different composites placed in 24-well plates. After removing the planktonic cells, the attached bacteria were stained with crystal violet. In comparison to the uncoated PC plate, both nanoparticle composites were able to decrease bacterial biofilm formation (Figure 4.6). However, the CeO_2 particles annealed at 185 °C had with a 65% decrease a much larger effect

on the biofilm formation of *P. aeruginosa* than the untreated CeO$_2$ particles which only showed a 30% decrease. While the biofilm on the untreated PC plate was distributed equally all over the surface, the distribution was inhomogeneous on both CeO$_2$ RT/PC composites and the CeO$_2$ 185 °C/PC nanocomposites (Figure 4.6).
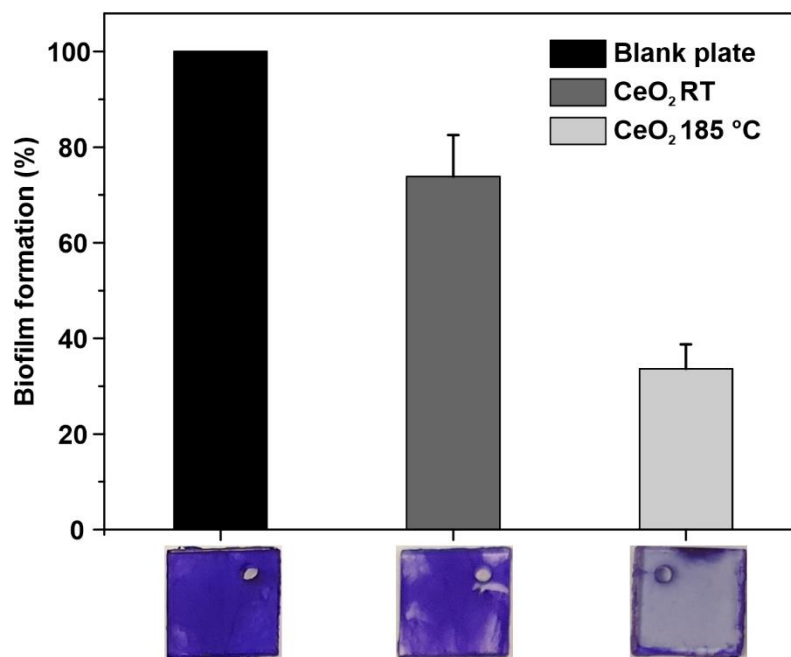

Figure 4.6. Bacterial biofilm formation on CeO$_2$-coated PC surfaces. Crystal violet staining assay of *P. aeruginosa* PA14 grown in LB broth. The bacteria were cultivated aerobically for 72 h under gentle movement (150 rpm) at 30 °C on non-coated (blank plate) and CeO$_2$-coated PC surfaces annealed at 185 °C or not annealed (RT). Then, the planktonic cells were removed, and the attached cells were stained with crystal violet. After solubilization of the bound crystal violet, the quantification was performed via measurement of absorbance in a plate reader at 575 nm. The stained plates are shown at the bottom of the figure. Error bars represent the standard deviation of three independently performed experiments.

Furthermore, we analyzed biofilm formation on CeO$_2$ coated PC surfaces via quantifying single live and dead cells on the surfaces. For that purpose, the *P. aeruginosa* PA14 was grown for 72 h at 30 °C on the different PC samples placed in 24-well plates. After removing the planktonic cells, the attached bacteria were stained with SYTO 9 (total cell count) and propidium iodide (live cell count). In comparison to the blank plate (Figure 4.7A), both CeO$_2$/PC composites showed a decrease in bacterial cell attachment. While the biofilm on the blank plate was equally distributed all over the surface, less biofilm clusters were visible on the CeO$_2$ RT/PC (Figure 4.7B) and much less as well as smaller clusters on the CeO$_2$ 185 °C/PC (Figure 4.7C) composites. Although both nanoparticle composites were able to reduce the bacterial attachment, resulting in a reduced number of cell clusters on the surface, the most promising

87

effect could be achieved with the CeO_2 185 °C/PC composites. In comparison to the blank plate, approximately 60% of the cells were attached to the CeO_2 RT/PC surfaces, and only 15% on the CeO_2 185 °C/PC composites (Figure 4.7D). Furthermore, the composites had no effect on the life/dead cell-ratio, as the portion of dead cells on the treated surfaces were comparable to that on the blank plate (approximately 15%-20%) (Figure 4.7D). These data clearly show the inhibitory and non-biocidal effect of the composites on bacterial biofilm formation. This could be also demonstrated in liquid culture. The addition of CeO_2 to a liquid culture of *P. aeruginosa* PA14 had no effect on the growth of the bacteria at 30°C (Figure 4.7E). Therefore, CeO_2 must interfere with bacterial biofilm formation on another than a toxic way.
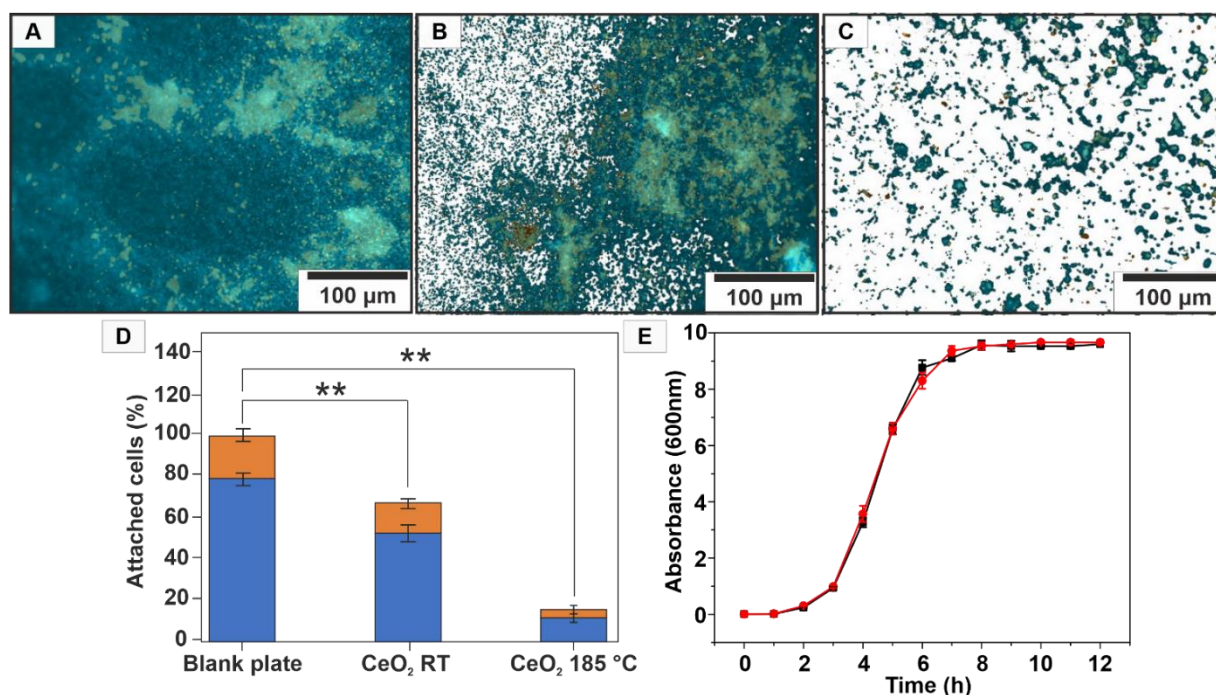
Figure 4.7. Effect of CeO_2-coated PC surfaces on cell adhesion and growth of *P. aeruginosa* PA14. The bacteria were cultivated for 72 h under gentle shaking (150 rpm) at 30 °C on non-coated and coated CeO_2/PC composites. The planktonic cells were removed, and the remaining bacteria attached to the surfaces were stained with SYTO 9 and propidium iodide for 30 minutes at 30 °C. The surfaces were then analysed by epifluoresence surface microscopy. The pictures show bacterial attachment on (A) non-coated , on (B) CeO_2 RT/PC and (C) CeO_2 185 °C/PC composites. The effect of the incorporated CeO_2 NPs on bacterial biofilm formation was quantified by analyzing three different squares of 300 μm x 400 μm in size by quantifying the portion of green (SYTO 9) and red fluorescence color (propidium iodide) representing (D) total and live cells (blue) count and respectively dead cells (orange). The asterisks (**) indicate statistically significant differences with a *p*-value smaller than 0,001. (E) Growth curve of *P. aeruginosa* with (black) and without (turquoise) addition of 2% (w/v) CeO_2. Error bars represent standard deviation of three independently performed experiments.

For the organization within a biofilm, bacteria usually have to communicate via small diffusible molecules sensing their cell count, a process called quorum sensing.[75] The CeO_2 NPs promote the production of halogenated compounds, which are similar to quorum sensing molecules of

88

Gram-negative bacteria. Therefore, we assumed that the non-toxic biofilm inhibiting effect of CeO$_2$ composites might be due to a putative interference with the bacterial cell-cell communication, an effect that is generally referred to as quorum quenching.[76]
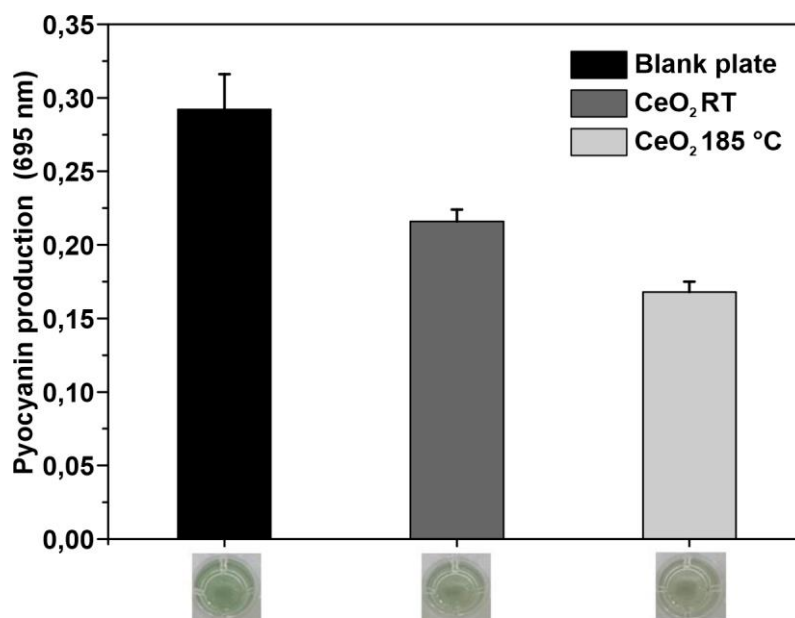

Figure 4.8. Effect of CeO$_2$/PC nanocomposites on the pyocyanin production in *P. aeruginosa* PA14. The bacteria were cultivated for 72 h under shaking conditions (350 rpm) at 37 °C on non-coated and coated PC plates. The plates were then removed, and the remaining culture fluid was analyzed for pyocyanin occurrence in a plate reader at 695 nm. Error bars represent standard deviation of three independently performed experiments.

In order to get first evidence on the molecular mechanism of how CeO$_2$/PC inhibit bacteria biofilm formation, we analysed its effect on the production of the virulence factor pyocyanin in *P. aeruginosa* PA14. Besides biofilm formation, the biosynthesis of pyocyanin is also under control of the entire quorum sensing systems in these bacteria [77]. For that purpose, the bacteria were cultivated for 72 h at 37 °C on blank plates and on CeO$_2$/PC composites. Then, the PC plates were removed, and the remaining culture fluid was analyzed on the presence of pyocyanin as described under *Materials and methods*. Both nanocomposites had a negative effect on pyocyanin production (Figure 4.8). However, CeO$_2$/PC composite annealed at 185 °C showed the highest decrease of up to 55% compared to the control cultures. Since *P. aeruginosa* is known to communicate via a distinct cell-cell signaling scheme,[78] it can be assumed that the NPs act on at least one of the three known quorum sensing systems. The results regarding inhibition of biofilm formation and pyocyanin production in *P. aeruginosa* finally showed the applicability of CeO$_2$/PC nanocomposites to inhibit bacterial communication and therefore

bacterial biofilm formation as a non-toxic strategy. Optimal growth conditions for *P. aeruginosa* are a pH-value range of 6 – 7.5 and a temperature of 30 °C.[79] Our tests were done in this pH and temperature window. Therefore, a change of the pH-value or temperature would in generally decrease the growth rate of the bacterium rather than the antibacterial performance.

4.4. Conclusion

CeO_2 NPs were coated on polymer surfaces to fabricate highly transparent and hard polymer/nanoparticle composites, which display the intrinsic haloperoxidase-like characteristics of the CeO_2 NPs as demonstrated by the bromination of PR and the formation of the virulence factor pyocyanin, which is regulated by the quorum sensing system. Since *P. aeruginosa* is known to communicate *via* a distinct cell-cell signaling scheme, it can be assumed that the biomimetic activity of the CeO_2 NPs acts on at least one of the three known quorum sensing systems. An effective segmented flow synthesis of CeO_2 NPs was devised. It allows the continuous synthesis of non-agglomerated material with a single mixer to fabricate nanomaterials for polycarbonate displays in large quantities. The yield can easily be enhanced by parallelization. The highly reproducible (automated) synthesis of CeO_2 NPs in copious amounts allowed to systematically analyze the role of particle size, ion concentration and surface chemistry on their (bio)catalytic properties.

An important point is that ceria does not leach because of its extremely low solubility (solubility product log K_L = −60).[80,81] This is also the reason why cerium – despite its abundance (comparable to copper)[82]– is involved in biological processes only under extreme conditions in volcanic mudpots.[83] The low solubility makes ceria nanoparticles also highly biocompatible: little or no cytotoxic effects were observed (depending on the uptake pathway).[84] Ceria nanoparticles have been proposed for biomedical applications (e.g. in sun creams),[54]and it was demonstrated with *in vivo* experiments that ceria NPs can even protect cells against irradiation and oxidative stress.[55,85]

In contrast, various metal NPs (e.g., Cu or Ag) preventing biofouling are known to be harmful to the environment. [86] V_2O_5 NPs showed excellent performance to prevent biofouling on surfaces in marine environments,[43] but leaching leading to soluble polyvanadates in combination with reported carcinogenic and mutagenic effects make any practical application unlikely.[87-90]

TiO_2 nanoparticles show antibiofouling properties, but their mode of biocidal activity TiO_2 is associated with the induction of oxidative stress due to photogenerated reactive oxygen species under UV irradiation. The production costs of TiO_2 dispersible nanoparticles are moderate.[10,91] TiO_2 particles can be incorporated into various polymers, such as polyamide[10] poly(lactic-co-glycolic acid)[92] or polytetrafluorethylene[93] with antibiofouling properties. Titania nanoparticles have a broad activity spectrum against microorganisms, and they have been considered environmentally friendly with non-contact biocidal action.[94] Their recent classification as a "suspected carcinogen" by the EU, however, may lead to restrictions or even a ban on their chemical use in consumer products.[95] CeO_2 offers a sustainable alternative to TiO_2, with non-toxic properties and high abundance, more importantly catalytic activity does not depend on UV irradiation.

Because of their non-toxicity and environmental sustainability polycarbonate/CeO_2 nanocomposites may find broad application as green antimicrobials on plastics for automotive, aircraft, or railway components, for drinking bottles, glasses and food containers, where traditional biocides (toxines, antibiotics, etc.) are strictly prohibited because of toxicity, non-target impacts or the evolution of resistance by micro-organisms. Other applications could be touch panels, sporting helmets, glasses, fountain pens, portable devices for consumer electronics like smart phones, audio player cases, computer cases, durable, lightweight luggage, musical instruments, and toys. Especially in the health sector this may prevent infections that are becoming increasingly troublesome with the emergence of drug resistant bacteria and reduce the use of antibiotics.

4.5. Experimental Section

Materials. $Ce(ac)_3 \cdot H_2O$ (99,9% Sigma Aldrich), oleylamine (> 50% TCI Chemicals), benzyl alcohol (99% Acros Organics), deionized water, cyclohexane (99,8% Fisher Scientific), ethanol (98% Honeywell), H_2O_2 (35% Roth), fluorinated ethylene propylene tube with 1/16´´ OD and 1 mm ID (Fisher Scientific), peristaltic pump reglo ICC (Ismatec), Polycarbonate (thickness 1 mm, Goodfellow)

Batch Synthesis. Before the synthesis $Ce(ac)_3 \cdot H_2O$ was dried for 10 minutes at 130 °C in an oven. Subsequently 0.5 mmol (150 mg) of dried $Ce(ac)_3$ was transferred into a 100 mL three-necked flask, furthermore 7 mL of benzyl alcohol and 3 ml of oleylamine were added. The solution was heated up to 120 °C (5 °C/min) and kept at the temperature for 20 minutes. Then

it was heated up to 180 °C (5 °C/min) for 30 minutes with a stirring speed of 400 rpm. The reaction solution was subsequently cooled down to room temperature. For the purification the product was washed three times with ethanol and cyclohexane and dried under vacuum at room temperature.

Segmented Flow Synthesis. Before the synthesis $Ce(ac)_3 \cdot H_2O$ was dried for 10 minutes at 130 °C in an oven. Subsequently, 1.4 mmol of dried $Ce(ac)_3$ was transferred into a beaker, 21 mL of benzyl alcohol and 9 mL of oleylamine were added, and the solution was stirred at room temperature. Deionized water was added in a second beaker. The overall tube length was 9 m. The first segment (3 m) was put in an oil bath with a temperature of 120 °C, the second segment (3 m) was heated in an oil bath to 180 °C, the last segment (3 m) was kept at room temperature. The two solutions were pumped separately, the flow rate for the metal precursor solution was 2 mL/min, the flow rate for the deionized water was 1.5 mL/min. The two solutions were connected through a T-fitting. The nanoparticles were washed three times with ethanol and cylclohexane and dried under vacuum at room temperature. The reaction mixture was also scaled up to the tenfold and even twentyfold of the amount of the original batch synthesis.

Powder X-ray Diffraction. X-ray diffraction patterns were recorded on a STOE Stadi P diffractometer equipped with a Dectris Mython 1k detector in transmission mode using Mo $K\alpha_1$ radiation. Crystalline phases were identified according to the PDF–2 database using Bruker AXS EVA 10.0 software. Full pattern profile fits (Pawley / Rietveld) were performed with TOPAS Academic 6.0 applying the fundamental parameter approach. [76,77]

Transmission Electron Microscopy. Transmission Electron Microscopy (TEM) images for determining the size and morphology were acquired on a FEI Tecnai G2 Spirit microscope operating at 120 kV (LaB_6 filament), equipped with a Gatan US1000 CCD-camera (16-bit, 2048×2048 pixels), using the Gatan Digital Micrograph software. Samples for TEM were prepared by placing one drop (10 µL) of a diluted NP solution in chloroform (0.1 mg mL^{-1}) on a carbon-coated copper grid and by letting it dry at room temperature. Size evaluation of individual nanoparticles on the TEM images was performed with ImageJ.

High Resolution Transmission electron microscopy. The Samples were prepared adding a drop of diluted Nanoparticles in Cylcohexan on a carbon coated copper grid. The samples were measured with the FEI Tecnai F30 ST TEM at 300 kV acceleration voltage equipped with a Gatan US4000 4k CCD camera.

Scanning Electron Microscopy. Scanning Electron Microscopy (SEM) images for demonstrating the presence of CeO2 on the surface of PC were acquired on a FEI Nova

NanoSEM with a EDX-detector (EDAX-Pegasus X4M). The samples were coated with gold before investigation and observed at 15 kV.

IR Spectroscopy. ATR-IR spectra were measured on a Nicolet iS10 Spectrometer manufactured by Thermo Scientific. The spectra were recorded in a frequency range from 650 cm^{-1} to 4000 cm^{-1} with a resolution of 1.4 cm^{-1} per data point.

Thermogravimetry (TGA). The measurements were conducted using a Perkin Elmer TGA Pyris 6 (30 to 800 °C, heating rate of 5 °C·min^{-1}, oxygen atmosphere, the sample weight was about 10 mg).

Brunauer-Emmet-Teller (BET). The specific surface area was determined using a *3P micro 300 adsorption-desorption device from 3P instruments*. Measurements were conducted with an appropriate amount of sample (150 mg) at 77 K with nitrogen as analysis gas.

Preparation of CeO$_2$/Polycarbonate Nanocomposites. Polycarbonate (PC) plates (ca. 1x1 cm) were washed with MQ-water and ultrasonicated for 10 min in isopropanol to remove contaminants. After that, PC plates were dried in air at 80 °C overnight. PC substrates were exposed to oxygen plasma for 20 min to produce hydroxyl groups onto the surface. The oxygen plasma was created at a pressure = 0,1 mbar and a power = 300 W. The pretreated PC plates were dip coated in a CeO$_2$ dispersion (10 mg/mL) in cyclohexane with a dipping speed of 60 mm/min, deposition time of 5 s, and withdrawal speed of 60 mm/min. After dip coating, the coatings were dried in air at 110 °C for 16 h. Finally, CeO$_2$-coated PC substrates were washed with MQ-water to remove excess CeO$_2$ from the surface and dried at 80 °C overnight.

Nanoindentation Young's modulus and hardness were measured by nanoindentation using a MFP Nanoindenter (Asylum Research, Santa Barbara, CA) equipped with a diamond Berkovich indenter. Each series of indentations was done on a grid of 2×6 indents on a 90×90 µm^2 area at three different positions on the sample, i.e., 36 indents per series. The Young's moduli and hardness were calculated by fitting the indentation curves according to the Oliver-Pharr method[96] using the analysis software of the nanoindenter. The Young's modulus was obtained as *elastic* response of the sample upon unloading, i.e., from the slope of the onset of the unloading curve. The hardness of the material was obtained as the ratio of maximum applied load divided by the indenter contact area at that load. It is indicative of the resistance of the material against *plastic* deformation.

Contact Angle Measurements. The contact angle was measured with the contact angle measurement system OCA35 and the water drop was deposited by a Hamilton syringe (100 µL) with a hydrophobic needle.

HPO Activity Measurements. The activity measurements were performed with the phenol red assay. Phenol red (PR) is converted to tetrabromophenol blue (TBPB) in the presence of a bromide source (KBr), H_2O_2 and CeO_2 NPs dispersed in MilliQ water. The kinetic measurements were carried out on a Varian Cary 5G UV/Vis spectrometer in the wavelength range from 300 nm to 750 nm. For the measurements, CeO_2 NPs (25 µg/mL) were dispersed in MilliQ water (18.2 MΩ cm^{-1}), and H_2O_2 (300 µM), PR (50 µM), and KBr (25 mM) were added to the solution. The solution was stirred for 2 minutes after the addition of PR to obtain a homogenous solution. The baseline was measured with a mixture of NPs, KBr and PR dissolved in MilliQ water. H_2O_2 was added prior to the measurement.

Michaelis Menten kinetics. The Michaelis Menten kinetics were measured by adding different amounts H_2O_2 to a stirred solution of PR, KBr and the NPs. For this, standard solutions of KBr (250 mM) and PR (1 mM) were prepared separately by dissolving the appropriate amount in MQ-water under sonication. As next step a mixed standard solution of PR with KBr was prepared by dilution of the standard solutions. The final solution contained 50 µM PR and 25 mM KBr. From this solution 2 mL were mixed in a 2.5 mL quartz cuvette with 62.5 µL of a nanoparticle dispersion (1 mg/mL). The amount of H_2O_2 was introduced by adding always the same amount (50 µL) of an appropriate H_2O_2 dilution. For this purpose, a 100 mM H_2O_2 standard solution was prepared as a starting solution and the dilution was done immediately before the addition. Dilution was achieved by mixing MQ-water with the H_2O_2 initial solution (e.g. 95:5 v/v (water/H_2O_2(100 mM)) for a 5 mM H_2O_2) to prepare the diluted H_2O_2 solution. All kinetics were run for a reaction time of 6 min. The absorbance change was measured at a wavelength of $\lambda = 590$ nm. All data points were fitted linearly in an interval of 2-5 min, to achieve a linear relation between the data. The amount of TBPB was calculated from the Lambert-Beer law. The extinction coefficient was determined by measuring five TBPB solutions containing different amounts of dye (range c(dye) = 0.002 – 0.018 mM) in a quartz cuvette (d = 1 cm) to fit into the range of $0.1 < A_{590} < 1$. An extinction coefficient of 47111 L mol^{-1} cm^{-1} was determined for pure TBPB in water measured with a Varian Cary 5G spectrophotometer.

Bacterial strains and growth conditions. P. aeruginosa PA14 was used for biofilm and growth assays, which is a clinical isolate with increased virulence compared to the reference laboratory strain PAO1 and is resistant against a large number of antibiotics)[97] *P. aeruginosa* was aerobically cultivated in LB medium (1% (w/v) NaCl; 1% (w/v) tryptone; 0.5% (w/v) yeast extract) at 30 °C. For preparation of agar plates, 1.5% (w/v) agar was added to the medium. For monitoring growth curves *P. aeruginosa* PA14 cultures were grown overnight at 30 °C in LB

medium. Overnight cultures were washed with sterile 0,85 % NaCl (w/v) solution to remove residual media. Cultures were diluted in fresh LB medium to obtain equal optical densities (OD_{600}) of 0,005. Growth of the cultures was assessed in LB broth in presence and absence of 2% CeO_2 NP´s (w/v). Growth was monitored by determining absorbance at 600 nm using Ultrospec 2100 pro UV/Vis Spectrometer (Biochrom, Berlin, Germany) cuvette reader for 12 h at 30 °C. All experiments were performed in triplicate.

Biofilm assays. For quantification of bacterial biofilm production, a modified method of previous published protocols was used .[98] Briefly, *P. aeruginosa* was aerobically cultivated in LB medium over night at 30 °C. The cultures were then diluted in LB in a volume of 1 ml per well of a 24-well polystyrene microtiter plate (Sarstedt, Nürnbrecht) at a final Optical Density at 600 nm (OD_{600}) of 0.5. Additionally, KBr (Roth, Karlsruhe, Germany) and H_2O_2 (Roth, Karlsruhe, Germany) at a final concentration of 32 mM and 0.8 mM, respectively, were added to the wells. Then, the blank plates and CeO_2/PC composites were subjected. Subsequently, the microtiter plate was incubated for 72 h under gentle shaking (150 rpm) at 30 °C. H_2O_2 was added stepwise at a final concentration of 0.8 mM every 24 h. Then, the plates were rinsed with water to remove the planktonic cells. After drying for 5 min, 1 ml of 1% (w/v) crystal violet (Merck, Darmstadt) was added to the wells containing the plates. After 30 min incubation at room temperature, unbound crystal violet was removed by gently submerging the plates for two times in water. The plate was then air-dried over-night at room temperature. For quantification, 1 ml of 30% (v/v) acetic acid (Roth, Karlsruhe) was added to the plates to solubilize the crystal violet from the biofilm. After 15 min of incubation at room temperature, absorbance was quantified in a plate reader (Tecan, Salzburg) at 575 nm.

Pyocyanin Analyses. For pyocyanin production, an alternate method of already published protocols were used.[96] *P. aeruginosa* was cultivated in LB medium over night at 30 °C. The cultures were then diluted in LB, in a volume of 1 ml per well of a 24-well polystyrene microtiter plate (Sarstedt, Nürnbrecht) at a final OD_{600} of 0.5. Additionally, KBr (Roth, Karlsruhe, Germany) and H_2O_2 (Roth, Karlsruhe, Germany) at a final concentration of 32 mM and 0.8 mM respectively were added to the wells. The non-coated plates and CeO_2/PC composites were then added to the wells, respectively. The microtiter plate was then incubated for 72 h under shaking conditions (350 rpm) at 37 °C. Every 24 h H_2O_2 was added at a final concentration of 0.8 mM. Afterwards, the composites were taken out of the wells and the remaining supernatant inside the wells was collected in a microreaction tube (Eppendorf, Germany). Cells were separated from culture fluids via centrifugation at 16×1000 g for 15

min. Then, the supernatant was passed through 0.22 μm filters (Merck, Darmstadt). Cell-free culture fluids were then analysed for pyocyanin in a plate reader (Tecan, Salzburg) at 695 nm.

Epifluorescence microscopy and fluorescence quantification. P. aeruginosa PA14 was cultivated in LB medium over night at 30 °C. The cultures were then diluted in LB, in a volume of 1 ml per well of a 24-well polystyrene microtiter plate (Sarstedt, Nürnbrecht) at a final OD_{600} of 0.5. Additionally, KBr (Roth, Karlsruhe, Germany) and H_2O_2 (Roth, Karlsruhe, Germany) at a final concentration of 32 mM and 0.8 mM, respectively, were added to the wells. The non-coated blank plates and nanoparticle composites were then added to the wells. The microtiter plate was then incubated for 72 h under gentle shaking (150 rpm) at 30 °C. Every 24 h H_2O_2 was added at a final concentration of 0.8 mM. Then, the plates were rinsed with water to remove the planktonic cells. Afterwards, the plates were placed in 1 ml of a combined SYTO 9 and propidium iodide solution (Thermo Fisher, Pittsburgh, USA) and incubated for 30 minutes at 30 °C. Then, the plates were rinsed again with water and mounted on microscopy slides. Biofilm samples were microscopically analysed on an Axio Imager 2 fluorescence microscope, which is especially designed for material surface analysis (Carl Zeiss, Jena, Germany). The fluorophore SYTO 9 was visualized with an excitation of 470 nm while propidium iodide was visualized with an excitation of 558 nm. The images were then processed using the ZEN 3.3 blue software. The green and red fluorescence intensity within single squares were was then quantified and set into correlation using ImageJ software (Version: 2.0.0-rc-69/1.52n).

4.6. References

(1)   H. C. Flemming, J. Wingender, U. Szewzyk, P. Steinberg, S. A. Rice, S. Kjelleberg, *Nat. Rev. Microbiol.* **2016**, *14*, 563-575.

(2)   S. T. Kelley, U. Theisen, L. T. Angenent, A. S. Amand, N. R. Pace, *Appl. Environ. Microbiol.* **2004**, *70*, 4187–4192.

(3)   A. Różańska, A. Chmielarczyk, D. Romaniszyn, M. Bulanda, M. Walkowicz, P. Osuch, T. Knych, *Antimicrob. Resist. Infect. Control* **2017**, *6*, 80.

(4)   F. Siedenbiedel, J. C. Tiller, *Polymers* **2012**, *4*, 46-71.

(5)   Z. K. Zander, M. L. Becker, *ACS Macro Lett.* **2018**, *7*, 16-25.

(6)   S. Jiang, Z. Cao, *Adv. Mater.* **2010**, *22*, 920-932.

(7)   S. Krishnan, C. J. Weinman, C. K. Ober, *J. Mater. Chem.* **2008**, *18*, 3405-3413.

(8)   I. Banerjee, R. C. R. C. Pangule, R. S. Kane, *Adv. Mater.* **2011**, *23*, 690-718.

(9)   G. D. Bixler, B. Bushan, *Phil. Trans. R. Soc. A* **2012**, *370*, 2381–2417.

(10)   B. Khorshidi, I. Biswas, T. Ghosh, T. Thundat, M. Sadrzadeh, *Sci. Rep.* **2018**, *8*, 784.

(11)   J. Genzer, K. Efimenko, *Biofouling* **2006**, *22*, 339−360.

(12)   N. Gao, F. Geyer, D. W. Pilat, S. Wooh, D. Vollmer, H.-J. Butt, R. Berger, *Nat. Phys.* **2017,** *13*, 1020-1025.

(13)   M. Manefield, R. de Nys, K. Naresh, R. Roger, M. Givskov, S. Peter, S. Kjelleberg, *Microbiolog*y **1999**, *145,* 283-291.

(14)   A. Camilli, B. L. Bassler, *Science* **2006**, *311*, 1113-1116.

(15)   W. R. J. D. Galloway, J. T. Hodgkinson, S. D. Bowden, M. Welch, D. R. Spring, *Chem. Rev.* **2011**, *111,* 28-67.

(16)   B. L. Bassler, R. Losick, *Cell* **2006**, *125*, 237-246.

(17)   A. Butler, M. Sandy, *Nature* **2009**, *460*, 848-854.

(18)   R. Wever, M. A. van der Horst, *Dalton Trans.* **2013**, *42*, 11778-11786.

(19)   V. Weichold, D. Milbredt, K.-H. van Pée, *Angew. Chem. Int. Ed.* **2016**, *55*, 6374-6389.

(20)   V. Agarwal, Z. D. Miles, J. M. Winter, A. S. Eustáquio, A. A. El Gamal, B. S. Moore, *Chem. Rev.* **2017**, *117*, 5619-5674.

(21)   B. Sels, B. DeVos, M. Buntinx, F. Pierard, A. Kirsch-De Mesmaeker, P. Jacobs, *Nature* **1999**, *400*, 855–857.

(22)   G. J. Colpas, B. J. Hamstra, J. W. Kampf, V. L. Pecoraro, *J. Am. Chem. Soc.* **1996**, *118*, 3469-3478.

(23)   V. Conte, B. Floris, *Dalton Trans.* **2011**, *40*, 1419–1436.

(24)   N. Madaan, N. R. Shiju, G. Rothenberg, *Catal. Sci. Technol.* **2016**, *6*, 125–133.

(25)   F. Natalio, R. André, A. F. Hartog, B. Stoll, K. P. Jochum, R. Wever, W. Tremel, *Nat. Nanotechnol.* **2012**, *7*, 530-535.

(26)   K. Herget, P. Hubach, S. Pusch, P. Deglmann, H. Götz, T. E. Gorelik, I. A. Gural'skiy, F. Pfitzner, T. Link, S. Schenk, M. Panthöfer, V. Ksenofontov, U. Kolb, T. Opatz, R. André, W. Tremel, *Adv. Mater.* **2017**, *29*, 1603823.

(27)   J. Wu, X. Wang, Q. Wang, Z. Lou, S. Li, L. Qin, H. Wei, *Chem. Soc. Rev.* **2019**, *48*, 1004-1076.

(28)   L. Gao, J. Zhuang, L. Nie, J. Zhang, Y. Zhang, N. Gu, T. Wang, J. Feng, D. Yang, S,. Perrett, X. Yan, *Nat. Nanotechnol.* **2007**, *2*, 577-583.

(29)   H. Wei, E. Wang, *Chem. Rev.* **2013**, 42, 6060-6093.

(30)   K. Korschelt, M. N. Tahir, W. Tremel, *Chem. Eur. J.* **2018***, 24,* 9703–9713.

(31)   Nanozymology - Connecting Biology and Nanotechnology, X. Yan (Ed.), Springer Singapore 2020.

(32)   K. Herget, H. Frerichs, F. Pfitzner, M. N. Tahir, W. Tremel, *Adv. Mater.* **2018**, *30*, 1707073.

(33)   D. Price, P. J. C. Worsfold, R. F. Mantoura, *TrAC Trends in Analytical Chemistry* **1992**, *11*, 379-384.

(34)   B. Halliwell, M. V. Clement, L. H. Long, *FEBS Letters* **2000**, *486*, 10-13.

(35)   M. R. Detty, R. Ciriminna, F. V. Bright, M. Pagliario, *Acc. Chem. Res.* **2014,** *47*, 678-687.

(36)   S. Chernousova, M. Epple, *Angew. Chem. Int. Ed.* **2013**, *52*, 1636-1653.

(37)   F. R. Cassee, E. C. van Balen, C. Singh, D. Green, H. Muijser, J. Weinstein, K. Dreher, *Crit. Rev. Toxicol.* **2011**, *41*, 213–229.

(38)   C. K. Kim, T. Kim, I.-Y. Choi, M. Soh, D. Kim, Y.-J. Kim, H. Jang, H.-S. Yang, J. Y. Kim, H.-K. Park, S. P. Park, S. Park, T. Yu, B.-W. Yoon, S.-H. Lee, T. Hyeon, *Angew. Chem. Int. Ed.* **2012**, *51*, 11039-11043.

(39)   B. Collin, M. Auffan, A. C. Johnson, I. Kaur, A. A. Keller, A. Lazareva, J. R. Lead, X. Ma, R. C. Merrifield, C. Svendsen, J. C. White, J. M. Unrine, *Environ. Sci. Nano* **2014**, *1,* 533-548.

(40)   R. I. Walton, *Prog. Cryst. Growth Charact. Mater.* **2011**, *57*, 93-108.

(41)   D. Zhang, X. Du, L. Shi, R. Gao *Dalton Trans.* **2012**, *41*, 14455-14475.

(42)   S. Yang, L. Gao, *J. Am. Chem. Soc.* **2006**, *128*, 9330-9331.

(43)   L. Yan, R. Yu, J. Chen, X. Xing, *Cryst. Growth Des.* **2008**, *8*, 1474-1477.

(44)   W. Wang, J. Y. Howe, Y. Li, X. Qiu, D. C. Joy, M. P. Paranthaman, M. J. Doktyczde, B. Gu, *J. Mater. Chem.* **2010**, *20*, 7776-7781.

(45)   C. Slostowski, S. Marre, O. Babot, T. Toupance, C. Aymonier, *Langmuir* **2014**, *30*, 5965−5972.

(46)   T. Adschiri, K. Kanazawa, K. Arai, *J. Am. Ceram. Soc.* **1992**, *75*, 1019-1022.

(47)   A. Cabanas, J. A. Darr, E. Lester, M. Poliakoff, *J. Mater. Chem.* **2001**, *11*, 561-568.

(48)   C. Tyrsted, K. M. Ørnsbjerg Jensen, E. D. Bøjesen, N. Lock, M. Christensen, S. J. L. Billinge, B. B. Iversen, *Angew. Chem. Int. Ed.* **2012**, *51*, 9030 –9033.

(49)   C. Tyrsted, J. Becker, P. Hald, M. Bremholm, J. S. Pedersen, J. Chevallier, Y. Cerenius, S. B. Iversen, B. B. Iversen, *Chem. Mater.* **2010**, *22*, 1814–1820.

(50)   P. W. Dunne, A. S. Munn, C. L. Starkey, T. A. Huddle, E. H. Lester, *Phil. Trans. R. Soc. A* **2015**, *373*, 20150015.

(51)   M. Niederberger, *Acc. Chem. Res.* **2006,** *40*, 793-800.

(52)   G. Garnweitner, M. Niederberger, *J. Mater. Chem.* **2007**, *18*, 1171-1182.

(53)   D. P. Debecker, P. H. Mutin, *Chem. Soc. Rev.* **2012**, 41, 3624-3650.

(54)   C. Tang, Y. Bando, B. Liu, D. Golberg, *Adv. Mater.* **2005**, *17*, 3005-3009.

(55)   H. L. Lin, C. Y. Wu, R. K. Chiang, *J. Colloid Interface Sci.* **2010**, *341*, 12-17.

(56)   S. Mourdikoudis, M. Liz-Marzán, *Chem. Mater.* **2013**, *25*, 1465-1476.

(57)   R. H. Harris, P. M. Shumbula, H. v. d. Walt, *Langmuir* **2015**, *31*, 3934-3943.

(58)   M. Sarif, J. Hilgert, I. Khan, S. Plana-Ruiz, M. Panthöfer, U. Kolb, M. N. Tahir, W. Tremel*, Langmuir* **2020***, 36,* 13804−13816.

(59)   A. A. Coelho, TOPAS Academic V 6.0. Coelho Software, Brisbane, 2016.

(60)   R. W. Cheary, A. A. Coelho, *J. Appl. Crystallogr.* **1992**, *25*, 109-121.

(61)   C. Li, Y. Sakata, T. Arai, K. Domen, K. Maruya, T. Onishi, *J. Chem. Soc., Faraday Trans.* **1989**, *85*, 1451-1461.

(62)   G. N. Vayssilov, M. Mihaylov, P. S. Petkov, K. I. Hadjiivanov, K. M. Neyman, *J. Phys Chem. C* **2011**, *115*, 23435-23454.

(63)   K. Yoshikawa, H. Sato, M. Kaneeda, J. N. Kondo, *J. CO2 Util.* **2014**, *8*, 34-38.

(64)   L. G. Appel, J. G. Eon, M. Schmal, *Catal. Lett.* **1998**, *56*, 199-202.

(65)   T. Montini, M. Michele, M. Monai, P. Fornasiero, *Chem. Rev.* **2016**, *116*, 5987-6041.

(66)   S. Kozuch, J. M. L. Martin, *Catal.* **2012**, *2*, 2787-2794.

(67)   T. G. Shikova, A. A. Ovtsyn, S. A. Smirnov, *High Ener. Chem.* **2019**, *53*, 326-330.

(68)   S. Bardage, M. Hendricksson, S. Olsson, I. P. Collins, D. Meng, A. Ahniyaz, E.-J. Salazar-Sandoval, A. Rahier, M. Gasparini, N. Lamproye, *Surf. Coat. Int.* **2013**, *96*, 94-99.

(69)   Young´s   modulus   polycarbonate: https://omnexus.specialchem.com/polymer-properties/properties/young-modulus#values

(70)   E. Baur, T.A. Osswald, N. Rudolph, Plastics Handbook, Carl Hanser, München, 2018.

(71)   Z. Shi, P. Shum, Z. Zhou, L. K.-Y. Li, *Surf. Coat. Tech*. **2017**, *320*, 333–338.

(72)   V. Jardret, H. Zahouani, J. L. Loubet, T. G. Mathia, *Wear.* **1998**, *218*, 8-14.

(73)   K. D. Mena, C. P. Gerba, *Rev. Environ. Contam. Tox.* **2009**, *201*, 71-115.

(74)   M. Paulsson, Y.C. Su, T. Ringwood, F. Udden, K. Riesbeck, *Sci. Rep*. **2019**, *9*, 18168.

(75)   C. M. Waters, B. M. Bassler, *Ann. Rev. Cell Dev. Biol.* **2005,** *21***,** 319-346**.**

(76)   C. Grandclement, M. Tannieres, S. Morera, Y. Dessaux, D. Faure, *FEMS Microbiol Rev.* **2016**, *40,* 86-116.

(77)   O. Karatuna, A. Yagci, *Clin. Microbiol. Infect.* **2010**, *16*, 1770-1775.

(78)   K. E. R. Bachta, J. P. Allen, B. H. Cheung, C. H. Chiu, A. R. Hauser, *Nature Commun.* **2020**, *11*, 543.

(79)   A. Tsuji, Y. Kaneko, K. Takahashi, *Microbiol. Immunol.* **2002**, *26*, 15-24.

(80)   E. Curti, C. Degueldre, *Radiochim. Acta* **2002**, *90*, 801-804.

(81)   T. V. Plakhova, A. Y. Romanchuk, S. N. Yakunin, T. Dumas, S. Demir, S. Wang, S. G. Minasian, D. K. Shuh, T. Tyliszczak. A. A: Shiryaev, A. V. Egorov, V. K. Ivanov, S. N. Kalmykov, *J. Phys. Chem. C* **2016**, *120*, 22615-22626.

(82)   N. N. Greenwood, A. Earnshaw, Chemistry of the Elements, Pergamon, 1984, p 1284.

(83)   A. Pol, T. R. M. Barends, A. Dietl, A. F: Khadem, J. Eygensteyn, M. S. M. Jetten, H. J. M. Op den Camp, *Environ Microbiol.* **2014,** *16*, 255-264.

(84)   J. Gagnon, K. M. Fromm, *Eur. J. Inorg. Chem.* **2015**, *27*, 4510-4517.

(85)   D. Kim, H. J. Kwon, T. Hyeon, *Adv. Mater.* **2019**, *31*, 1807965.

(86)   J. Zhang, W. Guo, Q. Li, Z. Wan, S. Liu, *Environ. Sci. Nano*, **2018**, *5*, 2482–2499.

(87)   F. L. Assem, L. S. Levy, *J. Toxicol. Environ. Health, Part B*, **2009**, *12*, 289–306.

(88)   Vanadium: The Versatile Metal, ed. K. Kustin, J. C. Pessoa, D. C. Crans, ACS Symposium Series, American Chemical Society, Washington DC, 2007, vol. 974.

(89)   M. R. Tavakoli, D. B. Dreisinger, *Hydrometallurgy*, **2014**, *141*, 59–66.

(90)   M. Trypuć, U. Kiełkowska, M. Chałat, *J. Chem. Eng. Data*, **2002**, *47*, 765–767.

(91)   M. R. Tavakoli, D. B. Dreisinger, *Hydrometallurgy* **2014**, *141*, 59–66.

(92)   C. S. Ong, P. S. Goh, W. J. Lau, N. Misdan, A. F. Ismail, *Desalination*, **2016**, *393*, 2.

100

4. A Simple Microfluidic Benchtop System for High-Throughput Synthesis of CeO₂
Nanoparticles in Segmented Flow for Highly Transparent Nanocomposites Repelling
Pseudomonas aeruginosa PA14 Biofilms

(93) J. Y. Wu, C. W. Li, C. H. Tsai, C. W. Chou, D. R. Chen, G. J. Wang, *Nanomed.: Nanotechn., Bio. And Med.* **2014**, 1097-1107.

(94) S. Zhang, X. Liang, G. M. Gadd, Q: Zhao, *Applied Surface Sci.* **2019**, 231-241.

(95) P.-L. Lam, R.S.-M. Wong, K.-H. Lam, L.-K. Hung, M.-M. Wong, L.-H. Yung, Y.-W. Ho, W.-Y. Wong, D.K.-P. Hau, R. Gambari, C.-H. Chui, *Chem. Biol. Inter.* **2020**, *320*, 109023.

(96) Toxic   lobbying: the   titanium   dioxide   label   debate   continues: https://corporateeurope.org/en/2019/06/toxic-lobbying-titanium-dioxide-label-debate-continues.

(97) H. Mikkelsen, R. Mcmullan, A. Filloux, *PLoS ONE,* **2011**, *6*, e29113.

(98) W. C. Oliver, G. M. & Pharr, *J. Mater. Res.* **1992**, *7*, 1564-1583.

4.7. Supporting Information

Table 4.2. General information concerning the Rietveld refinement.

General information	Description
Diffractometer	Stoe Stadi P
Detector	Dectris Mythen 1k
Wavelength (Å)	0.7093 (MoKα_1)
Temperature (K)	298
Program	TOPAS Academic 6.0
Number of parameters	17
Space group (cerianite)	Fm-3m
Wyckoff positions	Ce: 4a, O: 9c

Table 4.3. Information concerning the Rietveld refinement.

Sample	R_{wp}	Cell parameter (Å)	Crystallite size (nm)
MF RT	4.36	5.418(1)	5.86(7)
MF 185 °C	4.21	5.423(1)	5.83(5)
MF 500 °C	4.44	5.4141(2)	16.2(1)
MF 800 °C	8.70	5.41678(2)	71.5(4)
Batch RT	4.58	5.412(1)	3.15(2)
Batch 185 °C	4.28	5.417(2)	3.78(3)
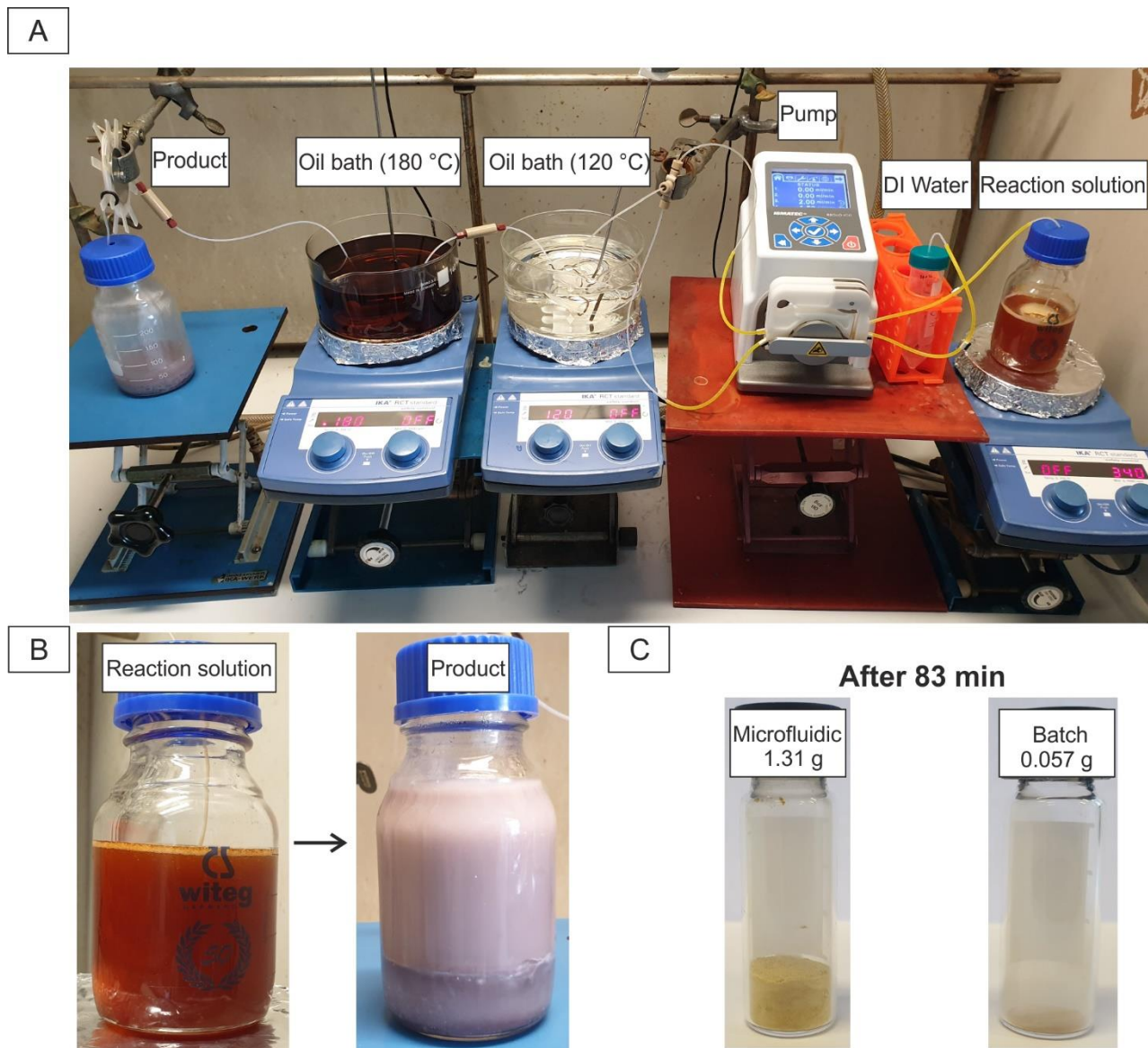
Figure 4.9. (A) Setup for the segmented flow, (B) comparison of the reaction solution and the product. (C) CeO$_2$ NPs after 83 minutes in the segmented flow and in the batch process.
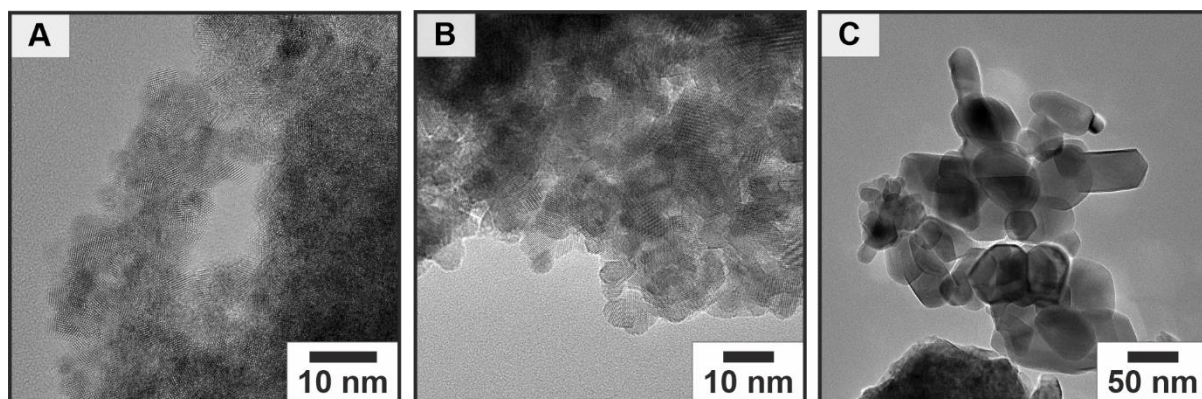
Figure 4.10. HRTEM images of CeO$_2$ NPs obtained under segmented flow conditions and annealed for 5 h at (A) 185 °C, (B) 500 °C and (C) 800 °C.
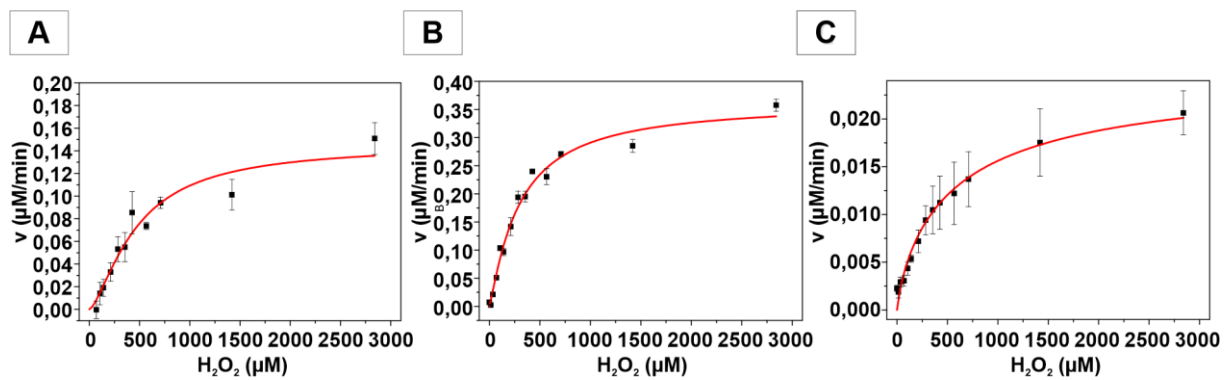
Figure 4.11. Michaelis-Menten kinetics for H_2O_2, with the corresponding Hill fit (red line) for the CeO_2 NPs obtained from the segmented flow (A) annealed at 185 °C, (B) 500 °C and (C) 800 °C.
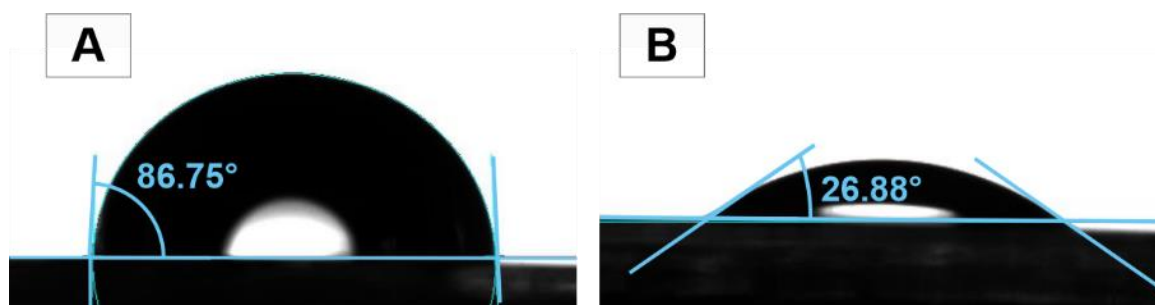
Figure 4.12. Contact angle measurements of polycarbonate with water (A) before and (B) after oxygen plasma treatment.
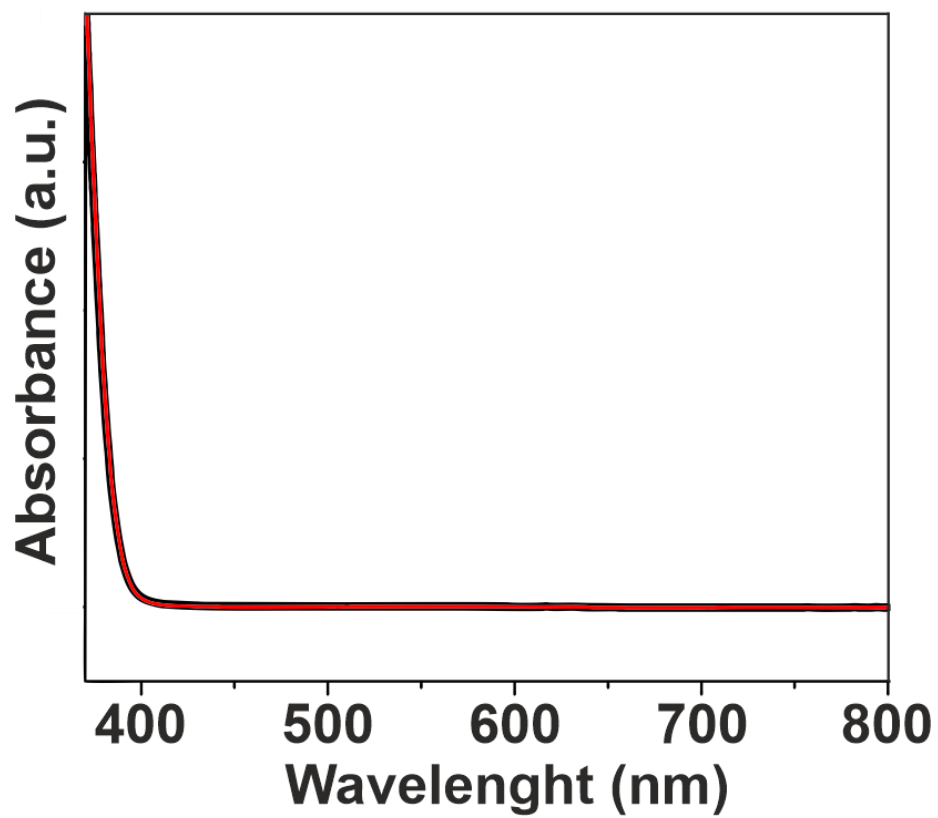
Figure 4.13. UV-VIS absorption spectra of polycarbonate before (black) and after coating (red) with CeO$_2$ NPs.

5. Generalized Synthesis of NaCrO₂ Particles for High-rate Sodium Ion Batteries Prepared by Microfluidic Synthesis in Segmented Flow
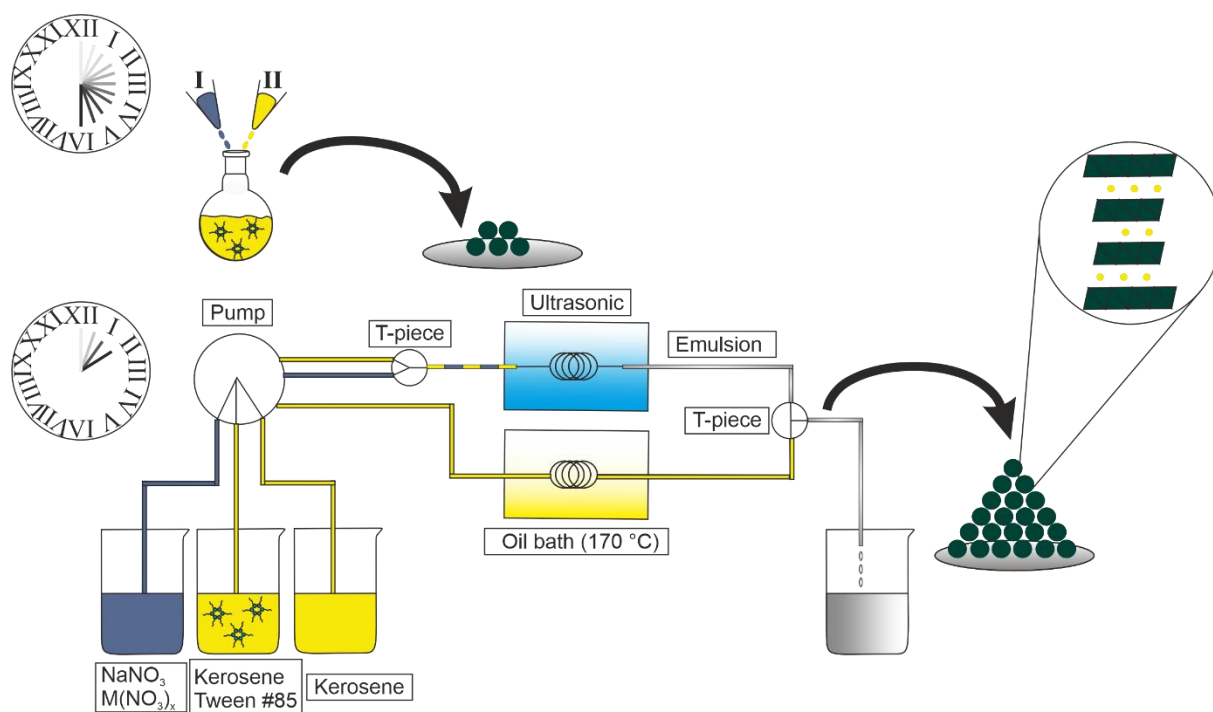
The following chapter will be submitted to Dalton Transaction. In the appendix of the dissertation a detailed authorship statement with the contributions of each author is attached.

5.1. Abstract

NaCrO$_2$ particles for high-rate sodium ion batteries were prepared on a multigram scale in segmented flow from chromium nitrate and sodium nitrate using a segregated flow water-in-oil emulsion drying process. Microfluidic processing is an environmentally friendly and rapid synthetic method, which facilitates large-scale industrial implementation for the production of materials with superior properties. The reaction time for NaCrO$_2$ nanocrystals was reduced by almost one order of magnitude compared to a standard batch process and by several orders of magntitude compared to a conventional solid-state reaction. In addition, it allows for an easy upscaling and was generalized for the synthesis of other layered oxides NaMO$_2$ (M = Cr, Fe, Co, Al). The automated water-in-oil emulsion approach circumvents the diffusion limits of solid-state reactions by allowing a rapid intermixing of the components at a molecular level in submicrometer-sized micelles. A combination of Raman and nuclear magnetic resonance spectroscopy (^{1}H, ^{23}Na), thermal analysis, X-ray diffraction and high resolution transmission electron microscopy provided insight into the formation mechanism of NaCrO$_2$ particles. The new synthesis method allows to produce cathode materials of different types in large scale, constant quality and in short reaction times in an automated manner.

5.2. Introduction

Lithium-ion batteries (LIBs) are considered a promising battery technology for combining renewable energy sources with large scale and high-energy applications for portable electronics or electric mobility.[1–4] The limited availability of lithium and other state-of-art-materials in LIBs lead to price increases on the world market and partial exhaustion of resources requires the development of alternatives for postlithium battery technologies. Sodium-ion batteries (SIBs) are promising alternative stationary energy storage devices based on cost effective and naturally abundant materials. The world sodium deposits are almost 400 times higher than those of lithium.[5,6] Therefore, sodium-based compounds could establish a new generation of commercial batteries. The chemical properties of lithium and sodium, including the intercalation chemistry, are similar in many aspects, and the redox potential of sodium is with –2.71 V[7] only 0.3 V higher than that of lithium.[4,8,9] Therefore, electrode materials are being developed, capable of accommodating the larger Na$^+$ cations and enabling highly reversible (de-)sodiation as well as stable long-term cycling, in order to enable Na-based energy storage.

A variety of different materials have been developed for use as potential SIBs.[1,4,9–13] Layered oxides with the formular Na_xMO_2 ($x \leq 1$, M = Ni, Co, Mn, Fe, V, Ti, Cr, Cu) showed high specific capacities, good thermal stability, excellent cyclability.[1,4,10,14] Layered oxides of the form ABO_2 have structures with MO_2 layers of edge sharing MO_6 octahedra. The A cations between these layers can have different (octahedral, prismatic, trigonal, or linear (for Delafossites)) site symmetries, based on the oxygen packing sequence.[15] Delmas et al.[15] categorized layered oxides into O3 and P2 type materials. The key difference between the O3 and P2 types is the occupation of Na^+ site between the slabs of the layered structure and therefore the oxide coordination of the Na^+ cations. In the α-$NaFeO_2$ structure type, the interlayer Na^+ site is octahedrally coordinated, and all metal oxide octahedra have the same orientation, described by the notation "O3" (octahedrally coordinated sodium ions, 3 layers). In the P2 type structure Na^+ occupies the prismatic sites between the MO_2 layers.[10,15,16] $NaCrO_2$ crystallizes in the α-$NaFeO_2$ structure (O3 type, space group $R\bar{3}m$) which has a sufficiently large sodium reservoir. Wang et al.[1] showed that $NaCrO_2$ has a reversible capacity of up to 123 mAh g^{-1} at 0.1C with excellent cycling performance up to 88.2% of the initial capacity after 500 cycles at 2C. Based on the outstanding performance of $NaCrO_2$ in SIBs, an automated large-scale synthesis with high conversion rates and therefore low reaction times is essential to meet the potential demand. An emulsion technique[4] to prepare $NaCrO_2$ in micelles serving as a reservoir for phase formation proved useful for a continuous flow synthesis. Flow reactions in micrometer-sized tubes can circumvent typical problems of batch processes, where the change of the surface-to-volume ratio during upscaling can change many important synthesis parameters (e.g., heat transfer) which impacts the composition and the properties of the products and prevents direct upscaling. The use of micrometer-sized flow tubes leaves the surface-to-volume ratio unchanged, and product particles with homogeneous dispersity, morphology or composition can be obtained. Furthermore, the high surface-to-volume ratio allows a higher heat transfer and a much higher higher conversion rate.[17,18] Therefore, flow reactions in microfluidic devices enable automated processes which are essential for large scale syntheses. Here, we report an automated flow synthesis based on an emulsion-drying method. Systematic studies were carried out to understand the formation mechanism of $NaCrO_2$ and and its $NaMO_2$ analogues.

5.3. Results and Discussion

An automated flow synthesis of $NaCrO_2$ with a high conversion rate and short reaction time was established based on an emulsion drying technique.[4] Figure 5.1 shows the experimental set up for the synthesis. Channel 1 contains a Tween surfactant/kerosene solution (solution 1), channel 2 contained a mixture of $Cr(NO_3)_3 \cdot 9\ H_2O$ and $NaNO_3$ in deionized water (solution 2). The two solutions were connected through a T-fitting. Due to the immiscibility of kerosene and water, the flow is segmented, i.e. each segment contains alternating mixtures of channel 1 or 2. Preliminary experiments were done to produce an emulsion inside the tubes. Figure 5.6 (SI) indicates ultrasonicating of both mixtures to be sufficient to form an emulsion. Channel 3 contains kerosene (solution 3), which passes an oil bath with T = 180 °C. After passing the oil bath, the hot kerosene and the emulsion were mixed by a T-segment. The resulting mixture was collected, and water and kerosene were removed through a spiral-type condenser. The final product was obtained by heating the resulting powder under argon for 4 hours at 800 °C.

Compared to the emulsion/drying techniques, the reaction time could be reduced by a factor 8. The most time-consuming steps were the combination of solution 1 and 2, and combining the resulting emulsion with solution 3. By setting suitable flow rates for each channel, we could avoid long reaction times and quadrupel the yield within a given time period.

The final product was obtained by heating the residue under argon (to avoid the oxidation of Cr^{3+} to Cr^{4+} or Cr^{6+}) for 4 hours at 800 °C after removing water and kerosene. An annealing temperature of 800 °C was needed to obtain single-phase $NaCrO_2$. X-ray powder diffraction (XRPD) patterns (Figure 5.2A) of the products obtained at annealing temperatures (400 – 800 °C) always show the formation of $NaCrO_2$ with minor impurities (Figure 5.2A). The diffractograms in Figure 5.2B show that single phase product was obtained after increasing the amount of sample by a factor of ten compared to a conventional batch process, i.e., an upscaling can be done without any difficulties.
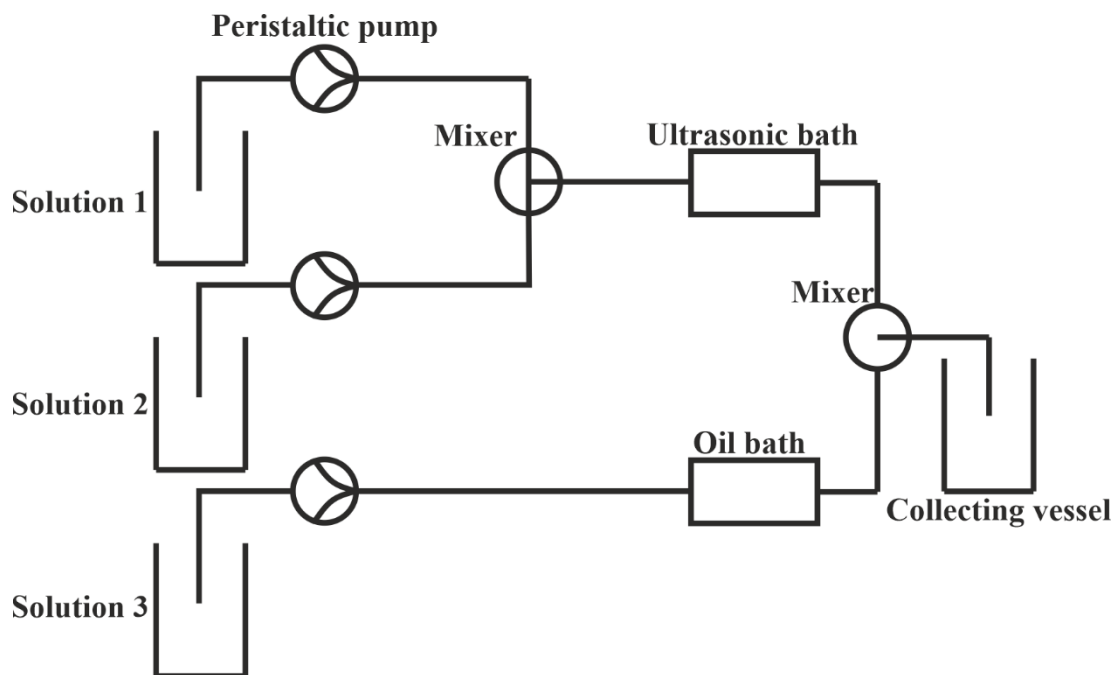
Figure 5.1. Experimental setup for the synthesis. Solution 1 contains a Tween/kerosene mixture, solution 2 contains $Cr(NO_3)_3 \cdot 9\,H_2O$ and $NaNO_3$ in deionized water, solution 3 contains kerosene.
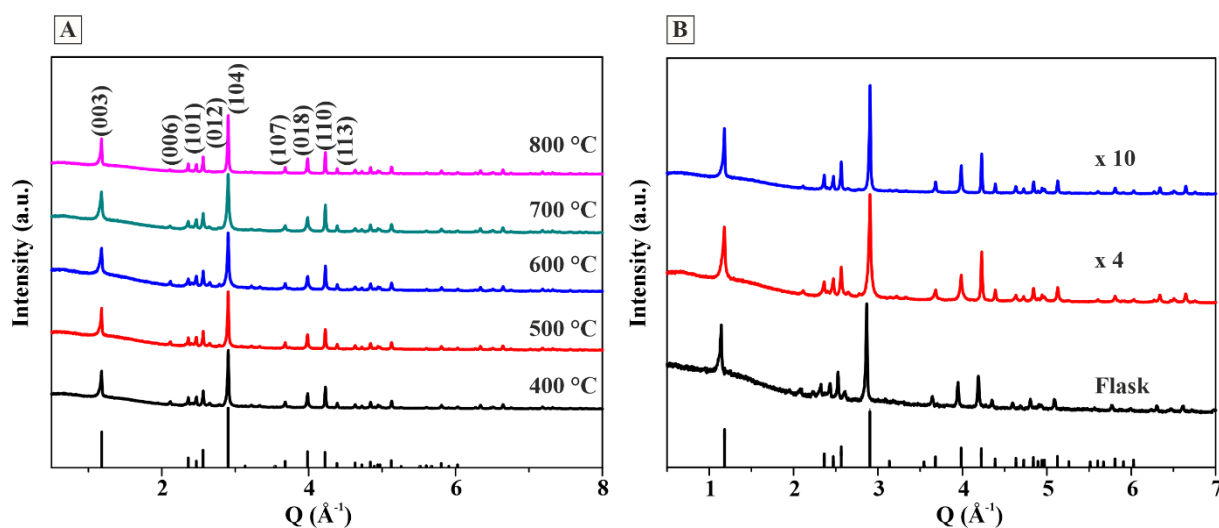

Figure 5.2. XRPD patterns obtained after (A) different annealing temperatures and (B) at different scale ups in comparison with the flask synthesis, with $NaCrO_2$ (black ticks) as reference.

Pawley refinement of the product obtained by annealing at 800 °C (Figure 5.3A) shows the formation of a highly crystalline product. Details concerning the refinement are given in the supporting information (Table 5.1). A HRTEM image of a crystalline nanoplate (Figure 5.3B) shows well-defined lattice fringes with an interplanar distance of 5.33 Å corresponding to the (003) plane. The corresponding diffraction pattern shows a single set of reflections confirming that the particles are either single crystalline or contain several domains sharing identical facets. SEM images confirm the platelike morphology of the particles (Figure 5.7A (SI)), and the

elemental mapping (Figure 5.7B-C) shows the presence of Na and Cr in equal quantities. XPS survey spectra show the presence of Na, Cr and O surface species (Figure 5.3C). The high-resolution image of the Cr 2p spectrum shows the positions at 577 eV ($2p_{3/2}$) and at 587 eV ($2p_{1/2}$) (Figure 5.3D), compatible with the presence of Cr^{3+} (peak positions for Cr^{4+} are located at 580 eV and latter 588 eV).[19]
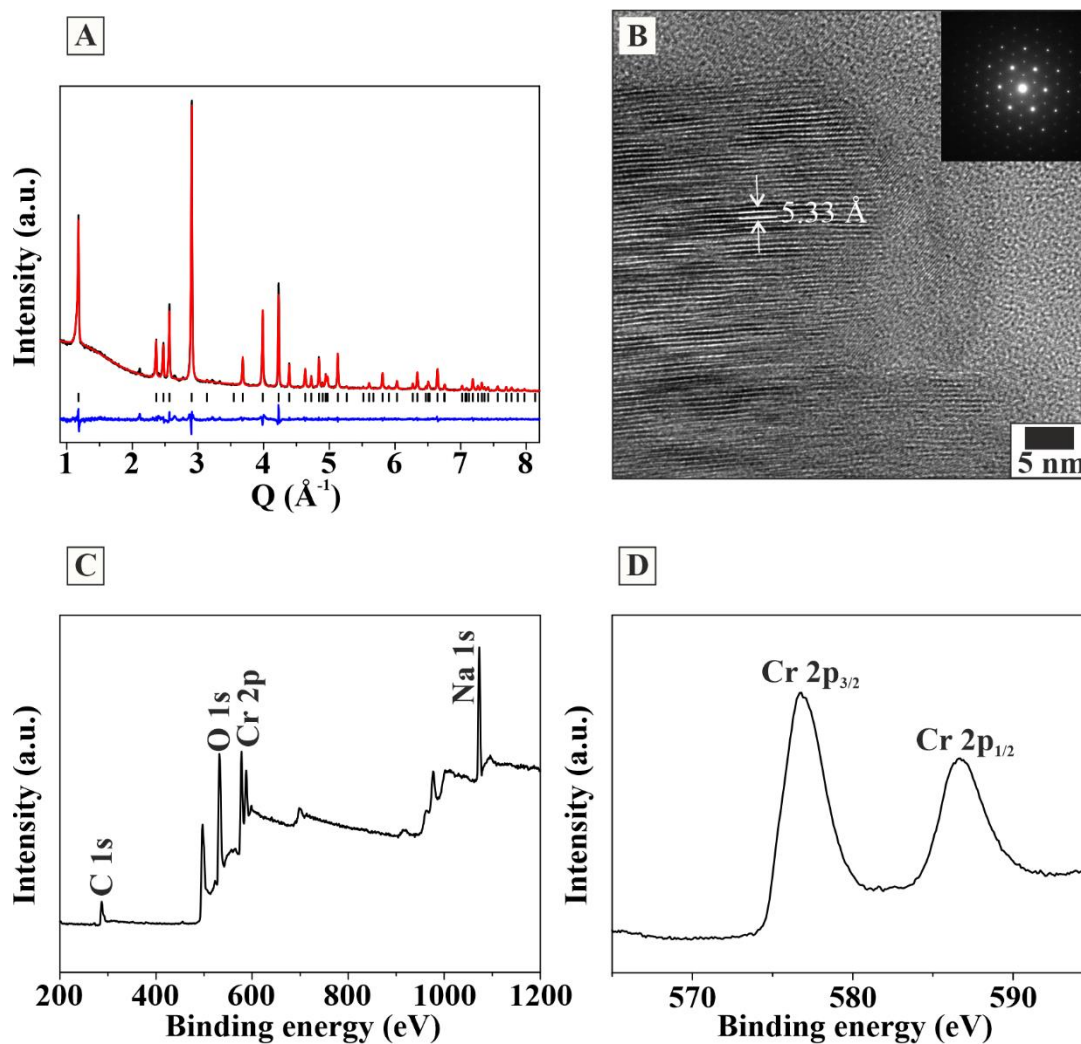

Figure 5.3. (A) XRPD pattern with Pawley refinement for $NaCrO_2$ obtained after annealing at 800 °C for 4 h. Experimental data (black line), Pawley refinement (red line), difference curve (blue line). Ticks indicate theoretical positions of Bragg intensities. (B) HRTEM-image with the corresponding diffraction pattern as inset. (C) XPS survey spectra and (D) Cr 2p spectra of the obtained particles.

Nucleation and growth of $NaCrO_2$ required a short annealing at 400°C (Figure 5.2A). The XRPD pattern and Raman spectrum of the oily pre-annealed intermediate (Figure 5.4A- B) show only the presence of $NaNO_3$ (melting point of 308°C), i.e., the formation of the $NaCrO_2$ product phase is likely to occur within the micelles. The vibration bands at 1385 cm^{-1} (v_3) and 725 cm^{-1} (v_4) and the band at 185 cm^{-1} can be assigned to the E_g modes and the libration mode

114

of the nitrate anion. The vibration at 1068 cm^{-1} belongs to the A_{1g} (v_4).[20] Two vibrations of the annealed product (Figure 5.4C) at 450 and 572 cm^{-1} (A_{1g}) are compatible with the Cr-O vibrations in $NaCrO_2$.[21] No vibrations of the starting compound $NaNO_3$ occurred after annealing, i.e., indicating the transformation to be complete.

The diffraction data and Raman spectra suggest that the micelles formed by the Tween surfactant serve as nanoreactors that encapsulate the educts during the emulsion-drying. During the removal of water and kerosene in the spiral type condenser, the micelles precipitate while the educts are still encapsulated and intermixed on an atomic level and in an appropriate ratio. This reduces the transport distances to atomic dimension, compared to transport lengths in the order of μm in conventional solid-state reactions. It is even more crucial when one recalls that the diffusion coefficients in the solid state typically range from 10^{-16} to 10^{-12} cm^2/s.[22] As a consequence, solid-state reactions typically require a high thermal activation and long reaction times. This favors thermodynamic control and the formation of thermodynamically stable products, which significantly hampers the reproducibility and predictability in solid-state synthesis.

The micelles collapse upon heating. $NaNO_3$ melts at 308°C, and $Cr(NO_3)_3$ decomposes inside to carbonized "nanoreactors" to form nanosized $NaCrO_2$. Laser scanning microscopy images of the pre-annealed sample (Figure 5.8A-B (SI)) shows two different laser scanning microscopy images in support of our hypothesis.

The ^{23}Na solid state NMR spectrum of the pre-annealed sample (Figure 5.4D black) shows a single resonance at δ = - 8.01 ppm (with respect to solid NaCl), which perfectly matches to the sodium signal in $NaNO_3$.[23] This sharp spectral line disappears in the ^{23}Na-NMR spectrum of the annealed product (Figure 5.4D red) which confirms the complete transformation of the starting product. Instead, three broad ^{23}Na resonances appear in the NMR spectrum indicating three new sodium environments. Measurements at different spinning frequencies were carried out to distinguish the centerband from the spinning sideband envelope (Figure 5.9A-B (SI)). Assuming that the major ^{23}Na shift contribution arises due to the chromium ions in the first coordination sphere and that there are no significant interactions between the paramagnets at ambient temperature[24] the significant low field shift of ca -270 ppm of one of the ^{23}Na lines is due to the hyperfine interaction with Cr^{3+}. Figure 5.4E shows the polarization mechanism related with the negative sign of the spin density transferred to the Na 3s orbital.[24]

Additionally, two more sodium resonances are detected in the ^{23}Na NMR spectrum of the annealed product. Their shifts are in the spectral region for sodium in diamagnetic compounds (most probably arising from sodium related with the diamagnetic Cr^{6+}, i.e. $Na_2Cr_2O_7$). As long

as no other phase was detected in the XPRD pattern of the annealed product these sodium environments should be disordered.

Further confirmation for the success of the synthesis is observed when comparing the ^{1}H-NMR spectra (Figure 5.10 (SI)) of the pre-annealed and the annealed samples. Proton resonances originating from the surfactant molecules involved in micelle formation in the product mixture are clearly detected in the pre-annealed product, whereas these signals disappear in the ^{1}H NMR spectrum of the product after annealing at 800 °C. Also, the respective C-H vibrations after annealing are no longer observed in the FTIR spectrum. (Figure 5.11 (SI)).
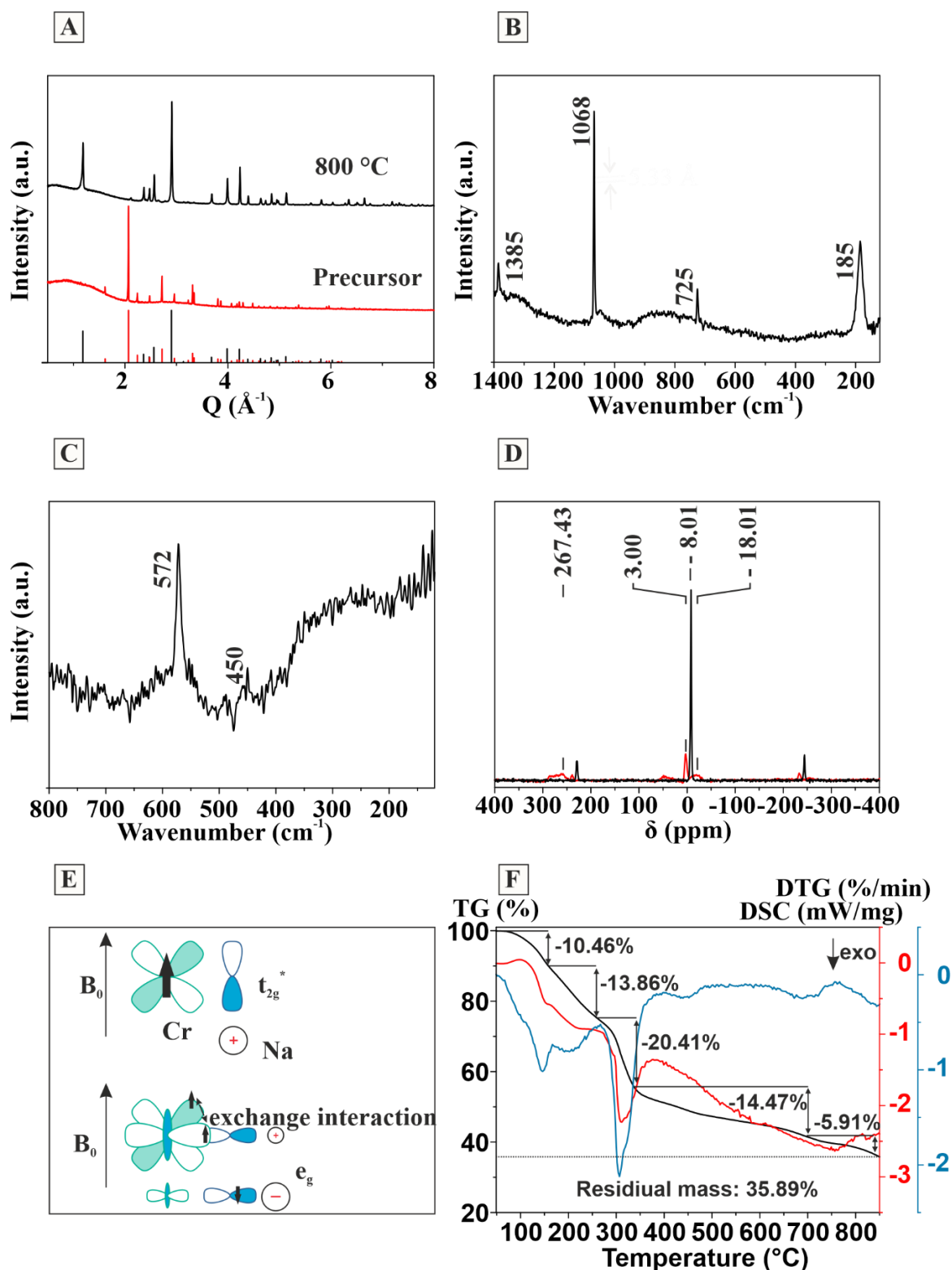
Figure 5.4. (A) XRPDs before (red) and after annealing (black) at 800 °C, with the corresponding references NaCrO₂ (black ticks) and NaNO₃ (red ticks). Raman spectra (B) before annealing and (C) after annealing. (D) ^{23}Na-NMR before (black) and after annealing (red) referred to solid NaCl. (E) Molecular t_{2g}* (top) and e_g (bottom) orbitals of Cr^{3+} in NaCrO₂ in an external magnetic field with the polarization mechanism between Cr^{3+} and Na^+, (F) TG/DTG/DSC analysis of the pre-annealed product. The TG trave is shown in black, the DSC trace in red and DTG trace in blue.

Figure 5.4F shows the TG/DTG/DSC measurements of the pre-annealed product. In order to avoid the oxidation of Cr^{3+} to higher oxidation states inert gas conditions were used. The TG trace reveals a mass loss of 64.11% in 5 different stages. The first stage corresponds to a mass loss of 10.46%. The DSC trace shows an endothermic process at around 100 °C indicating the evaporation of water as an explanation of the first stage mass loss. The 2nd stage mass loss of 13.86% at ~135°C is attributed to kerosene evaporation. Bello et. al[25] reported that the onset temperature of pure kerosene starts at 135 °C corresponding with our results. The third stage shows a significant mass loss of about 20.41% at a temperature range from 260 – 340 °C. The DSC curve shows an exothermic reaction with a minimum at 307 °C compatible with the combustion of tween 85.[26] The fourth and fifth stage is very broad indicating the pyrolysis of indistinct compounds. The overall mass loss during the fourth stage is 14.47% and 5.91% during the fifth stage in a temperature range of 340 – 850 °C. Taking the XRPD pattern of Figure 5.2A into account, the formation of $NaCrO_2$ already occurs at 400 °C, indicating the reduction of $NaNO_3$ (thermal decomposition occurs between 570 and 760°C).[27] Therefore stages 4 and 5 are attributed to a decomposition of the pyrolysis products formed by the decomposition of tween 85 in stage 3, but also to the decomposition of $NaNO_3$. The decomposition temperature for $NaNO_3$ may vary depending on the heating rate, composition of the sample and many other factors.[27] In summary, Figure 5.4 shows the formation of the micelles, and their decomposition together with $NaNO_3$ leading to the formation of $NaCrO_2$ as final product.

The setup for the synthesis of $NaCrO_2$ was used for the synthesis of the layered oxides Na_xMO_2 ($x \leq 1$) to show that a wider range of materials can be prepared using the setup. Except for the metal precursor, neither the composition of the single solutions, nor the flow rate or the setup was changed. $Fe(NO_3)_3$, $Co(ac)_2$ and $Al(NO_3)_3$ were used as metal precursors for the synthesis of $NaFeO_2$, $NaCoO_2$ and $NaAlO_2$. Figure 5.5 shows the obtained XPRD patterns for each compound with the corresponding reference. The XRPD pattern of $NaFeO_2$ shows two different polymorphs which could be assigned to α-$NaFeO_2$ (hexagonal, red ticks) and β-$NaFeO_2$ (orthorhombic, black ticks). The former one consists of edge-sharing NaO_6 and FeO_6 octahedral units alternating along the ab plane. The latter one consists of corner-sharing tetrahedral $NaO4$ and FeO_4 units in the ac plane.[28-30]
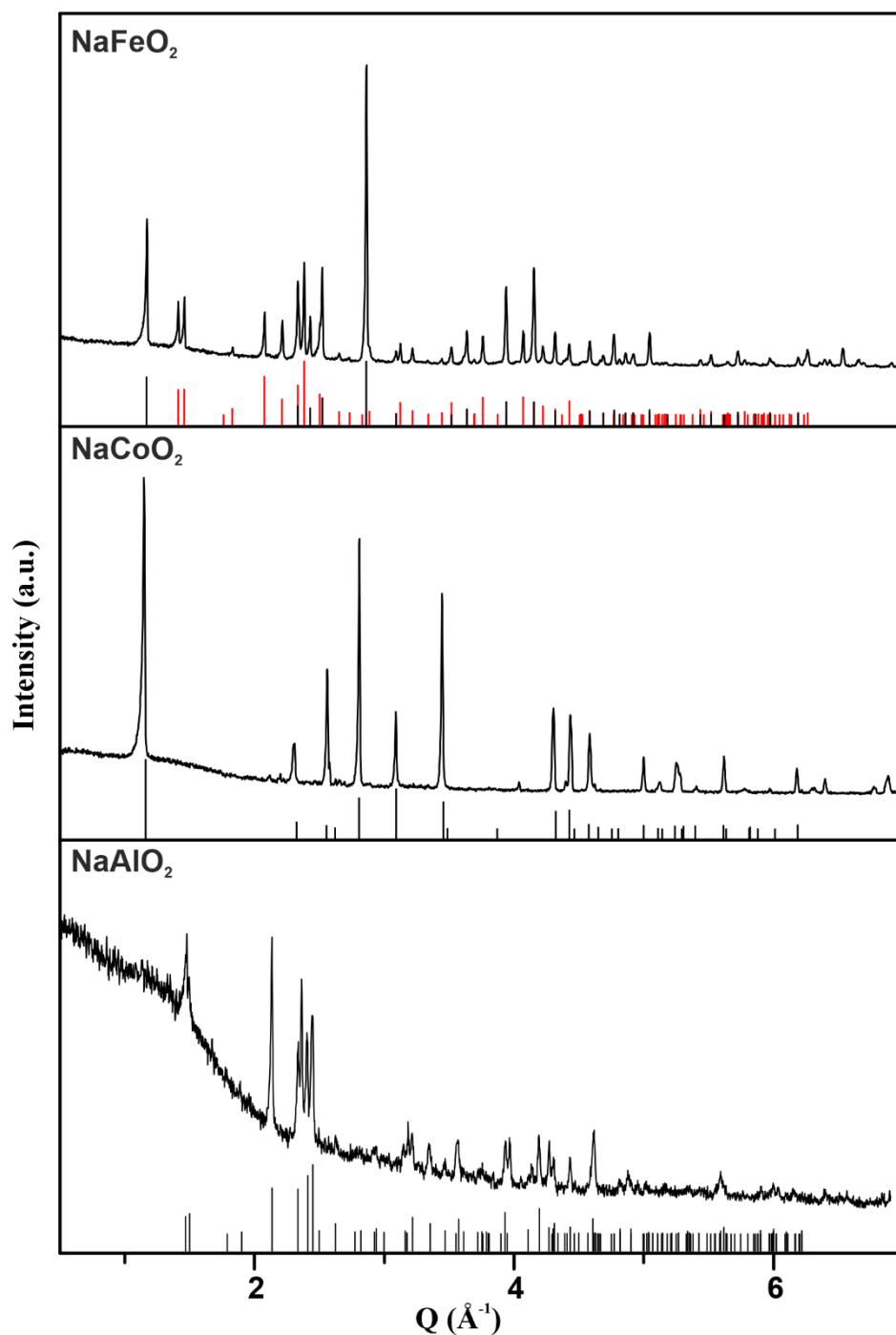
Figure 5.5. XRPD patterns of the layered oxides NaFeO₂, NaCoO₂ and NaAlO₂. XRPD patterns of NaFeO₂ with α-NaFeO₂ (red ticks) and β-NaFeO₂ (black ticks) as reference and of NaCoO₂ and NaAlO₂ with the corresponding reference.

Several factors appear to be important for the polymorph selection. The transition of α-NaFeO₂ to β-NaFeO₂ was reported to occur at 760 °C.[31-33]

As the precursor was annealed at 800 °C for only 4 hours, the rate of the solid state phase transition (or the dwell time) seems to be responsible for the formation of both polymorphs (Figure 5.5). Annealing for 4 hours at 900 °C led to the formation of the high-temperature phase

β-NaFeO$_2$ (with minor impurities of magnetite, Fe$_3$O$_4$), indicating the phase transition of α-NaFeO$_2$ to β-NaFeO$_2$ to be complete (Figure 5.12 (SI)). Pure NaCoO$_2$ was formed when Co(ac)$_2$ was used as metal precursor, as shown by the XRPD pattern with the corresponding reference in Figure 5.5. Likewise, pure NaAlO$_2$ could be prepared using Al(NO$_3$)$_3$ as Al precursor (Figure 5.5). The XRPD patterns in Figure 5.5 show that layered oxides NaMO$_2$ (M = main group and 3d transition metals) can be prepared by a generalized segmented flow approach using an identical setup, flow rates and reaction/annealing temperatures in very high yields and in relatively short reaction times.

5.4. Conclusion

We have demonstrated an efficient segmented flow synthesis of NaCrO$_2$ particles, which allows the synthesis of large amounts of NaMO$_2$ (M = main group and 3d transition metals) within short reaction times. The yields may be enhanced significantly by parallelization of the setup. Efforts were also made to understand particle growth and the NaCrO$_2$ surface chemistry. The successful and reproducible (automated) synthesis of NaCrO$_2$ NPs in large amounts allowed us, to systematically analyze the formation mechanism.

The micelles formed by the surfactant in water-in-oil emulsion-drying approach serve as nanoreactors that confine reaction volumes to nanometer size. This aids in overcoming the limitations of solid-state reactions due to solid state diffusion. Traditional solid-state synthesis require elevated temperatures or long reaction times to increase reaction rates. Alternatively, lower activation energies for diffusion can be achieved by going to a fluid phase (fluxes, vapor phase transport, solvothermal reactions).[34] The emulsion-drying approach shortens the diffusion paths down to molecular scale by using ionic precursors to prepare intimately mixed reactants which transform upon short-time annealing at low temperatures into the crystalline solids. A key issue in the annealing step is the need to remove surfactant molecules trapped in the micelle "nanoreactors". The setup could also be used for other metal layered oxides, potentially allowing a range of potential cathode materials to be produced using the setup. The much shorter reaction time also allows high yields to be realized in short time frames, which can be further increased by parallelizing the setup. As a result, the synthesis strategy offers an alternative to the already established methods for the large-scale industrial production of cathode materials

5.5. Experimental Section

Materials and Methods

Materials. NaNO$_3$ (> 99% Sigma Aldrich), Cr(NO$_3$)$_3$ · 9 H$_2$O (99% Acros Organics), Tween #85 (Sigma Aldrich), kerosene (reagent grade Sigma Aldrich), deionized water, fluorinated ethylene propylene tube with 1/16'' OD and 1 mm ID (Fisher Scientific), peristaltic pump reglo ICC (Ismatec), ultrasonic bath (Elma S 30 H).

Flask Synthesis. Before the synthesis 50 µL of Tween #85 was diluted in 50 mL of kerosene and stirred in a 100 mL beaker for 24 hours at room temperature to form the micelles. 2.5 mmol of Cr(NO$_3$)$_3$ x 9 H$_2$O and 2.5 mmol of NaNO$_3$ were diluted in 50 mL of deionized water and stirred in a second beaker at room temperature. The oil mixture was transferred into a 250 mL flask, and the aqueous solution was introduced to the oil mixture through a dropping funnel with a rate of 3-5 droplets per second. The precursor was obtained by dropping the emulsion into hot kerosene (170-180 °C). Remaining water and kerosene were removed through a spiral-type condenser. The powder was heated in an argon oven at 800 °C for 4 hours to form the product.

Segmented Flow Synthesis. Before the synthesis 500 µL of Tween #85 was diluted in 500 mL of kerosene and stirred in a 500 mL beaker for 24 hours at room temperature to form the micelles. 25 mmol of Cr(NO$_3$)$_3$ x 9 H$_2$O and 25 mmol of NaNO$_3$ were diluted in 500 mL of deionized water and stirred in a second beaker at room temperature. Kerosene was added in a third beaker. The overall tube length was 6 m. The first segment (3 m) was put in an ultrasonic bath at room temperature, the second segment (3 m) was heated in an oil bath to 170-180 °C. The three solutions were pumped separately, the flow rate for the aqueous and the kerosene/Tween #85 solution were 1 mL/min, the flow rate for the kerosene was 4.0 mL/min. The two solutions were connected through a T-fitting. The resulting emulsion and kerosene were connected through another T-fitting. Water and kerosene were removed after the reaction through a spiral type condenser. The powder was heated in an argon oven at 800 °C for 4 hours to form the final product.

For the other layered oxides, the precursors Fe(NO$_3$)$_3$, Co(ac)$_2$ and Al(NO$_3$)$_3$ were used, while the other parameters kept the same.

X-ray Powder Diffraction. X-ray diffraction patterns were recorded on a STOE Stadi P diffractometer equipped with a Dectris Mythen 1k detector in transmission mode using Mo Kα_1 radiation. Crystalline phases were identified according to the PDF–2 database using Bruker

AXS EVA 10.0 software. Full pattern profile fits (Pawley / Rietveld) were performed with TOPAS Academic 6.0 applying the fundamental parameter approach.[34]

Transmission Electron Microscopy (TEM). TEM mages for determining the size and morphology were acquired on a FEI Tecnai G2 Spirit microscope operating at 120 kV (LaB$_6$ filament), equipped with a Gatan US1000 CCD-camera (16-bit, 2048 × 2048 pixels), using the Gatan Digital Micrograph software. Samples for TEM were prepared by placing one drop (10 µL) of a diluted solution in deionized water (0.1 mg mL^{-1}) on a carbon-coated copper grid and by letting it dry at room temperature. Size evaluation of individual particles on the TEM images was performed with ImageJ.

High Resolution Transmission electron microscopy. The Samples were prepared adding a drop of diluted precursor in deionized water on a carbon coated copper grid. The samples were measured with the FEI Tecnai F30 ST TEM at 300 kV acceleration voltage equipped with a Gatan US4000 4k CCD camera.

Scanning Electron Microscopy (SEM). SEM images for demonstrating the presence of chromium and sodium on the surface were acquired on a FEI Nova NanoSEM with a EDX-detector (EDAX-Pegasus X4M). The samples were coated with gold before investigation and observed at 5 kV.

IR Spectroscopy. ATR-IR spectra were measured on a Nicolet iS10 Spectrometer manufactured by Thermo Scientific. The spectra were recorded in a frequency range from 650 cm^{-1} to 4000 cm^{-1} with a resolution of 1.4 cm^{-1} per data point.

X-ray photoelectron spectroscopy (XPS). X-ray photoelectron spectroscopy (XPS) measurements were performed on a Kratos AXIS Ultra DLD instrument using a monochromatic Al Ka x-ray source.

Laser scanning microscopy. The measurements were performed on a Keyence Model VK-8710 color 3-D laser scanning microscope equipped with CF Plan Lenses - 10x / 20x / 50x / 100x.

TGA/DSC. The measurements were performed on a Netzsch STA 409 PC/PG. The analysis was recorded in a temperature range from 35 °C to 1000 °C with a heating rate of 5 °C/min under argon atmosphere.

Solid-State NMR Spectroscopy. All solid-state NMR spectra were recorded on a Bruker Advance 400 DSX NMR spectrometer (Bruker BioSpin GmbH, Rheinstteten, Germany) at ^{1}H frequency of 399.87 MHz and ^{23}Na frequency of 105.74 MHz. A commercial three-channel 4 mm Bruker probe head was used for all experiments. The ^{1}H and ^{23}Na NMR spectra were

recorded at 10 kHz magic angle spinning (MAS) in both cases averaging 32 transients with 8 s and 5 s recycle delay respectively.

5.6. References

(1) Y. Wang, W. Li, G. Hu, Z. Peng, Y. Cao, H. Gao, K. Du and J. B. Goodenough, *Chem. Mater.*, 2019, **31**, 5214–5223.

(2) M. Winter, B. Barnett and K. Xu, *Chem. Rev.*, 2018, **118** , 11433–11456.

(3) J. Xie and Y.-C. Lu, *Nat. Commun.*, 2020, **11**, 2499.

(4) C.-Y. Yu, J.-S. Park, H.-G.Jung, K.-Y. Chung, D. Aurbach, Y.-K. Sun and S.-T Myung, *Energy Environ. Sci.*, 2015, **8**, 2019–2026.

(5) A. V. Naumov and M. A. Naumova, *Russ. J. Non-Ferr. Met.*, 2010, **51**, 324–330.

(6) H. K Wedepohl, *Geochim. et Cosmochim. Acta*, 1995, **59**, 1217–1232.

(7) B. L. Ellis and L. F. Nazar, *Curr. Opin. Solid State Mater. Sci.*, 2012, **16**, 168–177.

(8) S.-W. Kim, D.-H. Seo, X. Ma, G. Ceder and K. Kang, *Adv. Energy. Mater.*, 2012, **2**, 710–721.

(9) V. Palomares, P. Serras, I. Villaluenga, K. B. Hueso, J. Carretero-González and T. Rojo, *Energy Environ. Sci.*, 2012, **5**, 5884.

(10) P.-F. Wang, Y. You, Y.-X. Yin and Y.-G. Guo, *J. Mater. Chem. A*, 2016, **4**, 17660–17664.

(11) B. V. Rami Reddy, R. Ravikumar, C. Nithya and S. Gopukumar, *J. Mater. Chem. A*, 2015, **3**, 18059–18063.

(12) M. Guignard, C. Didier, J. Darriet, P. Bordet, E. Elkaïm and C. Delmas, *Nat. Mater.*, 2013, **12**, 74–80.

(13) Y. Jiang, Z. Yang, W. Li, L. Zeng, F. Pan, M. Wang, X. Wei, G. Hu, L. Gu and Y. Yu, *Adv.Energy. Mater.*, 2015, **5** , 1402104.

(14) X. Xia and J. R. Dahn, *Electrochem. Solid-State Lett.*, 2012, **15**, A1.

(15) C. Delmas, C. Fouassier and P. Hagenmuller, *Physica*, 1980, **99B**, 81–85.

(16) N. Yabuuchi, K. Kubota, M. Dahbi and S. Komaba, *Chem. Rev.*, 2014, **114**, 11636–11682.

(17) Y. Song, J. Hormes, C. S. S. R. Kumar, *Small*, 2008, **4**, 698.

(18) J. Wang and Y. Song, *Small*, 2017, **13**, 1604084.

(19) L. Lavielle and H. Kessler, *J. Electron Spectros. Relat, Phenomena*, 1976, **8**, 95–107.

(20)   D. L. Rousseau, R. E. Miller and G. E. Leroi, *J. Chem. Phys.*, 1968, **48**, 3409–3413.

(21)   P. Brüesch and C. Schüler, *J, Phys. Chem. Solids*, 1971, **32**, 1025–1038.

(22)   H. Schäfer, *Angew. Chem.*, 1971, **10**, 43-50.

(23)   D. Freude, in *Encyclopedia of Analytical Chemistry*, ed. R. A. Meyers, John Wiley & Sons Ltd, Chichester, 2000, pp. 12188-12224.

(24)   C. P. Grey and M. Dupré, *Chem. Rev*., 2004, **104**, 4493-4512.

(25)   M. N. Bello, K. J. Hill, M. L. Pantoya, R. J. Jouet and J. M. Horn, *Combust. Flame*, 2018, **188**, 243-249.

(26)   S.-T. Myung, N. Kumagai, S. Komaba and H. T. Chung, *J. Appl. Electrochem.*, 2000, **30**,1081-1085.

(27)   P. Gimenez and S. Fereres, *Energy Procedia*, 2015, **69**, 654-662.

(28)   Y. Takeda, K. Nakahara, M. Nishijima, N. Imanishi, O. Yamamoto and M. Takano, R.Kanno, *Mater. Res. Bull*., 1994, **29**, 659-666.

(29)   I. E. Grey, R. J. Hill and A. W. Hewat, *Z. Kristallogr.*, 1990, **193**, 51-69.

(30)   N. Kuganathan, N. Kelaidis and A. Chroneos, *Mater.*, 2019, **12**, 3243.

(31)   J. Théry and R. Collongues*, C. R. Acad. Sci.*, 1958, **247**, 2003.

(32)   J. Théry, *Annales de Chimie*, 1962, **7**, 207.

(33)   Y. Takeda, J. Akagi, A. Edagawa, M. Inagaki and S. Naka, *Mater. Res. Bull.*, 1980, **15**,1167-1172.

(34)   D. L. M Cordova and D. C. Johnson, *ChemPhysChem*, 2020, **21**, 1345-1368.

(35)   A. A. Coelho, *J. Appl. Crystallogr*., 2018, **21**, 210-218.

5.7. Supporting Information

Table 5.1. General information concerning the Pawley refinement.

General information	Description
Diffractometer	Stoe Stadi P
Detector	Dectris Mythen 1k
Wavelength (Å)	0.7093 (MoKα_1)
Temperature (K)	298
Program	TOPAS Academic 6.0
Space group of parameters	R$\bar{3}$m
R$_{wp}$	4.8
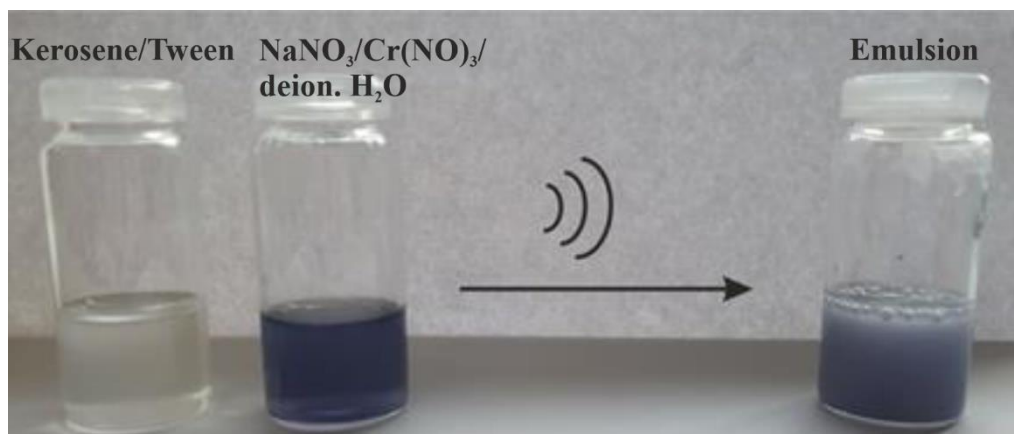
Figure 5.6. Preliminary test to form an emulsion by using an ultrasonic bath.
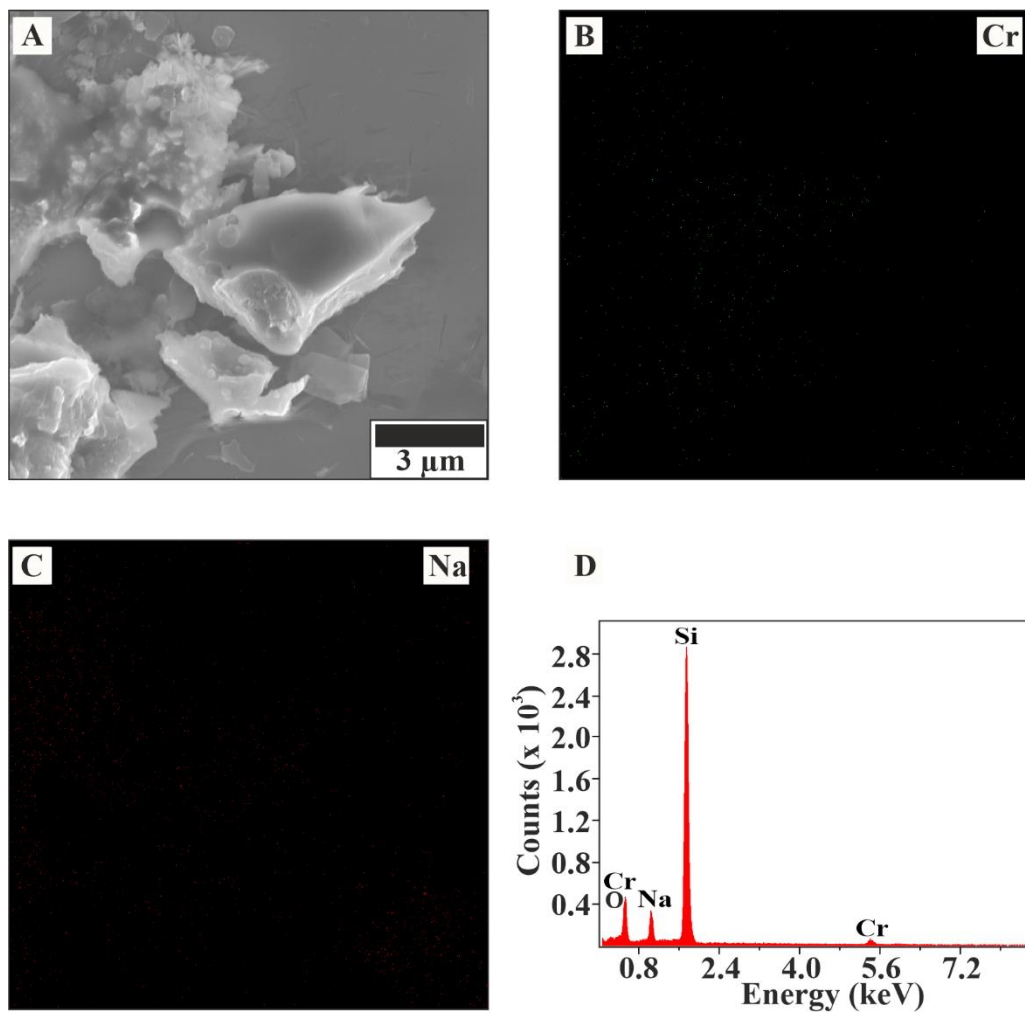
Figure 5.7. (A) SEM-image of the annealed sample with the corresponding elemental EDX mapping of (B) Cr and (C) Na and an (D) overview spectra.
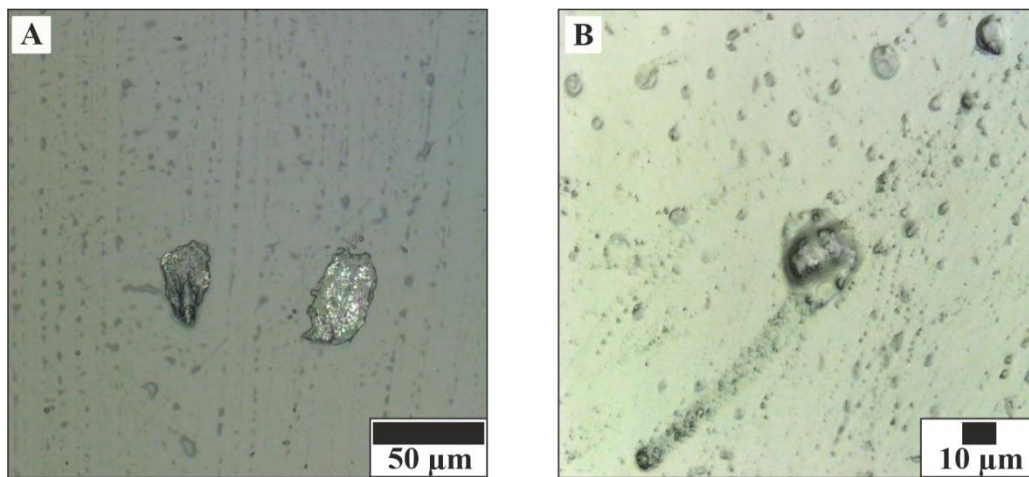
Figure 5.8. Laser scanning microscopy images with (A) low and (B) high magnification.
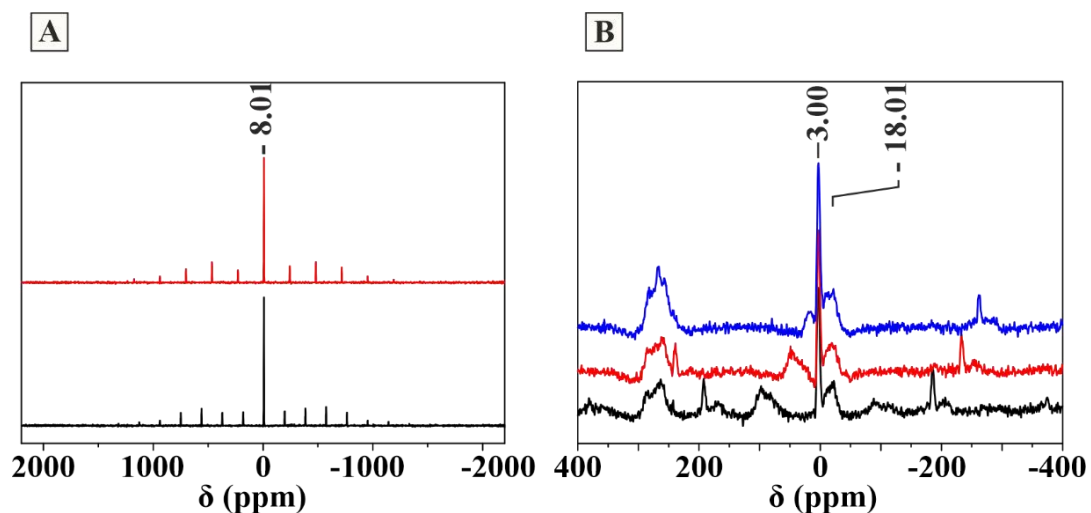
Figure 5.9. ²³Na-NMR spectra of (A) the pre-annealed sample measured at a frequency of 20 (black) and 25 khz (red) and (B) the annealed sample measured at a frequency of 20 (black), 25 (red) and 28 kHz (blue), to determine the satellite signals.
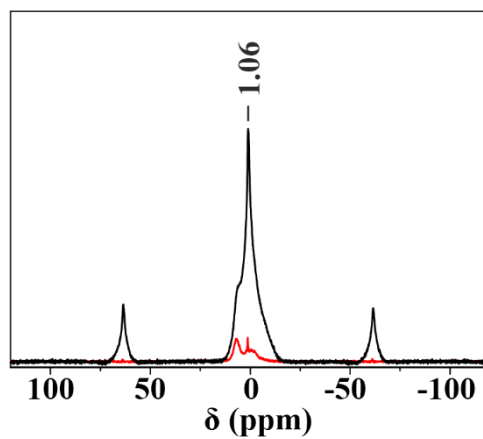
Figure 5.10. ^{1}H-NMR before (black) and after annealing (red). The signal with low intensity in the red spectrum arises from background
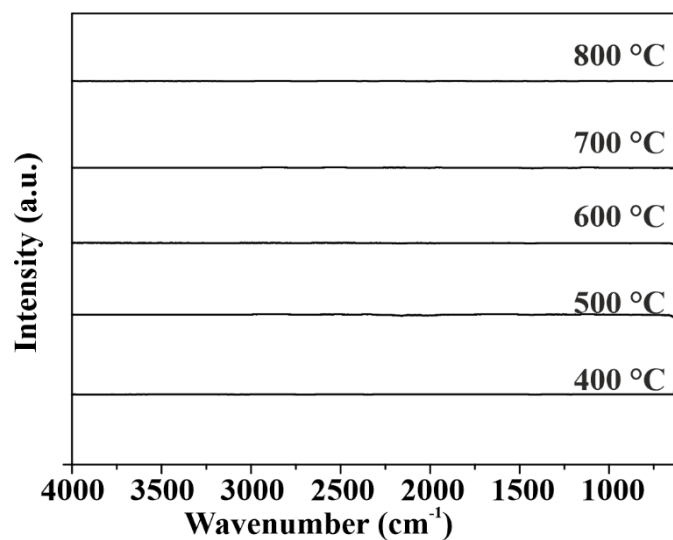
Figure 5.11. IR spectra NaCrO$_2$ after annealing at different temperatures.
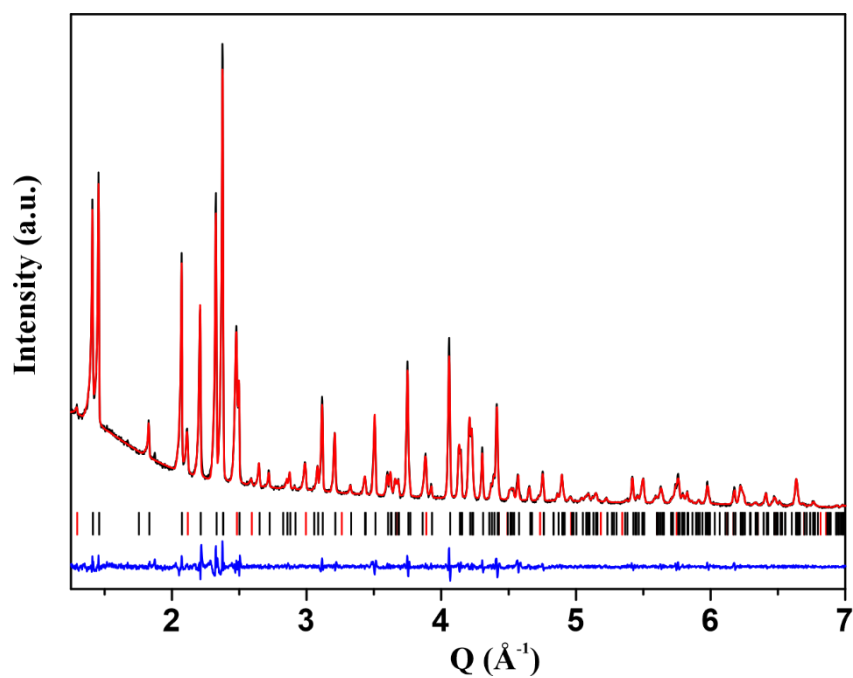
Figure 5.12. XRPD pattern with Pawley refinement for $NaFeO_2$ obtained after annealing at 900 °C for 4 h. Experimental data (black line), Pawley refinement (red line; $R_{wp} = 4.1$, space group $Pna2_1$), difference curve (blue line). Ticks indicate theoretical positions of Bragg intensities for $NaFeO_2$ (black) and Fe_3O_4 (red).

6. Conclusion and Outlook

This work addresses the preparation of various NPs using different synthesis methods, as well as the characterization and potential applications of the particles. Two wet chemical methods for the targeted preparation of nanocrystals were used preferentially: (i) discontinuous batch and (ii) microfluidic synthesis. It was found that the use of microfluidic synthesis methods can circumvent major drawbacks of classical flask synthesis. The synthesis of NPs is generally influenced by factors such as reaction time, ligand concentration, and ligand ratios. The influence of these factors on the morphology, dispersity, size and catalytic activity of the particles was demonstrated in the examples studied.

The first research project focuses on the synthesis of perfectly shaped CoO nanooctahedra. To achieve this morphology for electrocatalytic applications, different series of reactions were performed by (i) varying the ligand concentrations of OAC/OAM at constant ratio, (ii) varying the reaction time at different ligand ratios, (iii) keeping the total amount of ligands constant (24 mmol) but changing their ratio, and (iv) the concentration effect of each ligand. In general, when an excess amount of OAC was used, no conversion occurred, a viscous violet product was obtained, indicating the formation of cobalt oleate, while an excess amount of OAM led to the formation of elemental Co as a by-product. The octahedral CoO NPs were obtained at an equal concentration of OAC and OAM and a reaction time of 60 min. XRPD measurements could demonstrate the phase purity of CoO, while IR measurements showed only OAC as surfactant. SQUID measurements could determine the corresponding Néel temperature of CoO. XPS measurements showed no evidence of the frequent oxidation of the CoO surface to Co_3O_4. In agreement with the experimental results, simulations were also performed with respect to the binding energies of the ligands on the surface. Again, a ratio of 1:1 was determined to be the optimum ratio at which the binding energy for the binding of OAC to the surface of the NPs is the lowest. Finally, two different samples were tested for their electrochemical performance with respect to OER. This showed that the perfectly shaped CoO nanooctahedra exhibited the highest activity in alkaline medium, highlighting the influence of morphology on the activity, with a small initial OER potential (1.61 V vs. RHE), a large anodic current, and a long shelf life. Based on their morphology, they were superior to spherical or multioctahedral CoO NPs. Thus, we were able to demonstrate the influence of morphology on catalytic activity and thus the need for optimization.

In the second project of the thesis, CeO_2 NPs were prepared in a flask synthesis. This synthesis was then transferred to a microfluidic setup with segmented flow in large volume. The

segmented flow consisted of the reaction solution and water as immiscible phase. The yield was increased by a factor of 20 with the microfluidic approach. HRTEM, XRPD, FTIR and TGA measurements revealed no significant differences between products from both synthesis methods in terms of morphology, particle size and surface occupancy. The surface of the NPs was mainly occupied by OAM and carbonate. Since the surface occupancy also blocks the catalytic centers of the NPs, the samples from the segmented flow were annealed at different temperatures to remove the surfactants. No organic residues could be detected as early as 185 °C, but the surface was still covered with carbonate ligands, which decomposed at higher temperatures. Based on BET and HRTEM measurements, the diameter of the particles was found to increase with increasing heating temperature, resulting in a smaller surface area to volume ratio. The zeta potential measurements also showed a continuous decrease in potential with increasing heating temperature. Therefore, the total catalytic activity should decrease with increasing heating temperature. However, from the kinetic studies, the bromination rate increased sharply at 500 °C for the catalytic oxidative halogenation compared to the sample annealed at 185 °C, while it decreased again significantly for the particles at 800 °C heating temperature. This clearly shows the significant influence of the carbonate on the activity of the particles, regardless of the surface-to-volume ratio. However, for embedding in polycarbonate, high dispersibility was required to ensure uniform distribution of the NPs on the surface of the polycarbonate and to obtain a smooth and transparent surface. Therefore, both the particles annealed at 185 °C and those directly derived from synthesis were used for the biofilm tests. Based on EDX measurements, CeO_2 was detected on the surface of the polycarbonate. In addition, the composites showed the bromination of phenol red in the phenol red test. The composites were then evaluated for their inhibition of biofilm growth of *P. aeruginosa* (PA14). Inhibition of biofilm formation was demonstrated by crystal violet staining and epifluorescence surface microscopy. As expected, the composites with the particles annealed at 185 °C showed higher activity than those with the unannealed NPs. The biofilm inhibition was about 85% of the reference. In addition, a significant decrease in the formation of the virulence factor pyocyanin, which is involved in the quorum sensing system of bacteria, was observed (55%). This suggests that CeO_2 NPs affect quorum sensing and therefore inhibit biofilm formation in a non-biocidal manner.

In the third project, a new rapid and automated microfluidic synthesis for $NaCrO_2$ and related compounds was elaborated based on the emulsion drying technique. The reaction time decreased by almost an order of magnitude compared to the standard batch process. The product obtained from the microfluidic system contained the precursor, which had to be

annealed at 800 °C to obtain the final product. XRPD measurements showed no differences between the product from the batch and microfluidic synthesis. HRTEM and SEM images showed a crystalline, plate-like morphology with well-defined structures corresponding to $NaCrO_2$. XPS and EDX spectra showed the presence of Na, Cr, and O species, with no presence of Cr^{4+} observed, suggesting a phase-pure composition of the particles. To gain insight into the formation of the particles, the precursor and final product were examined. Raman, ^{1}H and ^{23}Na NMR, TG/DTG/DSC and FTIR measurements were performed. The Raman spectra showed the presence of $NaNO_3$ before annealing and Cr-O vibrations after annealing matching $NaCrO_2$. It can be concluded that $NaNO_3$ remains unchanged during the microfluidic synthesis of the precursor but decomposes during the annealing of the precursor. The ^{23}Na NMR spectra showed a single resonance that perfectly matches $NaNO_3$ for the pre-annealed product and disappears after annealing. After annealing, three broad ^{23}Na resonances appear, indicating three new sodium environments. To determine the central band and the side band, measurements were made at different spinning frequencies. The small field shift at -270 ppm is due to hyperfine interaction with Cr^{3+}. The other two ^{23}Na resonances are in the spectral range for sodium species in a diamagnetic compound, which is due to the interaction of sodium with diamagnetic Cr^{6+} in $Na_2Cr_2O_7$ Even though no other phases were detected in the XPRD measurements, the $Na_2Cr_2O_7$ phase could be highly disordered and present in very small amounts. ^{1}H-NMR revealed proton resonances for the annealed product originating from the Tween surfactants that formed the micelles. The signals disappear after annealing at 800 °C. The TG/DTG/DSC measurements for the pre-annealed product showed a mass loss corresponding to the evaporation of water and kerosene in the first two stages. The third stages showed another significant mass loss and an exothermic reaction at 307 °C, which can be attributed to the oxidation of the surfactant. The very broad fourth and fifth stages indicated pyrolysis of several compounds and $NaNO_3$. Therefore, we assume that the surfactants act as nanoreactors encapsulating the reactants during emulsion drying. Upon removal of the water and kerosene in the spiral condenser, the micelles precipitate while the reactants are still encapsulated and mixed at the atomic level and in an appropriate ratio. The micelles collapse during the drying process and decompose when heated. $NaNO_3$ melts and decomposes inside to form charred "nanoreactors" that form nanoscale $NaCrO_2$. The same synthesis could then be performed with other metallic reactants, which are also potential SIBs. XRPD measurements showed that rapid synthesis of $NaFeO_2$, $NaCoO_2$, and $NaAlO_2$ was also successful.

In this work, an insight into the interaction of nanoparticles and auxiliary surfactants in the synthesis of nanoparticles has been provided. Numerous syntheses are based on the interaction

of the multiple ligands. A better understanding of their interaction will, in principle, allow a more targeted use of surfactants to prepare particles of other compositions. Studies of NPs with other compositions using auxiliary surfactants could support our hypothesis. Batch syntheses can be transferred to microfluidics. This eliminates some of the drawbacks of classical synthesis. This allows the synthesis of NPs where the yield and quality of the products are very low or single-homogeneous. For CeO_2-NPs, dopants could be used in microfluidic synthesis to increase the inhibition of biofilm formation. Suitable dopants would include bismuth or lithium. The use of water as a transport medium in the segmented flow could prevent clogging of the pipelines. Since water is particularly favorable as a transport medium and does not form an emulsion without external influence, as well as changing into the gas phase at higher temperatures and thus having no significant influence, this type of synthesis is particularly suitable for the synthesis of NPs in nonpolar media. Thus, a suitable method is offered that eliminates both the disadvantages of classical synthesis and the disadvantages of microfluidic synthesis. The developed method can be used for a range of NPs with different compositions. The synthesis of layered oxides such as $NaCrO_2$, $NaFeO_2$, and $NaCoO_2$ by microfluidic synthesis enables automated and easy fabrication of electrode materials. It also opens up the possibility of producing a wide range of metal layered oxides, including, for example, the lithium electrode materials already in use, providing an alternative to conventional methods. Potentially, more compounds could be prepared using this method, and the materials already prepared could be doped and generally tested for electrochemical performance. Summa summarum, this work is intended to provide an improvement in certain syntheses in terms of their reaction time and yield, but also to provide insight into the formation of particles using specific ligands.

7. Appendix

7.1 Authorship Contributions

Manuscript Title:

Selective Synthesis of Monodisperse CoO Nanooctahedra as Catalysts for Electro-chemical Water Oxidation (Langmuir, 2020, 36, 13804-13816, reproduced with the permission of the American Chemical Society)

All persons who have contributed sufficiently to meet the authorship criteria concerning the design, analysis, writing of revisions of the manuscript are listed.

Authorship Contributions

Please note the contribution of each other author is listed starting with the initials followed by their surname. The * marks the first author(s).

Category 1:

Conception and design of study: ███████████████████

Acquisition of data: ██ █████ (synthesis, transmission electron microscopy, infrared spectroscopy, SQUID measurements), ████████ (synthesis assistance), ██████ (catalytic measurements), ██████████ (simulation experiments), ███████████ (high resolution transmission electron microscopy), █████████ (catalytic measurements), ██████ (BET measurements), ██████████ (X-ray powder diffraction and Rietveld refinement)

Analysis and/or interpretation of data: ████████████████████████████ ██████████████████

Category 2:

Drafting the manuscript: ██████████████

Revising the manuscript crticially for important intellectual content: ████████████ ████████████████

Category 3:

Approval of the manuscript to be published (name of all authors are listed): ██████████

██

███████████████

Manuscript Title:

A Simple Microfluidic Benchtop System for High-Throughput Synthesis of CeO2 Nanoparticles in Segmented Flow for Highly Transparent Nanocomposites Repelling Pseudomonas aeruginosa PA14 Biofilms (revised and resubmitted to Advanced Materials Interfaces)

All persons who have contributed sufficiently to meet the authorship criteria concerning the design, analysis, writing of revisions of the manuscript are listed.

Authorship Contributions

Please note the contribution of each other author is listed starting with the initials followed by their surname. The * marks the first author(s).

Category 1:

Conception and design of study: ██████████████████

Acquisition of data: ██ ████████ (synthesis, transmission electron microscopy, infrared spectroscopy, thermogravimetric analysis), ██████████ (surface coating, energy-dispersive X-ray spectroscopy, catalytic measurements, contact angle measurements), ██████████ (biofilm assays, crystal violet staining, Epifluorescence and fluorescence microscopy), ██████████ (catalytic measurements) ██████████ (high resolution transmission electron microscopy), ██

██ (BET measurements), ██████████ (X-ray powder diffraction and Rietveld refinement), ████████ (nanoindentation)

Analysis and/or interpretation of data: ████████████████████████████████ ████████████████

Category 2:
Drafting the manuscript: ████████████████████████

Revising the manuscript crticially for important intellectual content: ██████████████ ██████████████████████████████████████

Category 3:
Approval of the manuscript to be published (name of all authors are listed): ████████████████ ██ ████████████████████████████

Manuscript Title

Generalized Synthesis of NaCrO$_2$ Particles for High-rate Sodium Ion Batteries Prepared by Microfluidic Synthesis in Segmented Flow (to be submitted to Dalton Transactions)

All persons who have contributed sufficiently to meet the authorship criteria concerning the design, analysis, writing of revisions of the manuscript are listed.

Authorship Contributions

Please note the contribution of each other author is listed starting with the initials followed by their surname. The * marks the first author(s).

Category 1:

Conception and design of study: ███████████████████

Acquisition of data: ████████ (synthesis, infrared spectroscopy), ████████████ (synthesis assistance, laser scanning microscopy), ████████ (Pawley refinement), ████████ (high resolution transmission electron microscopy), ████████ (X-ray photoelectron spectroscopy), ██ ████ (scanning electron microscopy), ████████████ (Raman spectroscopy), ████████████ (nuclear magnetic resonance spectroscopy)

Analysis and/or interpretation of data: ████████████████████████████████ ██████

████████ *2:*

Drafting the manuscript: ████████████████

Revising the manuscript crticially for important intellectual content: ████████████ ██████████████████████

Category 3:

Approval of the manuscript to be published (name of all authors are listed): ████████ ████████████████████████████████████ ██████

Acknowledgments:

We thank ████████████ for X-ray diffraction measurements, ████████ for the XPS measurements and ████████████ for the TGA/DSC measurements. The microscopy equipment is operated by the electron microscopy center, Mainz, (EMZM) supported by the Johannes Gutenberg-University. We thank ████████████ for access to the powder diffractometer, ████████████ for access to the XPS spectrometer, ████████████ for access to the IR spectrometer and ████████████ for access to the TGA/DSC.

7.2 List of Figures

7.3 List of Tables

7.4 List of Abbreviations

AI	Autoinducer
ATR-IR	Attenuated total reflection infrared spectroscopy
BET	Brunauer-Emmett-Teller
BFGS	Broyden-Fletcher-Goldfarb-Shanno
DSC	Differential scanning calorimetry
DTG	Derivative Thermogravimetry
EIS	Electrochemical impedance spectroscopy
FEP	Fluorinated ethylene propylene
FFT	Fast Fourier transform
(FT)IR	(Fourier-transform) infrared spectroscopy
FTO	Fluorine-doped tin oxide
GCE	Glassy carbon electrode
HPO	Haloperoxidase
(HR)TEM	(High-resolution) transmission electron microscopy
LB	Lysogeny broth
LIB	Lithium-ion battery
LSV	Linear sweep voltammogram
M	Metal
NCA	Lithium nickel cobalt aluminium oxides
NMC	Lithium nickel manganese cobalt oxides
NMR	Nuclear magnetic resonance
NP	Nanoparticle
OAC	Oleic acid
OAM	Oleylamine
ODE	1-Octadecene
OER	Oxygen evolution reaction
OPT	Optimized synthesis
PA	Pseudomonas aeruginosa
PDI	Polydispersity index
PEEK	Polyether ether ketone
PR	Phenol red

PTFE	Polytetrafluorethylene
RHE	Reversible hydrogen electrode
ROR	Rate of reaction
SAED	Selected area electron diffraction
SIB	Sodium-ion battery
SQUID	Superconducting quantum interference device
TBPB	Tetrabromphenol blue
TGA	Thermogravimetric analysis
TOF	Turnover frequency
XPS	X-ray photoelectron spectroscopy
XR(P)D	X-ray (powder) diffraction

7.5 Curriculum Vitae

Massih Ahmad Sarif

PERSÖNLICHE DATEN:

Geburtsdatum: ██████████

Geburtsort: ██████████████

Staatsangehörigkeit: ███████

Adresse: ████████████
████████████

Sprachen: ████████████████████████████
██████████████████████████████
████████████████████

Ausbildung:

08/2018-aktuell   Promotionsstudium im Fachbereich Chemie
Johannes Gutenberg-Universität Mainz

08/2015-08/2018   Chemiestudium
Johannes Gutenberg-Universität Mainz
Abschluss: Master of Science

04/2012-08/2015   Chemiestudium
Johannes Gutenberg-Universität Mainz
Abschluss: Bachelor of Science

08/2008-06/2011   Allgemeine Hochschulreife
Georg-Christoph-Lichtenberg-Oberstufengymnasium
Bruchköbel

Akademische Tätigkeiten:

06/2020-07/2020   Praktikumsbetreuung „Chemie für Biologen",
           Johannes Gutenberg-Universität Mainz

02/2020-03/2020   Praktikumsbetreuung „Chemie für Mediziner und
           Zahnmediziner"
           Johannes Gutenberg-Universität Mainz

10/2019-11/2019   Praktikumsbetreuung des präparativen anorganischen
           Praktikums „AC2"
           Johannes Gutenberg-Universität Mainz

10/2018-02/2019   Betreuung der Bachelorarbeit von ████████, Johannes
           Gutenberg-Universität Mainz

08/2015-02/2016   SNU Seoul National University, Republik Korea
           Department Chemie
           DAAD-Auslandssemester

Interessen:

Kraftsport, Fußball, Sprachen, Lesen

Mainz, 16.09.2021
Ort, Datum

147